Pompage de spin et absorption de spin dans des hétérostructures magnétiques

Abhijit Ghosh

UNIVERSITÉ DE GRENOBLE

THÈSE

Pour obtenir le grade de

DOCTEUR DE L'UNIVERSITÉ DE GRENOBLE

Spécialité : **Physique**

Arrêté ministériel : 7 août 2006

Présentée par

Abhijit GHOSH

Thèse dirigée par **Ursula EBELS** et
codirigée par **William E. BAILEY**

préparée au sein du **Laboratoire SPINTEC UMR 8191**
dans **l'École Doctorale: Physique**

Spin pumping and spin absorption in magnetic heterostructures

Thèse soutenue publiquement le **12 Novembre 2012,**
devant le jury composé de :

Prof. Dirk GRUNDLER
Technische Universitaet Muenchen, Germany, Rapporteur
Prof. Sergio O. VALENZUELA
ICREA Professor, Institut Catala de Nanotecnologia, Spain, Rapporteur
Dr. Laurent VILA
Ingenieur Chercheur CEA, Grenoble, Membre
Dr. Jan VOGEL
Institut Néel Grenoble, Examinateur
Dr. Ursula EBELS
Ingenieur Chercheur CEA, Grenoble, Directrice de Thèse
Prof. William E. Bailey
Columbia University, New York, Co-directeur de Thèse

Université Joseph Fourier / Université Pierre Mendès France /
Université Stendhal / Université de Savoie / Grenoble INP

Acknowledgment

I would like to thank all of those who in one way or another have contributed to the completion of my thesis. Without their assistance this thesis would not have been possible.

First and foremost, I would like to express my deepest sense of gratitude to my supervisors Dr. Ursula Ebels and Dr. William E. Bailey, for their continuous support, advice, encouragement throughout the course of my PhD study and research. I am really thankful to them for their careful supervision and the effort that they put into training me. I really appreciate the share of knowledge and ideas that we had throughout last three years. Their generosity and candidness created a very pleasant and productive environment. It has been a privilege working with them.

I consider myself really fortunate to be a part of Spintec laboratory. I find, in this type of specialized laboratory where more than 50 people are working in the domain of magnetism and spintronics, knowledge share becomes much easier. I have deepest regard for Stephane Auffret, who has deposited very high quality samples for my studies, taking a minimum time. I would like to thank Eric Gautier for the transmission electron microscopy (TEM) measurements. I am thankful to F. Wilhelm, and A. Rogalev of the European Synchrotron Radiation Facility (ESRF), who have performed the XMCD measurement and analysis, which was an important step for understanding our FMR results. In many occasions, when I was struggling with the theoretical understandings, the inputs from Mairbek Chshiev, Bernard Dieny and Oliver Klein proved to be really crucial. I would like to thank Mihai Miron for helpful discussion especially at the end of the thesis, Vincent Baltz and Bernard Rodmacq for heaving useful discussions with me.

For a person who does not understand the French language, the administrative processes become much harder, and I am thankful to Catherine and Rachel for helping me out in many occasions in the last three years. The technical support that I have received from Isabelle Joumard and Eric Billiet was very useful. I am grateful to my colleagues in Spintec: Michael Quinsat, Juan Sierra, Elmer Monteblanco, Adrien Vaysset, Pablo Merodio, for useful discussions on and off the physics topic. I am grateful to all my colleagues and office mates in Spintec who have made my stay here an unforgettable moment. I would also like to acknowledge the support that I have had from my friends in Grenoble, who have made my staying away from home much easier. I am thankful to the CEA for providing my financial support of my PhD study.

Last but not the least; I would like to thank my parents, Bijoya, friends back home, and all my teachers, who have supported me in many ways throughout my life.

Résumé

L'interaction entre électrons de conduction itinérants et électrons localisés dans les hétérostructures magnétiques est à l'origine d'effets tels que le transfert de moment de spin, le pompage de spin ou l'effet Hall de spin. Cette thèse est centrée sur le phénomène de pompage de spin : une couche ferromagnétique (FM) en précession injecte un courant de spin pur dans les couches adjacentes. Ce courant de spin peut être partiellement ou totalement absorbé par une couche, dite réservoir de spin, placée directement en contact avec le matériau ferromagnétique ou séparée par une couche d'espacement. L'absorption de la composante transverse du courant de spin induit une augmentation de l'amortissement de la précession ferromagnétique de la couche libre. Cet effet à été mesuré par des expériences de résonance ferromagnétique avec, pour la couche en précession FM, trois matériaux ferromagnétiques différents ($NiFe$, $CoFeB$ and Co), et pour la couche de réservoir de spin, différents matériaux paramagnétiques (Pt, Pd, Ru), ferromagnétiques et antiferromagnétiques. Dans un premier temps, nous avons vérifié que le facteur d'amortissement non-local généré est de type amortissement de Gilbert, et qu'il est inversement proportionnel à l'épaisseur de la couche en précession FM. L'analyse de l'augmentation de l'amortissement a été réalisée dans le cadre du modèle de pompage de spin adiabatique proposé par Tserkovnyak et al. Dans un second temps et suivant ce modèle, nous avons extrait les paramètres de conductance avec mélange de spin à l'interface $g^{\uparrow\downarrow}$ pour différentes interfaces, ces paramètres déterminent le transport du courant de spin à travers des interfaces ferromagnétique/métal non-magnétique. Un troisième résultat important de cette thèse porte sur la longueur d'absorption du courant de spin dans des matériaux ferromagnétiques et paramagnétiques. Celle-ci varie considérablement d'un matériau à l'autre. Pour les matériaux ferromagnétiques, la longueur d'absorption du courant de spin est linéaire par rapport à l'épaisseur de la couche réservoir de spin, avec pour longueur caractéristique $\sim 1.2\,nm$. Ce résultat est en cohérence avec les théories antérieures et avec les valeurs de longueur de déphasage de spin pour le transfert de moment de spin dans les matériaux ferromagnétiques. Dans les paramagnétiques tels que Pt, Pd, Ru, la longueur d'absorption est soit linéaire soit exponentielle selon que le réservoir paramagnétique est directement en contact avec la couche en précession ou bien séparé par une couche mince d'espacement en Cu. La longueur caractéristique correspondante est inférieure à la longueur de diffusion de spin. Des mesures complémentaires de dichroïsme circulaire magnétique par rayons X ont révélé une induction de moments magnétiques dans les matériaux paramagnétiques comme Pd, Pt, lorsque couplé directe-

ment ou indirectement avec une couche FM. Ce résultat fournit une explication de la dépendance en épaisseur linéaire observée dans les hétérostructures en contact direct. Etant donné que le pompage de spin et le couple de transfert de spin (STT) sont des processus réciproques, les résultats de cette thèse sur la conductance avec mélange de spin, la longueur d'absorption de spin et les moments de spin induits sont également d'un grand intérêt pour les études de transfert de moment de spin, ainsi que d'effet Hall de spin, direct et inverse. L'avantage des études présentées ici réside dans le fait qu'elles sont effectuées sur des couches minces continues, sans aucune étape de nanofabrication.

Abstract

In magnetic heterostructures, the interaction between itinerant conduction electrons with localized electrons is at the origin of effects such as the spin momentum transfer, spin pumping or the spin Hall effect. This thesis is centered on the phenomenon of spin pumping, which states that a precessing ferromagnetic (FM) layer injects a pure spin current into its adjacent metallic layers. This spin current can be partially or fully absorbed by a spin sink layer, placed directly in contact with the ferromagnet or separated by a spacer layer. The absorption of the transverse component of the spin current results in an enhancement of the effective damping of the precessing ferromagnet which we have studied using ferromagnetic resonance experiments for three different ferromagnets ($NiFe$, $CoFeB$ and Co) as the precessing FM layer and various paramagnets (Pt, Pd, Ru), ferromagnets or an antiferromagnet as the spin sink layer. As a first step we have verified that the additional non-local damping is Gilbert type, and that it depends inversely on the thickness of the FM precessing layer. The analysis of the enhanced damping was done in the frame of an adiabatic spin pumping model proposed by Tserkovnyak et al. Within this model we extracted as a second step the interfacial spin mixing conductance parameters $g^{\uparrow\downarrow}$ for various interfaces, which determine the spin current transport through FM/NM interfaces. A third important result of the thesis concerns the absorption length of spin currents in ferromagnets and paramagnets which we found can be very different. In ferromagnets the spin current absorption is linear with the spin sink layer thickness, with a characteristic length of $\sim 1.2\,nm$. This is consistent with theory and the spin dephasing length for spin momentum transfer in ferromagnets. In paramagnets such as Pt, Pd, Ru, the spin current absorption is either linear or exponential depending on whether the paramagnetic is directly in contact with the FM or separated by a thin Cu spacer layer. The corresponding characteristic length is less than the spin diffusion length. Complementary X-ray magnetic circular dichroism measurements revealed induced magnetic moments in paramagnets like Pd, Pt when directly or indirectly coupled with a FM layer. This provides an explanation for the linear thickness dependence for the direct contact heterostructures. Since spin pumping and spin transfer torque (STT) are reciprocal processes the results of this thesis on the spin mixing conductances, spin absorption length scales and induced moments will also be of great interest for studies on spin momentum transfer, Spin Hall effect and Inverse Spin Hall effect. The convenience being that these studies can be done on continuous films and no nanofabrication is required.

Contents

Introduction

Magnetism and magnetic phenomena in nanostructures is a very active research area in condensed matter physics and nanoscience. Considerable improvements in thin film deposition technology and nanofabrication techniques in the late 1980's gave a huge boost to the research in magnetism, resulting in the discovery of various fundamental phenomenons such as oscillatory interlayer exchange coupling of ferromagnetic/nonmagnetic multilayer, Giant magnetoresistance, Tunneling magnetoresistance (TMR), Spin transfer torque (STT) effects, etc. These fundamental phenomena also offer huge potential for applications. This gave rise to the sub field of spintronics, where the idea is to control and manipulate electron's spins.

Nowadays, magnetic materials and spintronics concepts are well established in the data storage technology. Other emerging application possibilities are magnetic logic components, magnetic random access memory (MRAM), or microwave oscillators. It is evident that, in order to improve the applications, an understanding of the fundamental concepts is very important. Almost all of these applications are based on a spin polarized current flow through the circuit. Therefore, it is very important to understand the spin polarized current transport in these systems. In the 1990's an important focus of the studies was GMR, TMR, where current flow through these devices was controlled by the magnetization direction. In the late 90's a new phenomena was proposed and later on confirmed which shows that the magnetization direction can be controlled by a spin polarized current flowing through them. This has enabled current controlled magnetization switching or current controlled steady state oscillation. The fact that the magnetization state can be controlled by an electrical current, instead of an applied field has opened new possibilities for device applications, or device architecture.

A reciprocal phenomenon of STT, where the precession of magnetization drives a pure spin current into its adjacent metals was proposed in the last decade. This effect was first studied in $FM1/NM/FM2$ type structures, where a broadening of the FMR linewidth of the precessing thin ferromagnetic layer $FM1$, caused by $FM2$ was observed.

Experiments were carried out by the groups of Heinrich et al. (2003) and Mizukami et al. (2001) to verify this broadening of linewidth. A proper theoretical development for this phenomenon was made by Tserkovnyak et al, based on a scattering theory approach, using magnetoelectric circuit theory. Since the consequences of spin pumping leads to an enhancement of the relaxation rate of the magnetization, this effect can be studied by means of ferromagnetic resonance (FMR) linewidth measurements. This thesis work is primarily based on the experimental study of spin pumping in magnetic heterostructures using FMR.

Since spin pumping and spin transfer torque are reciprocal phenomena, the transport related parameters are the same. They can be extracted easily from spin pumping, which will be of use for STT. This will provide a much better understanding of these two phenomena from a fundamental point of view. The magnetization damping is a very important parameter to characterize, because STT induced switching or precession is directly related to the relaxation of magnetization. In both cases, the threshold current, which is called critical current, depends on the value of the damping parameter. Spin pumping reveals that damping in a ferromagnetic layer can be caused by nonlocal contributions, i.e. layers not directly attached to the FM layers but present in a magnetic heterostructure. This is hence important for GMR and TMR based devices and a precise determination of damping is even more important for the implementation of these novel effects in magnetoelectronics.

In the first chapter of the thesis we will go through the basics for studying magnetization dynamics and discuss the mechanism involved in magnetization relaxation. In the second chapter, we will introduce the phenomenon of spin transfer torque and spin pumping and present the most important parameters that describe the transport of a pure spin current or spin polarized charge current in magnetic heterostructures. In the end of this chapter an overview of prior work on spin pumping will be presented to put this thesis work into context. In the third chapter, we will discuss our experimental techniques, and how we optimize our setup for a better characterization of the samples. We will discuss about our most important characterization technique which is ferromagnetic resonance and we will also discuss the basics of X-ray magnetic circular dichroism, which will be used in chapter 6. In the fourth chapter, we will demonstrate the verification of the spin pumping phenomenon in a broad range of ferromagnetic materials using various spin sink layer metals. We will demonstrate that spin pumping is a general phenomenon and that it is not restricted to certain materials. In the fifth chapter, we will use spin pumping as a method to generate a pure spin current, which is then injected into various nonmagnetic, ferromagnetic materials to study spin current decay/ absorption by differ-

ent spin sink materials. In chapter 6, we will present our XMCD study, which provides an explanation of some of our results in chapter 5, from a different point of view. The thesis ends with a summary of our main results and presenting open questions.

Chapter 1

Basics of Magnetization Dynamics

In this chapter we go through the basics which are very important not only for studying magnetization dynamics but for studying magnetism in general. In the first section we recall the angular momentum associated with the electron's spin and its orbital motion and their coupling. Then we present different energy contributions associated with thin magnetic film structures such as exchange energy, crystalline anisotropy energy, demagnetization energy etc. Assuming the equilibrium condition we look at the minima of the total energy and solve the Landau-Lifshitz-Gilbert equation (LLG), describing the magnetization dynamics. We look at the solution of the LLG equation for given boundary conditions considering small perturbations (small angle precession) and concentrate on its linear solutions. We look at the dynamic susceptibility and the resonance condition for magnetization. At the end of this chapter we will go through the processes that are involved in the relaxation of the magnetization and phenomena related to it.

1.1 Magnetic Moments

Ferromagnetism arises because of the exchange interaction between the neighboring spins. To understand this phenomenon we recall the magnetic moments associated with the electrons spin and its orbital motion. Electrons moving in an atomic orbit has orbital magnetic moment $\boldsymbol{\mu_L}$ and spin magnetic moment $\boldsymbol{\mu_S}$; defined as: $\boldsymbol{\mu_L} = \gamma_L \mathbf{L}$ and $\boldsymbol{\mu_S} = \gamma_L \mathbf{S}$, where $\mathbf{L}$ is the total orbital angular momentum and $\mathbf{S}$ is the total spin angular momentum with γ_L and γ_S being their respective gyromagnetic ratios. These gyromagnetic ratios are defined in terms of Plank's constant (h), Bohr magnetron (μ_B), and the gyromagnetic splitting factor $g_L$and g_S as; $\gamma_{L,S} = g_{L,S}\frac{\mu_B}{h}, \mu_B = \frac{|e|h}{2m}$.

The total angular momentum is seen as: $\mathbf{J} = \mathbf{L} + \mathbf{S}$ and the corresponding total

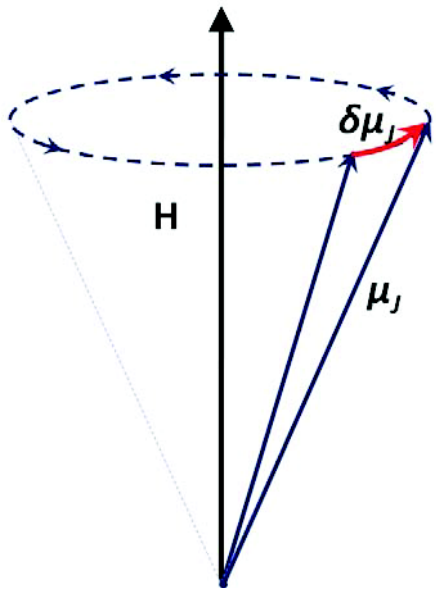

Figure 1.1: Precession of magnetic moment $\boldsymbol{\mu}_j$ around the applied field H.

magnetic moment $\boldsymbol{\mu}_\mathbf{J} = \gamma_J \mathbf{J}$. γ_J is known as the gyromagnetic ratio. If this total magnetic moment is subjected to an external (time varying) magnetic field $\mathbf{H}$, a torque will act on the total magnetic moment, seen as: $\boldsymbol{\mu}_\boldsymbol{J} \times \mathbf{H}$. The equation of motion of the magnetic moment is found by equating the applied torque to the rate of change of angular momentum.

$$\frac{d\boldsymbol{\mu}_\mathbf{J}}{dt} = -\gamma_J \left(\boldsymbol{\mu}_\boldsymbol{J} \times \mu_0 \mathbf{H}\right) \tag{1.1}$$

μ_0, is the free space permeability ($\mu_0 = 4\pi 10^{-7}$ H/m). This equation of motion describes a precessional motion of the total magnetic moment around the external applied field with a characteristic frequency f, known as Lamour frequency, defined as $f = \frac{1}{2\pi} \cdot \frac{e\mu_0 \mathbf{H}}{m_e} = C * H$, where C is a constant.

This total magnetization $M = M_S \mathbf{m}$ is better known as *spontaneous* magnetization for the magnetic system and the modulus of $|M|$ is conserved so that it has two degrees of freedom instead of three. The equation of motion for this magnetization can be defined in a similar manner as in the case of a single magnetic moment. This describes the fundamentals of magnetization precession around an effective field [1] (see Figure 1.1), which is also the basics of Brown's equations [2] and the Landau-Lifshitz-Gilbert equation[3, 4]:

$$\frac{d\mathbf{M}}{dt} = -\gamma \left(\mathbf{M} \times \mu_0 \mathbf{H}_{eff}\right) \tag{1.2}$$

Note that, we have used an effective field $\mathbf{H}_{eff}$, instead of just a bias field $\mathbf{H}$. This is because, in a thin magnetic field there are several energies which gives rise to a total effective field. Therefore, $\mathbf{H}_{eff}$ in the expression above is a combination of all these fields, which are present in the magnetic system plus the applied bias field. The effective field is related to the total energy in the magnetic system by the relation:

$$\mathbf{H}_{eff} = -\frac{1}{\mu_0 M_S}\frac{\delta e_{tot}}{\delta \mathbf{m}}. \tag{1.3}$$

In the following section, we derive all the energy terms which are important for the configuration of our interest, and determine the effective field for our system.

1.2 Different energy contribution in thin films

The total energy of a ferromagnetic system in an applied field is given by the sum of the exchange energy e_{ex}, Zeeman energy e_{zee}, anisotropy energies e_{ani} and demagnetization e_{dem} as:

$$e_{tot} = e_{ex} + e_{zee} + e_{ani} + e_{dem}.$$

This means that even in the absence of an external applied field (or the zeeman energy) there is an effective field present and acting on the magnetization. With the application of an external field, depending on the internal and external forces, different equilibrium conditions for the magnetization can be obtained. According to micromagnetic theory the magnetic equilibrium is a consequence of reaching the minimum energy state.

Exchange energy

The exchange interaction is a short range interaction between neighboring spins which gives rise to the parallel alignment of the magnetic moments. The exchange interaction is the strongest coupling occurring between two neighboring spins. The exchange energy for a system of N atoms with spins $\mathbf{S_i}, \mathbf{S_j}, ..., \mathbf{S_N}$ is seen as:

$$e_{ex} = -\sum_{i,j}^{N} J_{ij}(\mathbf{S_i} \cdot \mathbf{S_j}) = -2\sum_{i<j}^{N} J_{ij}(\mathbf{S_i} \cdot \mathbf{S_j})$$

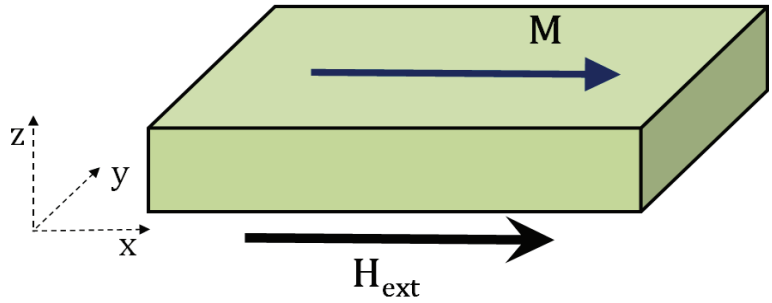

Figure 1.2: In plane magnetization of a ferromagnetic thin film.

where J_{ij} is the exchange integral, whose value depends on the distance between the interacting spins. When J_{ij} is positive, the exchange energy minimum leads to a ferromagnetic order between the spins but when J_{ij} is negative it leads to anti-parallel (antiferromagnetic) ordering. J_{ij} is related to the overlap of the electronic orbitals of adjacent atoms and to the Pauli exclusion principle. This exchange interaction falls rapidly with increasing distance and therefore the summation is limited to the nearest neighbors only. This is due to the overlapping of wave functions (local) of nearest neighbors, resulting in an energy contribution.

Zeeman energy

The interaction between the magnetization vector $\mathbf{M}$ and an external magnetic filed $\mathbf{H}_{ext}$ leads to an energy known as Zeeman energy. Zeeman energy is minimum when the magnetization is along the direction of the external field. The Zeeman energy term is expressed as:

$$e_{zee} = -\mu_0(\mathbf{M} \cdot \mathbf{H}_{ext}).$$

Magnetocrystalline anisotropy energy

The magnetization of a crystalline material will have an energetically preferred direction depending on the crystalline structure and the symmetry. Certain factors like the charge distribution of the ions in the crystal and the electrostatic interaction between the orbitals of the electrons determining the magnetic properties can impose a certain direction to $\mathbf{M}$. The dependence of magnetic energy on the orientation of the magnetization with respect to the crystallographic directions is called magneto-crystalline anisotropy. Certain orientations of the magnetic moments are more favorable energetically than others. This

preferred direction for the magnetization is called easy axis. The magneto-crystalline energy is usually small compared to the exchange energy and it depends on the structure of the crystal. The simplest case is the uni-axial anisotropy in which the energy expression is

$$e^k_{ani} = K^u_{ani}[1 - (\mathbf{m} \cdot \mathbf{u}_k)^2].$$

Here $\mathbf{u}_k$ is the unit vector along the direction of the easy axis and K^u_{ani} is the anisotropy energy constant expressed in the units of J/m^3, and $\mathbf{m}$ is the unit vector along the direction of magnetization i.e. $\mathbf{m} = \mathbf{M}/\mathbf{M_s}$. For simplicity we consider that the magnetization is aligned along the uni axial anisotropy direction.

In case of ultrathin magnetic films several other anisotropy contributions such as surface, interface, and exchange anisotropies can exist. This effect which is negligible in bulk samples is attributed to the reduced symmetry of the atomic environment of surface atoms. In case of surface (interface) anisotropy, this energy is described using a phenomenological uni-axial perpendicular (surface) anisotropy parameter K_{ani} acting along the $\hat{\mathbf{z}}$ direction (see Figure 1.2). The surface anisotropy energy of a ferromagnetic film of thickness t is viewed as:

$$e^s_{ani} = \frac{K^s_{ani}}{t}[1 - (\mathbf{m} \cdot \mathbf{u}_S)^2].$$

The perpendicular anisotropy constant K^s_{ani} is in the units of J/m^2.

Demagnetizing energy

In a uniformly magnetized sample, the magnetic poles appear on it's surface, leading to a demagnetizing field, $\mathbf{H}_{dem}$. The energy contribution due to this demagnetizing field is known as demagnetizing energy.

$$e_{dem} = -\frac{\mu_0}{2}(\mathbf{M} \cdot \mathbf{H}_{dem})$$

The demagnetizing energy contribution is found to be small compared to the exchange energy contribution. This is a long range field and even though it has very little or no influence on the parallel alignment of the neighboring spins, it influences the spatial distribution of the magnetization vector. The calculation of $\mathbf{H}_{dem}$ is quite complicated in general. But assuming an uniformly magnetized ellipsoid, it can be calculated as: $\mathbf{H}_{dem} = -\bar{\bar{N}}\mathbf{M}$, where $\bar{\bar{N}}$ is the demagnetizing tensor. If the co-ordinate axes are oriented

along the principal axes of an ellipsoid then $\bar{\bar{N}}$ is diagonal and can be written as

$$\bar{\bar{N}} = \begin{pmatrix} N_x & 0 & 0 \\ 0 & N_y & 0 \\ 0 & 0 & N_z \end{pmatrix}$$

In case of very thin films, the thickness is much smaller compared to in-plane dimensions. When the magnetization lies uniformly in the plane the magnetic charges are avoided which leads to the lowest energy configuration, with the demagnetization factors as $N_x = N_y = 0$ and $N_z = 1$. With these we find the simplified form of the demagnetizing energy as:

$$e_{dem} = \frac{\mu_0}{2}(\hat{\mathbf{z}} \cdot \mathbf{M})^2.$$

1.3 Energy minimization

As discussed earlier, the equilibrium position of the magnetization corresponds to the energy minima. Therefore assembling all the energy terms derived above; the total energy density for the simplest case of a uni-axial material is obtained as:

$$e_{tot} = -2\sum_{i<j}^{N} J_{ij}(\mathbf{S_i}\cdot\mathbf{S_j}) - \mu_0(\mathbf{M}\cdot\mathbf{H}_{ext}) + K^u_{ani}[1-(\mathbf{m}\cdot\mathbf{u_k})^2] + K^s_{ani}[1-(\mathbf{m}\cdot\mathbf{u_s})^2] - \frac{\mu_0}{2}(\hat{z}\cdot\mathbf{M})^2 \tag{1.4}$$

For the case of a perfectly homogeneous magnetized system the total exchange energy is zero. Therefore we ignore the exchange energy term from the above equation. Also we need to keep in mind that we have considered only the fundamental and basic energy contributions. Supplementary contributions arising from magnetostriction, surface (important contribution for us, and we will measure this term) and shape anisotropies or RKKY coupling might have to be taken into account. We also note that the magnetization when subjected to a small perturbation field will not strictly be aligned along the $\hat{\mathbf{x}}$ direction but will also have small $\hat{\mathbf{y}}$ and $\hat{\mathbf{z}}$ component as: $M = M_s\hat{\mathbf{x}} + m_y\hat{\mathbf{y}} + m_z\hat{\mathbf{z}}$. Following eqn 1.3, the effective field within the magnetic system is obtained by taking the variational derivative of the total energy as:

$$\mathbf{H}_{eff} = -\frac{1}{\mu_0 M_S}\frac{\delta\left(-\mu_0(\mathbf{M}\cdot\mathbf{H}_{ext}) + K^u_{ani}[1-(\mathbf{m}\cdot\mathbf{u_k})^2] + K^s_{ani}[1-(\mathbf{m}\cdot\mathbf{u_s})^2] + \frac{\mu_0}{2}(\hat{z}\cdot\mathbf{M})^2\right)}{\delta\mathbf{m}},$$

or,

$$\mathbf{H}_{eff} = \mathbf{H_{ext}} + \frac{2K^u_{ani}}{\mu_0 M_S}(\mathbf{m}\cdot\mathbf{u}_k)\frac{\delta(\mathbf{m}\cdot\mathbf{u}_k)}{\delta\mathbf{m}} + \frac{2K^u_{ani}}{\mu_0 M_S t}(\mathbf{m}\cdot\mathbf{u}_S)\frac{\delta(\mathbf{m}\cdot\mathbf{u}_S)}{\delta\mathbf{m}} - \frac{(\hat{\mathbf{z}}\cdot\mathbf{M})}{M_S}\frac{\delta\,(\hat{\mathbf{z}}\cdot\mathbf{M})}{\delta\mathbf{m}}$$

or,

$$\mathbf{H}_{eff} = \mathbf{H_{ext}} + \frac{2K^u_{ani}}{\mu_0 M_S} m_x\hat{\mathbf{x}} + \frac{2K^u_{ani}}{\mu_0 M_S t} m_z\hat{\mathbf{z}} - m_z\hat{\mathbf{z}}. \tag{1.5}$$

This is the expression for the effective field acting on the magnetization.

1.4 Dynamics of magnetization

Landau-Lifshitz-Gilbert (LLG) equation

In the last section, we have defined the total energy (at equilibrium) of a thin magnetic film and from that we have derived the effective field. But how does the magnetic system reach equilibrium when an external magnetic field is applied to it? To see this, we carry on from where we left in section 1.1 and start with eqn. 1.2. It was understood that the magnetization's gyroscopic motion around the applied field is governed by the equation of motion 1.2. In this equation the field term $\mathbf{H}$ is replaced by $\mathbf{H}_{eff}$ for a ferromagnetic system. Such systems can be considered as a damped oscillator, meaning the magnetization will not precess around the applied field for ever. Depending on the system the magnetization precession decays and it relaxes along the applied field (effective field). Therefore in the equation of motion of the magnetization, we introduce a phenomenological damping term, and the equation of motion for the magnetization from eqn. 1.2 becomes,

$$\frac{d}{dt}\mathbf{M}(t) = -\gamma\left(\mathbf{M}(t)\times\mathbf{H}_{\mathit{eff}}(t)\right) + \frac{\alpha}{M_s}\left(\mathbf{M}(t)\times\frac{d\mathbf{M}(t)}{dt}\right). \tag{1.6}$$

The first term in this equation corresponds to a uniform precession for the magnetization, which is an ideal case where no damping in the system is present as shown in Figure 1.3(a), and the second term is the phenomenological damping term with damping parameter α. Damping acts perpendicular to the direction of motion ($\frac{\mathbf{M}(t)}{M_s}\times\frac{d\mathbf{M}(t)}{dt}$) as rep-

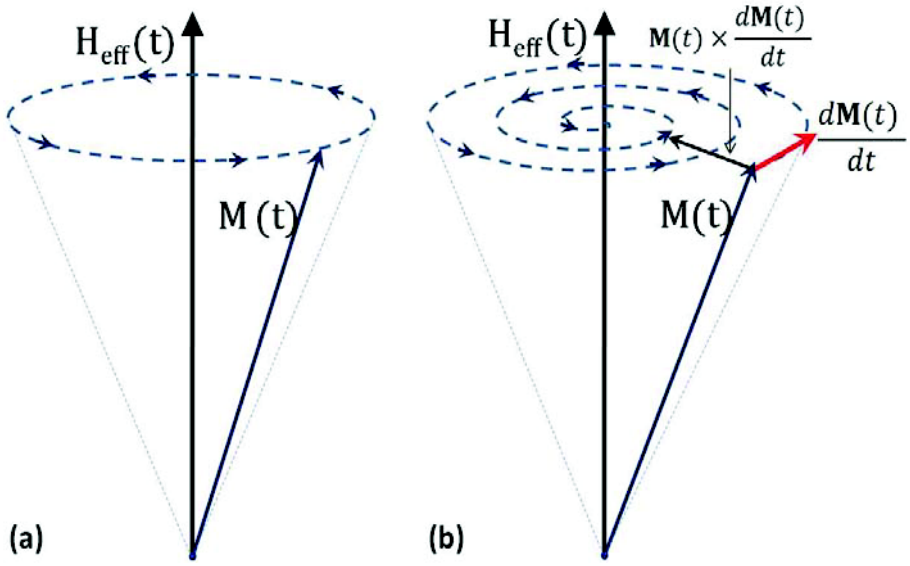

Figure 1.3: (a) Uniform precession of magnetization without any damping in the system. (b) Damping acts $\perp$ to the direction of motion of the magnetization $\mathbf{M}$, and makes it relax along the effective field $\mathbf{H}_{eff}$.

resented in Figure 1.3(b). This equation of motion is known as Landau-Lifshitz-Gilbert (LLG) equation proposed in 1935[3, 4].

Bloch-Bloembergen formalism

Other than Gilbert damping, there is another formalism of introducing the phenomenological damping term. This was introduced by F. Bloch for nuclear magnetic relaxation and later was adapted by N. Bloembergen in ferromagnetic relaxation[5]. With this formalism the equation of motion for the magnetization is given as:

$$\frac{d}{dt}\mathbf{M}(t) = -\gamma\left(\mathbf{M}(t) \times \mathbf{H}(t)\right) - \frac{(\widehat{\mathbf{x}}\cdot\mathbf{M})}{T_2}\widehat{\mathbf{x}} - \frac{(\widehat{\mathbf{y}}\cdot\mathbf{M})}{T_2}\widehat{\mathbf{y}} - \frac{(\widehat{\mathbf{z}}\cdot\mathbf{M})}{T_1}\widehat{\mathbf{z}}, \tag{1.7}$$

where T_1 is the longitudinal relaxation time, describing the relaxation along the equilibrium direction towards the full magnitude of the magnetization ($\mathbf{M_s}$), and T_2 is the transverse relaxation time which describes the relaxation of the magnetization in the equilibrium direction and which reduces the magnitude of $\mathbf{M(t)}$ as shown in Figure 1.4.

However unlike the LLG equation this formalism doesn't take the conservation on magnetic moment into account. The magnitude of the magnetization in this Bloch-

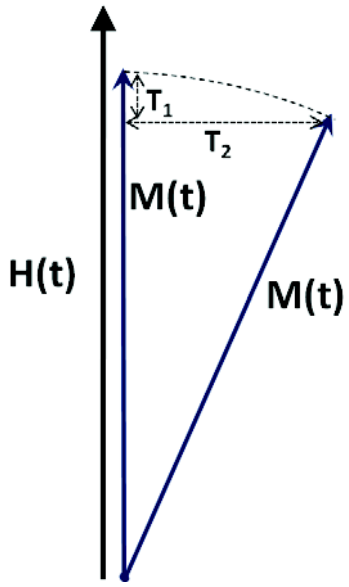

Figure 1.4: Position of magnetic moment at various stages of it's relaxation process in Bloch-Bloembergen formalism.

Bloembergen formalism is conserved only in case of small angle precession and $T_1 = \frac{T_2}{2}$. This description of relaxation will be used to explain the relaxation phenomenon caused by two magnon process.

1.5 Resonance condition and dynamic susceptibility: In-plane field configuration

In the last few sections we have discussed about the gyroscopic precession of the magnetization and its relaxation by introducing a phenomenological damping term in the equation of motion. The time scale for the magnetization relaxation is of the order of nanoseconds, i.e. the magnetization relaxes very fast. One of the ways to study this relaxation is by applying a high frequency pumping field perpendicular to the direction of the external DC field. This high frequency pumping (driving) field pulls the magnetization out of its equilibrium position and tries to make it precess around the effective DC field. However, like any damped oscillator system, this ferromagnetic system also has it's resonance condition determined by the applied DC field H_{ext} acting on it and the frequency ω of the applied microwave field. In this section we will determine this resonance condition and the susceptibility of the magnetic system by solving the differential LLG equation. Finding the solution of LLG in a generalized form is not very easy, therefore

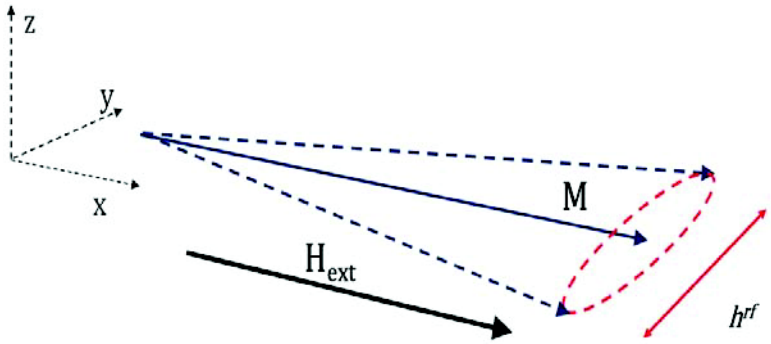

Figure 1.5: Ferromagnetic resonance configuration for magnetic film where the DC field H_{ext} is applied in the film plane an the microwave field h^{rf} is $\perp$ to the DC field.

we will make certain assumptions which are suitable for our system under study. We assume that: (1) H_{ext} is homogeneous where the sample is placed, and the magnetization is aligned along it ($\hat{\mathbf{x}}$). We use the macrospin model of the magnetization in which no spatial variation of $\mathbf{M}$ is taken into account. (2) Our sample is uniformly magnetized and the in plane dimensions are much larger than the thickness. The magnetization lies in plane and the magnetic charges are avoided to reach the lowest energy configuration. Therefore the demagnetization factors become $N_x = N_y = 0$ and $N_z = 1$. (3) A uni-axial perpendicular anisotropy caused by the two surfaces is present. This contribution is very small compared to the demagnetizing field.(4) The high frequency magnetic field h^{rf} is applied along $\hat{\mathbf{y}}$, which is perpendicular to the applied magnetic field H_{ext}.

In order to define the resonance condition we consider that the magnetization makes only a small deviation from its equilibrium. As shown in Figure 1.5, the magnetization when subjected to the rf field h^{rf}, it will have a small y and z component, but it will have small variation along the x direction. Therefore with these assumptions the magnetization is written as: $\mathbf{M} = M_s\hat{\mathbf{x}} + m_y\hat{\mathbf{y}} + m_z\hat{\mathbf{z}}$. The effective field acting on this magnetization is given by eqn. 1.5. We rewrite the effective field after some simplification by defining $H_{uni} = \frac{2K^u_{ani}}{\mu_0 M_S} m_x$, and $M_{eff} = \left(M_s - \frac{2K^S_{ani}}{\mu_0 M_S t}\right)$. After adding the high frequency rf field h^{rf} to the effective field term, the new expression of the effective field is seen as:

$$\mathbf{H}_{eff} = (H_{ext} + H_{uni})\,\hat{\mathbf{x}} + h^{rf}\hat{\mathbf{y}} - \frac{M_{eff}}{M_s} m_z \hat{\mathbf{z}}. \tag{1.8}$$

Using the above form of magnetization and the effective field acting on it, we seek the solution of the LLG equation, which is the equation of motion of a system of two coupled equations for m_y and m_z.

$$\frac{d}{dt}\mathbf{M}(t) = -\gamma_0 (\mathbf{M}(t) \times \mathbf{H}(t)) + \frac{\alpha}{M_s}\mathbf{M}(t) \times \frac{d\mathbf{M}(t)}{dt}$$

$$\begin{pmatrix} \frac{dM_s}{dt} \\ \frac{dm_y}{dt} \\ \frac{dm_z}{dt} \end{pmatrix} = -\gamma \begin{pmatrix} \hat{\mathbf{x}} & \hat{\mathbf{y}} & \hat{\mathbf{z}} \\ M_s & m_y & m_z \\ (\mathrm{H_{ext}}+\mathrm{H_{uni}}) & h^{rf} & -\frac{M_{eff}}{M_s}m_z \end{pmatrix} + \frac{\alpha}{M_s} \begin{pmatrix} \hat{\mathbf{x}} & \hat{\mathbf{y}} & \hat{\mathbf{z}} \\ M_s & m_y & m_z \\ \frac{dM_s}{dt} & \frac{dm_y}{dt} & \frac{dm_z}{dt} \end{pmatrix} \tag{1.9}$$

$$\begin{cases} 0 = -\gamma \left(m_y \frac{M_{eff}}{M_s} m_z - m_z h^{rf} \right) + \frac{\alpha}{M_s} \left(m_y \frac{dm_z}{dt} - m_z \frac{dm_y}{dt} \right) & for\, \hat{\mathbf{x}} \\ \frac{dm_y}{dt} = -\gamma \left\{ m_z (H_{ext} + H_{uni}) + M_{eff} m_z \right\} - \alpha \frac{dm_z}{dt} & for\, \hat{\mathbf{y}} \\ \frac{dm_z}{dt} = -\gamma \left\{ M_s h^{rf} - m_y (H_{ext} + H_{uni}) \right\} + \alpha \frac{dm_y}{dt} & for\, \hat{\mathbf{z}} \end{cases} \tag{1.10}$$

In order to solve these linearized set of equations we assume a harmonic time dependence of $h^{rf} = Re\left(\tilde{h}^{rf} e^{i\omega t}\right)$ and $m_{y,z} = Re\left(\tilde{m}_{y,z} e^{i\omega t}\right)$. The terms which contain the product of h^{rf} and $m_{y,z}$ will be dropped in order to ignore the second order contributions. After linearization, from the second line of 1.10, we obtain:

$$\begin{aligned} i\omega m_y &= -\gamma \left\{ m_z (\mathrm{H_{ext}}+\mathrm{H_{uni}}) + M_{eff} m_z \right\} - \alpha i\omega m_z \\ i\omega m_y &= \left\{ -\gamma (\mathrm{H_{ext}}+\mathrm{H_{uni}} + M_{eff}) - \alpha i\omega \right\} m_z \\ 0 &= i\tfrac{\omega}{\gamma} m_y + \left(A + i\alpha\tfrac{\omega}{\gamma} \right) m_z \end{aligned} \tag{1.11}$$

We choose to set $A = M_{eff} + H_{ext} + H_{uni}$ in order to simplify eqn. 1.11. From the third line of 1.10 we get:

$$\begin{aligned} i\omega m_z &= -\gamma \left\{ M_s h^{rf} - m_y (\mathrm{H_{ext}}+\mathrm{H_{uni}}) \right\} + \alpha i\omega m_y \\ i\tfrac{\omega}{\gamma} m_z &= -M_s h^{rf} + (i\alpha\tfrac{\omega}{\gamma} + \mathrm{H_{ext}}+\mathrm{H_{uni}}) m_y \\ M_s h^{rf} &= -i\tfrac{\omega}{\gamma} m_z + \left(B + i\alpha\tfrac{\omega}{\gamma} \right) m_y \end{aligned} \quad . \tag{1.12}$$

Here again we set $B = H_{ext} + H_{uni}$ in order to simplify eqn. 1.12. Eqn. 1.11 and 1.12 can be written in matrix form as

$$\begin{pmatrix} h^{rf} \\ 0 \end{pmatrix} M_s = \begin{bmatrix} \left(B + i\alpha\frac{\omega}{\gamma} \right) & -i\frac{\omega}{\gamma} \\ i\frac{\omega}{\gamma} & \left(A + i\alpha\frac{\omega}{\gamma} \right) \end{bmatrix} \begin{pmatrix} m_y \\ m_z \end{pmatrix}. \tag{1.13}$$

Since h^{rf} is applied in the y direction we are more interested in m_y, which is in the plane of the magnetic film . Writing eqn. 1.13 in terms of m_y:

$$h^{rf}M_s = m_y\left[\left(B + i\alpha\frac{\omega}{\gamma}\right) - \frac{\left(\frac{\omega}{\gamma}\right)^2}{\left(A + i\alpha\frac{\omega}{\gamma}\right)}\right] = m_y\left[\frac{\left(A + i\alpha\frac{\omega}{\gamma}\right)\left(B + i\alpha\frac{\omega}{\gamma}\right) - \left(\frac{\omega}{\gamma}\right)^2}{\left(A + i\alpha\frac{\omega}{\gamma}\right)}\right].$$

The susceptibility tensor as described by Polder [6], which relates magnetization components and h^{rf} is seen as:

$$\begin{pmatrix} m_y \\ m_z \end{pmatrix} = \overline{\overline{\chi}}\mathbf{h} = \begin{bmatrix} \chi_{yy} & \chi_{yz} \\ \chi_{zy} & \chi_{zz} \end{bmatrix}\begin{pmatrix} h^{rf} \\ 0 \end{pmatrix}. \tag{1.14}$$

In our configuration the microwave field h^{rf} is applied in the y direction, therefore the χ_{yy} component of the susceptibility tensor is important for us.

$$\chi_{yy} = \chi'_{yy} + i\chi'_{yy} = \frac{m_y}{h^{rf}} = M_s\frac{\left(A + i\alpha\frac{\omega}{\gamma}\right)}{\left(A + i\alpha\frac{\omega}{\gamma}\right)\left(B + i\alpha\frac{\omega}{\gamma}\right) - \left(\frac{\omega}{\gamma}\right)^2} \tag{1.15}$$

$$\frac{m_y}{h^{rf}M_s} = \frac{\left(A + i\alpha\frac{\omega}{\gamma}\right)}{\left[AB - \left(\frac{\omega}{\gamma}\right)^2(\alpha^2+1) + i\alpha\frac{\omega}{\gamma}(A+B)\right]}$$

$$\frac{m_y}{h^{rf}M_s} = \frac{\left(A + i\alpha\frac{\omega}{\gamma}\right)\left[AB - \left(\frac{\omega}{\gamma}\right)^2(\alpha^2+1) - i\alpha\frac{\omega}{\gamma}(A+B)\right]}{\left[\left\{AB - \left(\frac{\omega}{\gamma}\right)^2(\alpha^2+1)\right\}^2 + \left\{\alpha\frac{\omega}{\gamma}(A+B)\right\}^2\right]} \tag{1.16}$$

Resonance condition and Kittel law

The resonance condition for the magnetization is obtained when the denominator of eqn. 1.16 becomes minimum, i.e., when m_y becomes maximum for a given h^{rf}. Therefore we can write

$$\left\{AB - \left(\frac{\omega}{\gamma}\right)^2(\alpha^2+1)\right\}^2 = 0$$

Since $\alpha \ll 1$; α^2 can be ignored, which leads to $\left(\frac{\omega_{res}}{\gamma}\right)^2 = AB$. Replacing A and B with their original form:

$$\left(\frac{\omega_{res}}{\gamma}\right)^2 = \left(M_{eff} + H_{ext} + H_{uni}\right)\left(H_{ext} + H_{uni}\right) \tag{1.17}$$

This equation is known as the Kittel resonance formula. We note that this resonance condition is determined for the condition when the magnetization and the applied microwave (driving) field h^{rf} are in the film plane. In this thesis work we are interested in the resonance condition for this kind of configuration.

Real and imaginary parts of susceptibility

From eqn. 1.16 we determine the real component of χ_{yy}:

$$\chi'_{yy} = M_s \frac{\left(A\left\{AB - \left(\frac{\omega}{\gamma}\right)^2\right\} + \left(\alpha\frac{\omega}{\gamma}\right)^2 B\right)}{\left[\left\{AB - \left(\frac{\omega}{\gamma}\right)^2\right\}^2 + \left\{\alpha\frac{\omega}{\gamma}\left(A+B\right)\right\}^2\right]}$$

Since $A \gg \alpha^2 B$; the real part of χ_{yy} is simplified as:

$$\chi'_{yy} = \frac{M_s A\left\{\left(\frac{\omega_{res}}{\gamma}\right)^2 - \left(\frac{\omega}{\gamma}\right)^2\right\}}{\left[\left\{\left(\frac{\omega_{res}}{\gamma}\right)^2 - \left(\frac{\omega}{\gamma}\right)^2\right\}^2 + \left\{\alpha\frac{\omega}{\gamma}\left(A+B\right)\right\}^2\right]} \tag{1.18}$$

The imaginary component is written as

$$\chi''_{yy} = M_s \frac{\left[\alpha\frac{\omega}{\gamma}\left\{AB - \left(\frac{\omega}{\gamma}\right)^2\left(\alpha^2+1\right)\right\} - \alpha\frac{\omega}{\gamma}\left(A+B\right)A\right]}{\left[\left\{AB - \left(\frac{\omega}{\gamma}\right)^2\right\}^2 + \left\{\alpha\frac{\omega}{\gamma}\left(A+B\right)\right\}^2\right]}$$

$$\chi''_{yy} = \frac{-\alpha\left(\frac{\omega}{\gamma}\right)M_s\left\{A^2 + \left(\frac{\omega}{\gamma}\right)^2\right\}}{\left[\left\{AB - \left(\frac{\omega}{\gamma}\right)^2\right\}^2 + \left\{\alpha\frac{\omega}{\gamma}\left(A+B\right)\right\}^2\right]} \tag{1.19}$$

χ'_{yy} is the real component of susceptibility which is associated with the dispersive magnetic response and χ''_{yy} is the imaginary component associated with absorptive or irreversible process in the magnetic system which arise from energy dissipation in the system (see Figure 1.6). The real part χ'_{yy} represents the component of m_y which is in

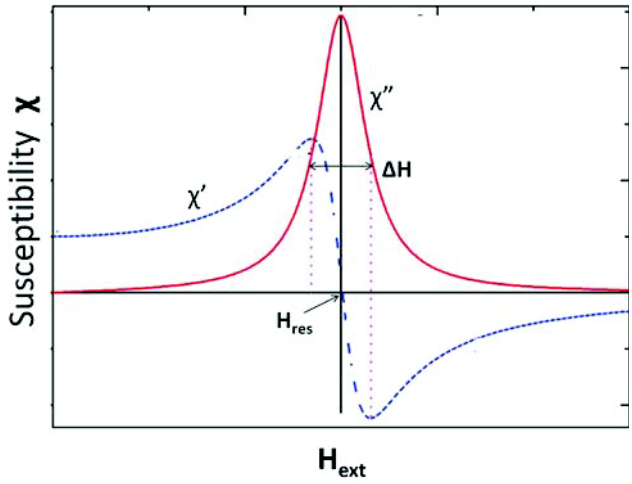

Figure 1.6: Real (blue dashed) and imaginary (red line) part of the complex susceptibility χ'_{yy} and χ''_{yy}.

phase with h^{rf}, while χ''_{yy} is the component which is delayed by a phase angle of 90° from h^{rf}. Therefore, at ω_{res}; $\chi'_{yy}(\omega_{res}) = 0$ and χ''_{yy} is max.

Susceptibility and absorption of power

In the last section we have determined the resonance condition, now we look at the energy that is absorbed to reach the resonance. The total magnetic field acting on the magnetization is seen as $\mathbf{H_{Tot}} = (\mathrm{H_{ext}}+\mathrm{H_{uni}})\,\hat{\mathbf{x}} + h^{rf}\hat{\mathbf{y}} - \frac{M_{eff}}{M_s} m_z \hat{\mathbf{z}}$. Only $h^{rf} = Re\left(\tilde{h}^{rf} e^{i\omega t}\right)$ in this equation is time varying. With the application of the time varying perturbation field h^{rf} (microwave field) the magnetization can be written as $\mathbf{M} = M_{eff}\,\hat{x} + m_y\,\hat{y}$. The $\hat{m}_z$ component is ignored since it's magnitude is much smaller compared to the other ones. When this magnetization is subjected to an external magnetic field, the time varying Zeeman energy is defines as:

$$\frac{d\epsilon_{zee}}{dt} = -\mu_0\left(\frac{d\mathbf{H_{Tot}}}{dt}\cdot\mathbf{M} + \mathbf{H_{Tot}}\cdot\frac{d\mathbf{M}}{dt}\right) \Rightarrow -\mu_0\left(m_y\frac{dh^{rf}}{dt} + h^{rf}\frac{dm_y}{dt}\right)$$

m_y can be written as: $m_y = Re\left(\chi_{yy}h^{rf}\right) = (\chi'_{yy} + i\chi''_{yy})(h^{rf}\cos\omega t + ih^{rf}\sin\omega t) = \chi'_{yy}h^{rf}\cos\omega t - \chi''_{yy}h^{rf}\sin\omega t$. Therefore the above equation for the Zeeman energy becomes $\frac{d\epsilon_{zee}}{dt} = -\mu_0 2 m_y \frac{dh^{rf}}{dt}$). The instantaneous absorbed power, assuming positive for work done on the system and lowering its energy is seen as: $P(t) = \frac{d\epsilon_{zee}}{dt} = -\mu_0 2 m_y \frac{dh^{rf}}{dt}$). We arrive at

$$P(t) = -2\mu_0 h^{rf}\left(\chi'_{yy}\cos\omega t - \chi''_{yy}\sin\omega t\right)\frac{dh^{rf}}{dt} = 2\mu_0\left(h^{rf}\right)^2\omega\left(\chi'_{yy}\cos\omega t\sin\omega t + \chi''_{yy}\sin^2\omega t\right).$$

The average absorbed power can be calculated over one cycle $T = \frac{2\pi}{\omega}$ using the mean value theorem,

$$\langle P\rangle = \frac{\omega}{2\pi}\int_0^{\frac{2\pi}{\omega}} P(t)dt \Rightarrow \mu_0\omega\chi''_{yy}(h^{rf})^2. \tag{1.20}$$

We see that the absorbed power contains only the imaginary part of the susceptibility which is a Lorentzian.

Linewidth: By performing ferromagnetic resonance measurements, power absorption characteristic can be obtained which is Lorentzian in nature. The full width half maxima (FWHM) $\triangle H_{1/2}$ gives the linewidth of the Lorentzian which contains information about the relaxation of the magnetic system. However, it is found that experimentally it is often easier to measure the differential absorption $\partial\chi''_{yy}/\partial H$. Therefore the measured absorption characteristics is a derivative of Lorentzian, with positive and negative extrema at the inflection points and zero at the peak of $\chi''_{yy}(H)$. The peak-to-peak spacing in $\chi''_{yy}(H)$ is measured as ΔH_{pp} . The FWHM of the conventional Lorentzian $\triangle H_{1/2}$ relates to the peak-to-peak linewidth $\triangle H_{pp}$ through: $\triangle H_{pp} = \frac{1}{\sqrt{3}}\triangle H_{1/2}$. Since sample inhomogeneity can also contribute to damping, it needs to be separated from the Gilbert damping, which can be done by using the relation[7]:

$$\Delta H_{pp}(\omega) = \Delta H_0 + \left(2/\sqrt{3}\right)\alpha\omega/|\gamma|. \tag{1.21}$$

The primary consequence of Gilbert damping is that the linewidth $\triangle H$ is proportional to the frequency, with proportionality given by the damping α.

1.6 Relaxation mechanisms

The introduction of damping in the last section was phenomenological and it's origin wasn't discussed. In fact the clear understanding of the origin of Gilbert damping in the metallic systems is still under debate, and there are many possible phenomena, which might contribute to it. In this section we will go through several of those possible phenomena which could contribute to damping. First of all we should keep in mind that damping of a thin magnetic layer is very much sample dependent. It is considered to have intrinsic

and extrinsic contributions. The intrinsic contribution comes from the scattering of spin waves with electrons and phonons. Since electrons and phonons are an integral part of the system, the intrinsic contribution in damping is very much unavoidable. Whereas the extrinsic contribution in damping are made by structural defects, interfacial effects, compositional defects, nonlocal effects. Also there are nonlocal phenomena which can contribute to damping. In this thesis work we are primarily interested in the study of nonlocal damping contribution.

1.6.1 Intrinsic Damping

Intrinsic damping depends very much on the ferromagnetic material. It can have contributions coming from eddy currents, scattering of conduction electrons with magnons, phonon drag. Since phonons and magnons are an integral part of a magnetic system, at finite temperature the presence of phonons and magnons can't be avoided. Also in case of alloys, there is a presence of inhomogeneous electron potential. All of these perturbations affect intrinsic interactions such as exchange couplings, dipole-dipole interactions, hence magnetic properties (anisotropy) are affected. Since all these components are very much an intrinsic part of a magnetic system, these contributions to the relaxation process are treated as intrinsic processes. Therefore, under a well defined thermodynamic condition, the smallest measured damping should be treated as intrinsic. Unfortunately, performing experiments to measure true intrinsic damping it quite difficult since creating an ideal sample or an ideal environment is very difficult, but within a vary small error range this can be done.

Scattering with itinerant conduction electrons: Spin flip

For metallic systems, the main contribution in intrinsic damping comes from the incoherent spin flip scattering of itinerant conduction electrons, caused by phonon and magnons. The presence of itinerant conduction electrons, in metallic ferromagnets, are primarily responsible for metallic ferromagnets to have larger damping compared to their insulating counterparts. There are two mechanisms which could give rise to this type of scattering.

(a) It is thought that (Kambersky) single-electron spin-flip scattering contributes most in intrinsic damping. This process involves scattering of itinerant electrons with energy $E(k,\uparrow)$ with magnon of energy $\hbar\omega_q$. For uniform ferromagnetic resonance, a finite cone angle θ is the expression of a finite number of uniform-mode $q = 0$ spin waves (magnons) excited in the system (see Figure 1.7). Each magnon annihilated by a collision with a

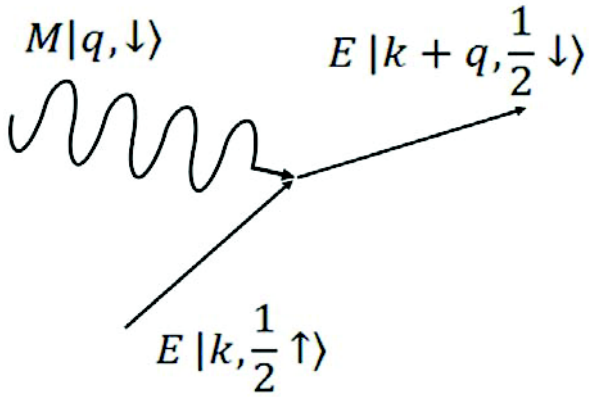

Figure 1.7: A spin wave with energy $E\left|k,\,\frac{1}{2}\uparrow\right\rangle$ collides with an electron in state $M\,|q,\,\downarrow\rangle$ changing its spin and momentum state to $E\left|k+q,\,\frac{1}{2}\downarrow\right\rangle$.

mobile electron in the ferromagnet will close down the cone angle and gradually cause M to align with H. Since the energy of magnons ($\hbar\omega_q = 4.1\mu eV/GHz \times f$) is quite small compared to that of splitting of spin up ad spin down band (˜ 1eV), conservation of energy is not possible in this process. This eventually results in flipping the spin of the itinerant conduction electron and reaching the final energy $E(k+q,\downarrow)$. Therefore, it is lost for the precession motion. This is possible due to the spin-orbit interaction, which creates a non-zero scattering probability between the two spin states[8]. This process is believed to be a dominant contribution in metallic damping and also known as spin-orbit damping. The spin flip rate which is defined as the inverse of spin flip time reads as $1/\tau_{flip} = (g_L - 2)^2/\tau_{orb}$, where τ_{orb} is the orbital relaxation time and g_L is the Lande g-factor[9]. As the Lande g-factor depends on the ratio of spin to orbital momentum[7], this indicates the importance of the spin-orbit coupling for damping in metals.

(b) It is known that the shape of the Fermi surface in a ferromagnetic metal changes with the change of direction of the magnetization [8]. Therefore a magnetization under precession causes a periodical variation of the Fermi surface due to spin-orbit coupling, which is also known as breathing of Fermi surface[10]. The process of itinerant electrons adapting to the changed Fermi surface all the time is a dissipative process, since it introduces a dephasing between the magnetization precession and the periodical variation. Therefore the re-population of the Fermi surface leads to relaxation for the scattered itinerant electron. Note that, this contribution is 'Gilbert' like contribution to the damping, which also depends on the spin-orbit coupling and is proportional to $\tau_{orb}(g_L - 2)^2$. This is in contrast to the case above, which is proportional to the resistivity. Therefore, this contribution is conductivity like as it is proportionality to τ_{orb}. Since this contribution

depends on the conductivity, the effect is more dominant at low temperatures.

Seeking examples for this two mechanism, we have found that at low temperatures, the above mentioned conductivity like mechanism (b) causes appreciable contribution in damping for Ni and Co, while for Fe or its alloys this was not observed [11]. At low temperature this contribution is dominant as it is conductivity like. It is thought that for NI, Co; near the Fermi energy E_F, degeneracy due to band-crossing exist, which are lifted by the spin orbit interaction, hence contributed strongly to damping. For Fe, this special feature is missing in its band structure, and therefore this type of contribution in damping wasn't observed at low temperatures. For, alloy's the absence of this contribution could be interpreted based on their reduced mean free path (short spin diffusion length) [11].

In summary, the two processes (a) and (b) both lead to a Gilbert-like damping term, i.e. to an α which is constant with resonance frequency. However, depending on temperature (a) and (b) do not necessarily contribute equally to the relaxation, as (a) is proportional to the resistivity, while (b) is proportional to the conductivity. This is demonstrated in [12], where the temperature dependence of the relaxation is examined, as the orbital relaxation time τ_{orb} is temperature-dependent. A more detailed discussion can be found in [13].

Magnetic relaxation caused by Eddy Currents

It is observed that Eddy currents affect magnetic damping in metallic films, especially when it is thick. It starts to a play role when the thickness of the ferromagnetic layer is comparable to its skin depth. By integrating Maxwell's equation across the film thickness t, the contribution due to this effect can be evaluated. In the presence of Eddy currents the damping can be estimated by measuring the effective Gilbert damping rate (G_{eddy}) of a magnetic substance as given by Heinrich et al.[13]:

$$\frac{G_{eddy}}{(M_S\gamma)^2} = \frac{1}{6}\frac{4\pi}{c}2\sigma t^2$$

where σ is the electrical conductivity and c is the velocity of light in free space. This type of contribution to damping depends very much on the material of the ferromagnet. It turns out that when the ferromagnetic layer becomes thicker than $50nm$, this contribution might become comparable to the intrinsic damping.

1.6.2 Extrinsic Damping

The contributions in relaxation could also arise from structural defects and complex geometrical features. The contributions are known as extrinsic contribution.

Two-Magnon Scattering

An important extrinsic contribution to damping comes from two magnon scattering, which arises due to structural defects. This process was studied in detail decades ago, for ferromagnetic insulators. In metallic films, this process is analog to the elastic scattering of electrons in metals by lattice defects. In two magnon scattering processes, a magnon corresponding to an uniform precession ($k = 0$) is annihilated and another with $k \neq 0$ is created. Since this is a spin-spin process the total number of magnons is unchanged. However for $k \neq 0$ magnons the spins are not parallel to one another. The excitations of such magnons reduces the length of the magnetization. This process is better modeled with Bloch-Bloembergen (BB) (see eqn. 1.7) than with the LLG-equation which conserves the magnetization. The spin dephasing mechanism is described by the transverse relaxation time T_2 (Figure 1.4). The $k \neq 0$ magnons relaxation to the lattice, leads to an independent relaxation time T_1. The damping contributed by a two-magnon scattering process is not Gilbert-like, i.e. it is not proportional to the resonance frequency. It can easily be confused with a finite zero frequency linewidth, which is usually accounted for the sample inhomogeneity as shown in eqn. 1.21.

1.6.3 Nonlocal Damping

This type of damping contribution was first observed in magnetic double layered structure like $NM/FM1/NM/FM2/NM$. The magnetization of $FM2$ layer is assumed to be fixed, i.e. pinned and $FM1$ is considered to be a free layer. Berger, included magnon occupation number explicitly for the precession of $FM1$, in his treatment[14]. This treatment assumes that the itinerant electrons which enter $FM1$ do not assumes immediately the instantaneous direction of the precessing magnetization. This therefore leads to an exchange torque, confined to the vicinity of the $FM1/NM$ interface, directed towards the equilibrium axis. This resulting relaxation torque contributes an additional FMR linewidth for $FM1$; seen as $\triangle H_{add} \sim (\triangle\mu + \hbar\omega)$, where $\triangle\mu = \triangle\mu^{\uparrow} - \triangle\mu^{\downarrow}$ is the difference in the shift of spin up and spin down electrons at the Fermi level. $\hbar\omega$, where ω is the angular frequency of the microwave (pumping field for FMR), represents interface Gilbert damping. This interface torque is shared by all atomic layers for ultrathin mag-

netic films[15, 16]. It follows that the additional FMR linewidth is inversely proportional $(1/t_{FM})$ to the thickness of the ferromagnetic layer t_{FM}. Later on this nonlocal damping was studied rigorously by Tserkovnyak et al. using magnetoelectric circuit theory. This nonlocal additional damping is attributed to an effect called spin pumping. This thesis is based on studying this type of nonlocal damping and the details of this type of damping is discussed in Chapter 2.

Chapter 2

Spin pumping a reciprocal effect of Spin transfer torque

Current induced magnetization dynamics, where a spin polarized current is used to switch the magnetization or to create steady state precession[17] of the magnetization, has become one of the major sub-fields in present day spintronics research. Number of issues in this domain have attracted physicist all over the world. This has offered very interesting physics along with the application prospects and played a vital role in bridging fundamental research with application. This field was pioneered by Berger[14] and Slonczewski[18] who have introduced the concept of spin polarized current transferring angular momentum to the magnetization by giving a torque, better known as spin transfer torque (STT). The fact that the magnetization state can be controlled by an electrical current, instead of an applied field has opened new possibilities for device applications. Experiments were carried out, in order to confirm STT effect in magnetic heterostructures [19, 20], and the importance of this concept was soon realized.

The concept of a reciprocal effect of spin transfer torque was proposed by Berger in 1996 [14]. This effect was first studied in $FM1/NM/FM2$ type structures, where broadening of FMR linewidth (caused by $FM2$) of the precessing thin ferromagnetic layer $FM1$ was observed. Experiments were carried out by groups of Heinrich et al. (2003) and Mizukami et al. (2001) to verify this broadening of linewidth. However, each group had interpreted this effect differently, as no concrete theory was existing at that time. A rigorous theoretical development of this phenomenon, which is known as spin pumping, was provided by Tserkovnyak et al. [21, 22], for magnetic heterostructures. A direct experimental demonstration of pumped out spin current is a little challenging. A possible way to detect this is by the Inverse spin Hall effect [23]. Since the consequences of spin pumping lead to the enhancement of the relaxation rate of the magnetization, this

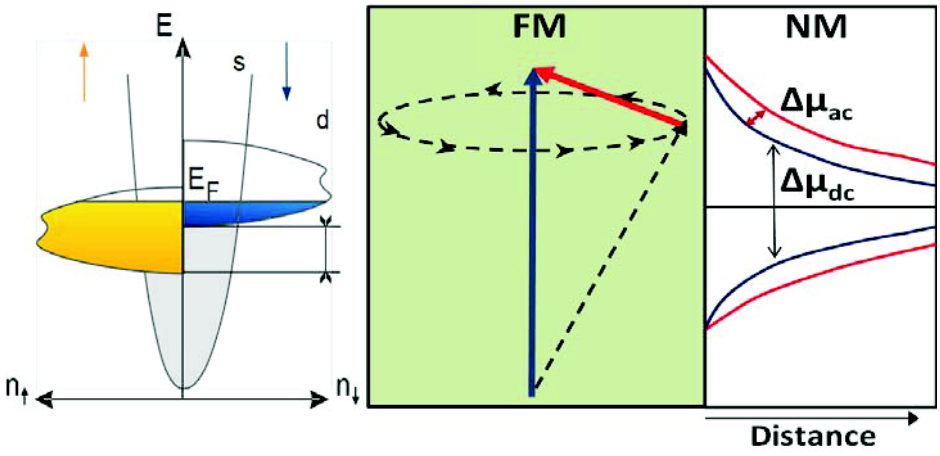

Figure 2.1: Spin accumulation in a nonmagnetic metal, adjacent to a ferromagnet. The d.c. component of spin accumulation corresponds to static magnetization, whereas the a.c. component of spin accumulation corresponds to the dynamic magnetization.

effect can also be measured, by means of measuring the broadening of FMR linewidth.

In this thesis study we deal a lot with Ferromagnetic/nonmagnetic bilayer structures. It is important for us to realize that from transport point of view, a nonmagnetic metal under normal circumstances is different than when it is in contact with a ferromagnetic layer. In Figure 2.1, using schematics, we demonstrate this effect. We know that the density of states (DOS) for spin up and spin down electrons at the Fermi level is different in the ferromagnet, which is also known as the imbalance of chemical potential ($\triangle\mu$). In case of a normal metal under normal circumstances, the DOS for spin up and spin down electrons is same. hence $\triangle\mu = 0$. However, when this normal metal is in contact with the ferromagnet, we find that just at the interface $\triangle\mu \neq 0$. In fact $\triangle\mu$ stays non zero within the normal metal over certain thickness range. Although this thickness range is not very well known. This chemical imbalance in the normal metal (shown by the blue lines), in contact with the ferromagnet creates a spin accumulation which can be indirectly measured. Since the chemical imbalance in the normal metal is created by the static magnetization, it is also known as the d.c. part of chemical imbalance in NM. For a dynamic magnetization, another component, which is known as the a.c. component of chemical imbalance (shown by the red lines) needs to be considered on top of the d.c. contribution, which is also measurable. Our study of spin pumping basically takes into account this a.c. component of chemical potential in NM. However, we will not quantify this component via electrical measurement, rather we will study the magnetization dynamics of the ferromagnet which is affected by this.

In this chapter, we will first introduce some fundamental concepts such as spin and

charge accumulation, Sharvin resistance, spin mixing conductances etc, which are necessary to understand spin current transport in magnetic heterostrutures using magnetoelectric circuit theory. Then we will present the phenomenon of spin transfer torque. We will go through the derivation of different current components following the magnetoelectric circuit theory of Tserkovnyak & Brataas [22, 24, 25]. In the following section, we will introduce the reciprocal effect of STT, spin pumping, and follow the description of Tserkovnyak & Brataas et al.'s work. This will present the principle idea of spin pumping, and how to quantify several spin current transport related parameters. We will consider different types of magnetic heterostructures like: FM/NM, $FM1/NM/FM2$, $FM/NM1/NM2$, and show the predicted effects according to the spin pumping model. In the end of this chapter we will present an overview on the state of the art, both theoretical and experimental.

Spin & charge accumulation

In a general manner *spin bias* or *spin accumulation* $\mathbf{V}^S$ is defined as the (electrical) potential difference between spin up and spin down electrons. In terms of the chemical potential $\mu_i = \frac{\partial F}{\partial n_i}$, where F is the Helmholtz free energy, the spin accumulation is given as:

$$e\mathbf{V}^S = \frac{1}{2}(\mu^{\uparrow} - \mu^{\downarrow})\mathbf{n},$$

where e is the electronic charge and $\mathbf{n}$ is the direction of the net spin accumulation. Usually in the NM side there is no spin bias but $\mathbf{V}_N^S$ can be created artificially by creating an imbalance in the population of the spin up and spin down electrons.

The regular voltage bias (or charge bias) V^C is a scalar quantity and it is determined by the net charge flow in a particular direction, which is defined as:

$$eV^C = \frac{1}{2}(\mu^{\uparrow} + \mu^{\downarrow}).$$

On the FM side,$\mathbf{V}_F^S$ is aligned with $\mathbf{m}$ (we have assumed that $\mathbf{m}$ is aligned in the z direction); $\mathbf{V}_F^S = V_F^S\mathbf{m}$. It is assumed that the magnetization $\mathbf{m}$ of FM is along the z direction and the interface normal is along x and the interface is lying in the $y-z$ plane and the charge accumulation is viewed as V_F^C(see Figure 2.3(b)).

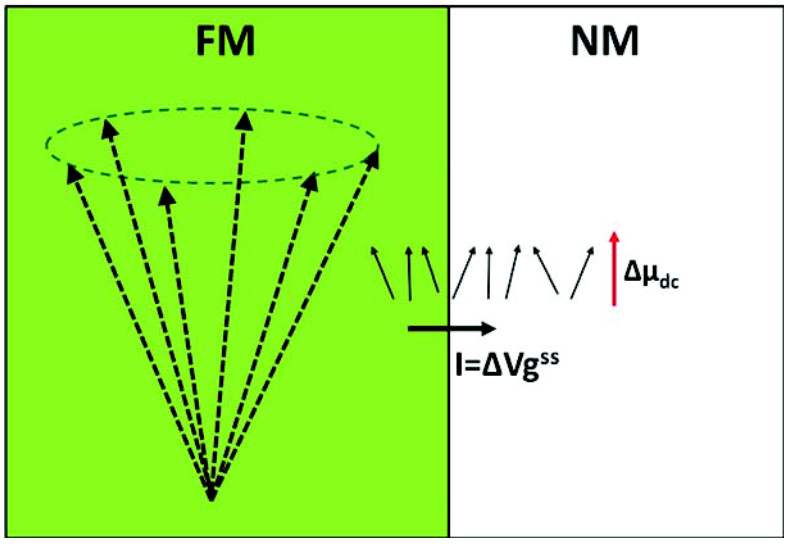

Figure 2.2: Spin dependent conductance for FM/NM bilayer structure.

Spin mixing conductance

In spin current transport, it is known that the conductivity is spin dependent. This spin dependent conductance becomes a bit complicated while studying transport in a FM/NM bilayer structure or ferromagnetic heterostructures. In these type of structure a term known as spin mixing conductance is more used than just spin dependent conductance. For us, it is a little difficult to release this term for FM/NM bilayer structure without much theoretical basics. However, we would like to understand this term in a very crude manner. For this we consider a FM/NM bilayer in Figure 2.1, which is very similar to Figure 2.1.

We use the concept of induced chemical potential in the NM by FM we write from Figure 2.1. The spin current for this FM/NM bilayer can be written in terms of a potential difference ($\triangle V$) created by spin accumulation and a conductance matrix: $I = \triangle V g^{ss}$. This conductance matrix can be written as:

$$g^{ss} = \begin{pmatrix} g^{\uparrow\uparrow} & g^{\uparrow\downarrow} \\ g^{\downarrow\uparrow} & g^{\downarrow\downarrow} \end{pmatrix}.$$

Here, $g^{\uparrow\uparrow}$and $g^{\downarrow\downarrow}$are the *spin dependent conductances,* which are to be used for collinear cases, i.e. when the spin current traveling from FM side to NM side are parallel or antiparallel to the local spin accumulation in NM. Whereas $g^{\uparrow\downarrow}$and $g^{\downarrow\uparrow}$ are used for non collinear cases. When the magnetization is dynamic, this two spin mixing conductances becomes very important. In this chapter, while going through the basics of spin transfer

torque and spin pumping, we will see that the non collinear cases are the one which basically drives these two phenomenons.

2.1 Spin Transfer torque

The dynamics of the magnetization is governed by the Landau-Lifshitz-Gilbert (LLG) equation (see Chapter 1). The first term describes the precession of the magnetization around the effective field $\mathbf{H}_{eff}$ and the second term represents the damping (α is the damping parameter) in the system which brings it back to equilibrium (discussed in Chapter 1):

$$\frac{d\mathbf{m}}{dt} = -\gamma\left(\mathbf{m} \times \mathbf{H}_{\mathit{eff}}\right) + \alpha\left(\mathbf{m} \times \frac{d\mathbf{m}}{dt}\right). \tag{2.1}$$

In 1996 Berger and Slonczewski predicted that a dc current can excite and even reverse the relative magnetization of a magnetic layer. This could be understood by taking into account the coupling of spin polarized electrons and the magnetization. According to this effect, when a spin polarized current enters a ferromagnet, if it is non collinear to the magnetization of the ferromagnet then it transfers angular momentum to the magnetization of the ferromagnet. This angular momentum transfer is transverse to the magnetization direction. The thickness range, within which the transfer of angular momentum takes place, is very short[26, 27].

For better understanding of this effect, we consider a spin polarized current $\mathbf{I}_S$ (directed of this vector is along the net spin polarization) incident on the NM/FM interface, coming from the NM side as shown in Figure 2.3. The loss of the transverse component of spin angular momentum at the normal metal/ ferromagnet interface can be written as $[\mathbf{I}_S - (\mathbf{I_S} \cdot \mathbf{m})\,\mathbf{m}] = -(\mathbf{m} \times (\mathbf{m} \times \mathbf{I}_S))$. This torque will be shared between all the magnetic moments or M_sV of the ferromagnetic layer of volume V. This exerted torque on the ferromagnetic layer is equal to the rate of change of the total magnetic moment of the ferromagnetic layer $\partial(\mathbf{m}M_SV)/\partial t\,|_{STT}$, seen as[18]:

$$\tau_{STT} = \left(\frac{\partial \mathbf{m}}{\partial t}\right)_{STT} = -\frac{\gamma}{M_SV}\left(\mathbf{m} \times (\mathbf{m} \times \mathbf{I}_S)\right). \tag{2.2}$$

So far we haven't discussed how $\mathbf{I}_S$ is generated. First of all, $\mathbf{I}_S$ can be a charge current with net spin polarization (called spin polarized charge current), or it can be a pure spin current (which has no net charge flow but a net spin flow only). There are several ways to generate these two types of current. The usual method to generate spin polarized charge current is by applying a bias voltage in a $FM1/NM/FM2$ system,

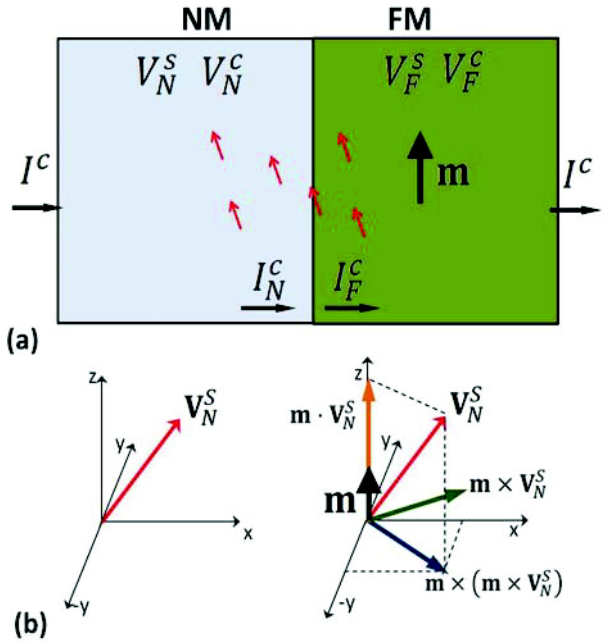

Figure 2.3: Schematic illustration of the spin transfer torque in layered NM/FM structure. Spin accumulation $\mathbf{V}_N^S$ in the NM induces a spin-transfer torque $\boldsymbol{\tau}_{STT}^{bias}$ on FM.

where $FM1$ is a highly coercive magnetic layer known as polarizer and $FM2$ is a free magnetic layer [28, 18, 29]. When charge current is passed through a polarizing $FM1$ layer, it becomes spin polarized with the polarization parallel to the magnetization of $FM1$. This spin polarized charge current when passed, through the free layer $FM2$, will exert a torque on $FM2$. This induces reversal or oscillation of the magnetization.

For the generation of pure spin current, spin pumping method can be used. In this method, precession of magnetization drives a pure spin current into the adjacent normal metals[30, 21]. We are using this mechanism to generate a pure spin current and inject it into the layers adjacent to the precessing ferromagnetic layer.

For the normal metal (NM)/ Ferromagnet (FM) system (see Figure 2.3(a)), Brataas et al. have done their calculation for a net charge current flowing in the circuit by using magnetoelectric circuit theory. This theory is based on Kirchhoff's theorem for electrical circuits, where the main idea is to understand a complicated electrical circuit in terms of current-voltage across a single resistance (or impedance) element. In this theory, the central idea of Kirchhoff's is generalized for electronic circuits incorporating ferromagnetic and nonmagnetic metals.

Spin current components for STT

Brataas et al. [24] have simplified the derivations, for spin current components in NM/FM structure, shown in Figure 2.3, by assuming a non-equilibrium magnetization

or spin accumulation $\mathbf{V}_N^S$ and a charge accumulation V_N^C already existing in the normal metal layer. We will come back to the point of already existing spin accumulation $\mathbf{V}_N^S$, while discussing spin pumping in the next section. We define, the spin up current $I^{\uparrow}$ (parallel to $\mathbf{m}$) and spin down current $I^{\downarrow}$ (anti-parallel to $\mathbf{m}$) flowing in the circuit. The total charge current (a scalar quantity) is simply defined as $I^C = I^{\uparrow} + I^{\downarrow}$, which is continuous across the interface and reads as: $I_N^C = I_F^C = I^C$. The spin dependent interface conductances (for NM/FM interface) for spin up and spin down electrons are defined as $g^{\uparrow}$, $g^{\downarrow}$. We note that the spin current flowing from NM to FM has a longitudinal (parallel to $\mathbf{m}$) $\mathbf{I}_N^S \parallel$ and a transverse (perpendicular to $\mathbf{m}$) component $\mathbf{I}_N^S \perp$[24]. It is considered that $\mathbf{V}_N^S$ and $\mathbf{V}_F^S$ are non collinear. Therefore the current which flows from NM to FM can be decomposed into three polarization components. These components are:

(1) longitudinal component, which is collinear to $\mathbf{V}_N^S$ (see Figure 2.3(b)),

(2) transverse component, which is perpendicular to $\mathbf{V}_N^S$ in the plane of $\mathbf{m}$ and $\mathbf{V}_N^S$ (this plane is defined as the perpendicular plane to the direction $\mathbf{m} \times \mathbf{V}_N^S$) or,

(3) transverse component, lying in the plane $\mathbf{m} \times \left(\mathbf{m} \times \mathbf{V}_N^S\right)$) (see Figure 2.3(b)).

The longitudinal component of the spin current $I_N^S \parallel = \left(I^{\uparrow} - I^{\downarrow}\right)\mathbf{m}$ is found to be:

$$\mathbf{I}_N^S \parallel = \mathbf{m}\left[g^{\uparrow}\left[\left(V_N^C - V_F^C\right) + \mathbf{m}\cdot\mathbf{V}_N^S\right] + g^{\downarrow}\left[\left(V_N^C - V_F^C\right) + \mathbf{m}\cdot\mathbf{V}_N^S\right]\right]. \tag{2.3}$$

The longitudinal component do not contribute to the spin transfer torque, but the transverse components do. However, since the transverse component is absorbed within a very short length after entering the ferromagnet, and not continuous across the leads, it cannot be calculated using Ohm's law. In the next section we discuss the absorption or loss of spin current in the vicinity of the interface.

Spin dephasing

To understand the transverse component of spin current moving into the ferromagnet, we have to realize that a spin state which is not collinear to the magnetization is not an eigenstate of the ferromagnet (for both majority and minority spins). However, with arbitrary spin direction a Bloch state can be considered as a coherent linear combination of spin eigenstates that are associated with different Fermi wave vectors $k_F^{\uparrow}$ and $k_F^{\downarrow}$ at the Fermi energy level [24]. Defining $k_{F,x}^{\uparrow}$ and $k_{F,x}^{\downarrow}$ as the components of spin-dependent wave vectors perpendicular to the interface, it was shown that the spin up and spin down electrons oscillate as a function of x as $\cos\left(k_{F,x}^{\uparrow} - k_{F,x}^{\downarrow}\right)x$[31]. This can be simply viewed as a precession of the spin states in the exchange field of the magnet with period $2\pi/|k_{F,x}^{\uparrow} - k_{F,x}^{\downarrow}|$[31, 32]. Realistically, incident electrons, which are coming from various directions correspond to states from all parts of the Fermi surface. Spins which travel different paths would have precessed by different angles around the z axis, which will

mean that their x and y components will not add constructively, resulting in classical *dephasing*, which is equivalent to the absorption of the transverse component within a length scale known as transverse spin-dephasing length (or magnetic coherence length) given as $\lambda_C \sim \pi/|k^{\uparrow}_{F,x} - k^{\downarrow}_{F,x}|$. Using first principle calculations this length was predicted to be few atomic lattice constants of the ferromagnet[31, 32]. Although experimentally this length scale was never probed accurately. One of our central results for this thesis work deals with the study of this transverse spin-dephasing length (see Chapter 5) for various ferromagnets ($NiFe$, $CoFeB$, Co), and anti ferromagnet ($MnIr$). We use spin pumping mechanism for creating pure spin current, injecting them into these materials [33, 34], and study it's absorption.

Torque term

We have seen above that the transverse component is not conserved across the normal metal–ferromagnet interface as it vanishes inside the ferromagnet. Therefore Brataas et al. have evaluated the transverse spin current on the NM side of the interface [24]. They have calculated the *magnitude* of the transverse spin current $I^S_N \perp$ assuming the electronic structure of the majority spin of the FM is matched to that of the NM. As mentioned in one of the previous sections, the transverse component of spin current in the normal metal can either be in the plane given by the magnetization and the spin accumulation vector$\left(\mathbf{m} \times \mathbf{V}^S_N\right)$, or normal to this plane, $\mathbf{m} \times \left(\mathbf{V}^S_N \times \mathbf{m}\right)$. Considering an ideal NM/FM interface, the transverse spin-current is determined using these two terms, combined with the real and imaginary part of the spin-mixing conductance $\tilde{g}^{\uparrow\downarrow} (= \tilde{g}^{\uparrow\downarrow}_r + i\tilde{g}^{\uparrow\downarrow}_i)$ as:

$$\mathbf{I}^{S,bias}_N \perp = -2\tilde{g}^{\uparrow\downarrow}_r \mathbf{m} \times \left(\mathbf{m} \times \mathbf{V}^S_N\right) - 2\tilde{g}^{\uparrow\downarrow}_i \left(\mathbf{m} \times \mathbf{V}^S_N\right). \tag{2.4}$$

For the details of how the spin mixing conductances ($\tilde{g}^{\uparrow\downarrow}_r$, $\tilde{g}^{\uparrow\downarrow}_i$) are related to spin dependent conductance ($g^{\uparrow}$, $g^{\downarrow}$), we refer to [24]. For convenience we denote the spin current as $\mathbf{I}^{S,bias}_N \perp$ since it is driven by the voltage $\mathbf{V}^S_N$, which is applied (created) externally and not existing naturally in the nonmagnet. On the ferromagnetic side of the interface at a distance larger than λ_C: $\mathbf{I}^S_F \perp = 0$. As discussed earlier the divergence of transverse component of spin current at the interface gives rise to the torque

$$\boldsymbol{\tau}^{bias}_{STT} = -\frac{\gamma}{M_S V}\left[\tilde{g}^{\uparrow\downarrow}_r \mathbf{m} \times \left(\mathbf{m} \times \mathbf{V}^S_N\right) + \tilde{g}^{\uparrow\downarrow}_i \left(\mathbf{m} \times \mathbf{V}^S_N\right)\right]. \tag{2.5}$$

The first term which is proportional to $\mathbf{m} \times \left(\mathbf{m} \times \mathbf{V}^S_N\right)$ corresponds to the torque term introduced first by Slonczewski. The second term, proportional to $\left(\mathbf{m} \times \mathbf{V}^S_N\right)$, acts as an effective magnetic field on $\mathbf{m}$. In a metallic system the real part of spin mixing conductance dominates over the imaginary part $g^{\uparrow\downarrow}_i \ll g^{\uparrow\downarrow}_r$making the Slonczewski torque

term more dominant. Adding this torque to the Landau-Lifshitz-Gilbert equation leads to the Landau-Lifshitz-Gilbert-Slonczewski (LLGS) equation:

$$\frac{d\mathbf{m}}{dt} = -\gamma\left(\mathbf{m}\times\mathbf{H}_{\mathit{eff}}\right) + \alpha\left(\mathbf{m}\times\frac{d\mathbf{m}}{dt}\right) + \boldsymbol{\tau}_{STT}^{bias} \tag{2.6}$$

The phenomenon of spin transfer torque was just one side of the coin. Since spin current can move magnetization it is evident to consider a reciprocal effect where moving magnetization is able to generate pure spin current. This phenomenon is known as spin pumping and this thesis deals with studying and verifying this effect and its consequences. Note that the we have not yet discussed the origin of $\mathbf{V}_N^S$. We move forward to the next section which will provide a basis to understand the origin of this spin accumulation.

2.2 Spin pumping: Dynamic coupling

Since spin currents can rotate (move) magnetization, it is quite natural to consider it's reciprocal effect, i.e. the generation of spin current by the movement (precession) of magnetization. In the 1970's, it was recognized that the dynamics of spin is associated with spin currents in a normal metal. The work presented by Janossy et al. and Silsbee et al, predicts a coupling between the magnetization and the spin accumulation in it's adjacent normal metal [35, 36]. However, a good theoretical understanding was missing at that time. More recently, an additional, nonlocal damping term has been identified theoretically by Tserkovnyak, Brataas, Bauer, and co-workers at Delft, and experimentally by the groups of Mizukami (Tohuku) and Heinrich (Simon Fraser) indicating the coupling of magnetization and spin accumulation in its adjacent normal metal[30, 21, 37, 38, 39, 27]. A detailed theoretical explanation was sought using scattering theory for spin currents induced by magnetization dynamics by Tserkovnyak et al.[22], based on the idea of adiabatic quantum pumping[40], hence the name "spin pumping". This effect is viewed as a reciprocal effect of spin transfer torque. In this process, pure spin currents are driven ("pumped") out of the ferromagnet to its adjacent normal metal. This pumping of spin current is associated with the loss of angular momentum by the ferromagnet which shows off in it's damping, as discussed below in more detail.

In Figure 2.4, we consider a FM/NM bilayer without any voltage bias. As no bias is applied and the magnetization is static, no spin or charge current flows in the circuit. If the magnetization starts to precess (e.g. driven by a microwave field), a spin current $\mathbf{I}_N^{S,pump}$ is pumped out of the ferromagnet into the NM layer[22]. This pumped out spin current is given as[21, 30]:

$$\mathbf{I}_N^{S,pump} = \frac{\hbar}{4\pi}(g_r^{\uparrow\downarrow}\left(\mathbf{m}\times\frac{d\mathbf{m}}{dt}\right) + g_i^{\uparrow\downarrow}\frac{d\mathbf{m}}{dt}), \tag{2.7}$$

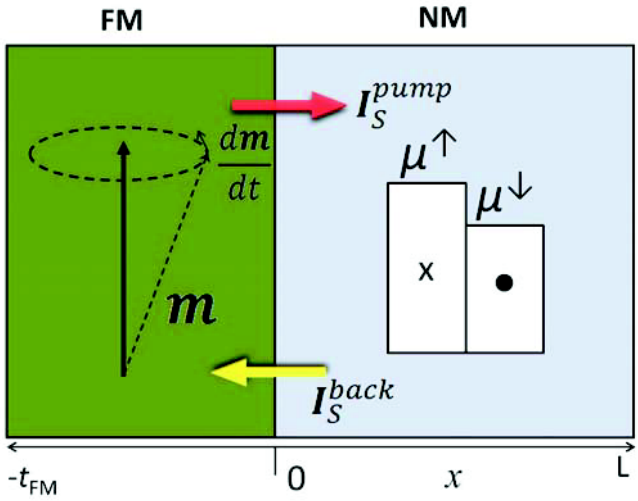

Figure 2.4: Schematic illustration of spin pumping in a FM/NM system, where the precession of magnetization $\mathbf{m}$ in the ferromagnet drives spin current $\mathbf{I}_S^{pump}$into the normal metal. Due to this non equilibrium spin accumulation is built in the normal metal, which either relaxes by spin-flip scattering or flows back into the ferromagnet as $\mathbf{I}_S^{back}$. This spin accumulation $\boldsymbol{\mu}_S(x)$ is a vector quantity and is position x dependent.

where $g_r^{\uparrow\downarrow}$ and $g_i^{\uparrow\downarrow}$ are the real and imaginary part of the transverse conductances which are material (interface) dependent. The pumped out spin current, which corresponds to a angular momentum loss, flows perpendicular to the FM/NM interface with a polarization direction $\mathbf{m}\times\frac{d\mathbf{m}}{dt}$.

While discussing the STT effect in the last section, it was assumed that the spin accumulation $\mathbf{V}_N^S$ already exist in the normal metal. As we see that spin pumping creates a spin accumulation in the adjacent nonmagnetic metals of a precessing ferromagnet, we think this could be used as the origin of $\mathbf{V}_N^S$ in the normal metal. This picture could be realized by adding Figure 2.4, from the left side of Figure 2.3, as shown in Figure 2.5.

This pumped out spin current in the normal metal can be absorbed, causing a permanent loss of angular momentum to the ferromagnet $FM1$, which is equivalent to a torque acting on its magnetization, seen as $\tau_S = -\mathbf{I_S}$. When spin current is driven back to $FM1$ (back flow of spin current), there is no net loss (or little) of angular momentum. We need to be careful about the sign of $\mathbf{I}_N^{S,pump}$, we assume it to be negative which implies angular momentum loss. Therefore, for $\left|\frac{d\mathbf{m}}{dt}\right| \neq 0$ replacing $\mathbf{I}_N^{S,bias}$ by $\mathbf{I}_N^{S,pump}$ for the torque term in equation 6 we find:

$$\frac{d\mathbf{m}}{dt} = -\gamma\mathbf{m}\times\mathbf{H}_{eff} + \alpha\mathbf{m}\times\frac{d\mathbf{m}}{dt} + \frac{\gamma\hbar}{4\pi M_S V}(g_r^{\uparrow\downarrow}\left(\mathbf{m}\times\frac{d\mathbf{m}}{dt}\right) + g_i^{\uparrow\downarrow}\frac{d\mathbf{m}}{dt}). \tag{2.8}$$

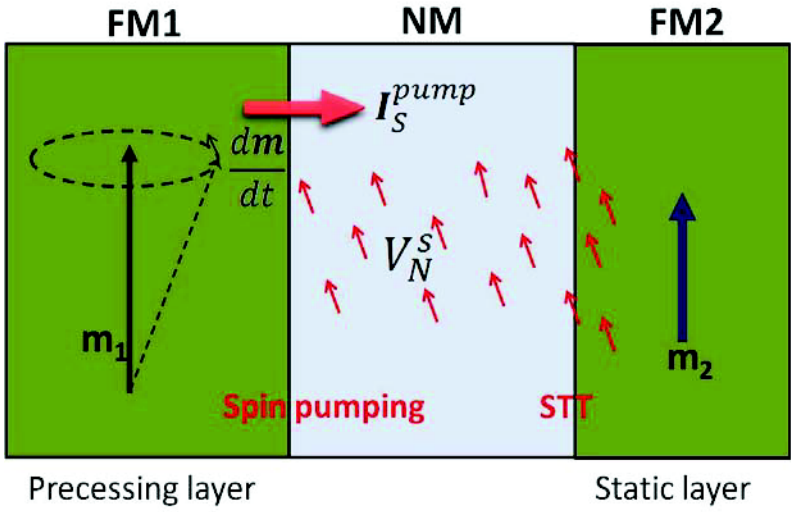

Figure 2.5: Typical $FM1/NM/FM2$ structure, where spin current is driven into NM by precessing $FM1$ layer, by spin pumping mechanism. This spin current traverse to $FM2$, where it is absorbed by STT effect.

Since $g_r^{\uparrow\downarrow} \gg g_i^{\uparrow\downarrow}$, we ignore the imaginary term added in eqn. 2.8. The term containing $g_r^{\uparrow\downarrow}$ which survives in eqn. 2.8, has the form $\mathbf{m}\times\frac{d\mathbf{m}}{dt}$, similar to that of the Gilbert damping term. Therefore this term can be treated as an additional damping: $\triangle\alpha = \frac{\gamma\hbar g_r^{\uparrow\downarrow}}{4\pi M_S V}$, acting on the precessing ferromagnet caused due to spin pumping effect. We must take a little note here. Spin pumping might not always lead to an additional damping, because a back flow of spin current from the adjacent metals to the ferromagnet might exist as well, which shows off in the magnitude of $\triangle\alpha$. We discuss about this in one of the upcoming subsections.

One important consideration made while deriving eqn. 2.8, is the *reciprocity* of the interfacial spin mixing conductances $g_r^{\uparrow\downarrow}$ and $g_i^{\uparrow\downarrow}$, meaning that these parameters are assumed to be the same for STT and spin pumping effect. Below, we look into the reciprocity statement for these quantities.

2.2.1 Reciprocity relations for spin mixing conductance:

The interfacial spin mixing conductance $g^{\uparrow\downarrow}$ determines how much spin current is passed through the interface. It was shown by Onsager reciprocity relations that in a thermodynamically reciprocal process the conductance parameters, if properly normalized, must be identical [24]. Since spin pumping and spin transfer torque are thermodynamical reciprocal processes, it was shown that the real and imaginary parts of spin mixing conductance used for STT in eqn. 2.4, and for spin pumping in eqn. 2.7, are the same, i.e. $g_r^{\uparrow\downarrow} = \tilde{g}_r^{\uparrow\downarrow}$ and $g_i^{\uparrow\downarrow} = \tilde{g}_i^{\uparrow\downarrow}$ [41]. There are two other important properties of spin mixing conductance as observed by Brataas[24]:

• $g^{\uparrow\downarrow}$ rotates spins around the magnetization axis of the ferromagnet, and

• $g_r^{\uparrow\downarrow}$ is generally larger than the average of the longitudinal spin-dependent conductances: $g^{\uparrow\downarrow} \geq \frac{1}{2}\left(g^{\uparrow} + g^{\downarrow}\right)$.

As $g_r^{\uparrow\downarrow}$ and $g_i^{\uparrow\downarrow}$ are identical for both STT and spin pumping, one can characterize these quantities accurately using either the spin pumping or spin transfer torque effect. However, it is seen that quantifying these parameters using the STT effect is quite challenging. On the other hand, using spin pumping, by exciting the homogeneous FMR mode, the transverse spin mixing conductance $g_r^{\uparrow\downarrow}$ and, $g_i^{\uparrow\downarrow}$ can be measured with enough accuracy. Therefore rather than measuring these parameters from current induced dynamics study, the values $g_r^{\uparrow\downarrow}$ and $g_i^{\uparrow\downarrow}$, as measured from spin pumping study can be directly used while analyzing more complex magnetization phenomena. This will be shown in Chapter 4 and 5, where we will extract the real part for different materials combination.

2.2.2 Back flow of spin current

As discussed above the pumped out spin current from the ferromagnet can be (1) fully absorbed by the adjacent metal, (2) fully diffused back to the ferromagnet, and (3) partially absorbed and partially diffused back to the ferromagnet. The above derived eqn. 2.8 holds good when the pumped out spin currents are fully absorbed. This was determined by Tserkovnyak et al. by considering an ideal spin bath attached to the ferromagnet, which shows the full absorption of spin current leads to additional damping $\triangle\alpha = \frac{\gamma\hbar g_r^{\uparrow\downarrow}}{4\pi M_S V}$.

However, a second case could be considered where a nonmagnetic metal of finite thickness, which is a poor spin sink, is attached to the ferromagnet from one side. For simplicity we don't consider anything attached in the other side of the ferromagnet. Tserkovnyak et al. have shown that the spin accumulation is an equilibrium property of the FM/NM system[22]. Assuming the magnetization $\mathbf{m}(t)$ starts precessing around the effective field $\mathbf{H}_{eff}$ at time t. After a short time interval δt, the magnetization slowly (i.e. adiabatically) changes to $\mathbf{m}(t+\delta t) = \mathbf{m}(t) + \delta\mathbf{m}$. For the above mentioned case of large but finite nonmagnetic reservoir, which does not flip the spin currents, a spin accumulation $\boldsymbol{\mu}_S(x) = \mu^{\uparrow}(x) - \mu^{\downarrow}(x)$ which is a function of the distance x from the FM/NM interface, is induced. Since the adiabatic assumption means the system is always in the stationary state, for a slow variation of $\mathbf{m}(t)$, this non equilibrium spin imbalance must flow back into the ferromagnet, and cancel any spin current that is generated by the magnetization precession. It was found (ref. [22]) that the non equilibrium spin accumulation for such a case is $\mu_S = \hbar\gamma H_{eff} = \hbar\omega$, where γ is the absolute gyromagnetic ratio of the ferromagnet and ω is the Larmor frequency of precession for the $\mathbf{m}(t)$ in

H_{eff}. Therefore we see that the spin up and spin down chemical potentials are split by an energy $\mu_S = \hbar\omega$, which corresponds to the precessional frequency (or frequency of the perturbation/pumping field).

It was shown by Brataas et al, [27, 24] using magnetoelectric circuit theory, that the back flow of spin current which satisfies the above condition has to be equal to the pumping current, i.e. $\mathbf{I}_S^{back} = \mathbf{I}_S^{pump}$:

$$\mathbf{I}_S^{back} = \frac{\hbar}{4\pi}(g_r^{\uparrow\downarrow}\left(\mathbf{m}\times\frac{d\mathbf{m}}{dt}\right) - g_i^{\uparrow\downarrow}\frac{d\mathbf{m}}{dt}).$$

This adiabatic pumping case is not the whole story, since a spin flip process is an integral part of magnetoelectric circuits. So far we have considered two extreme situations where adjacent (to the ferromagnet) nonmagnet is either an ideal spin sink ($\mathbf{I}_S^{back} \sim 0$) or it provides no spin flip ($\mathbf{I}_S^{back} \sim \mathbf{I}_S^{pump}$).

The third situation that we consider is when the nonmagnet is not an ideal spin sink neither it has zero spin flip rate. Therefore it provides diffusive transport to the spin current. In this case, the spin accumulation in the normal metal (following ref [22]) will read as $i\omega\boldsymbol{\mu}_S = D\partial_x^2\boldsymbol{\mu}_S - \boldsymbol{\mu}_S/\tau_{sf}$. where ω is the precession frequency, τ_{sf} is the spin flip rate and D is the diffusion coefficient of NM. After applying the boundary conditions, that at $x = 0$ the spin current is 0 and at $x = L$ (where L is the thickness at which spin current vanishes) the spin current vanished, leads us to$\boldsymbol{\mu}_S(x) = \frac{\cosh k(x-L)}{\sinh kL}\frac{2\mathbf{I}_S^{pump}}{\hbar NSDk}$, where $k = \frac{\sqrt{(1+i\omega\tau_{sf})}}{\lambda_{sd}}$ is the wave vector and $\lambda = \sqrt{D\tau_{sf}}$ is the spin diffusion length. This spin accumulation drives some part of the spin current back ($\mathbf{I}_S^{back}$) to the FM. In a generalized form this back flow of spin current is denoted as $\mathbf{I}_S^{back} \sim \beta\left(g_r^{\uparrow\downarrow}\mathbf{I}_S^{pump}\right)$, where β is the back flow factor. Therefore the net spin current loss by the FM is $\mathbf{I}_S = \mathbf{I}_S^{pump} - \mathbf{I}_S^{back}$.

The quality of spin sink material is primarily determined by three factors, (1) the character of the electron (s, d, f) in its conduction band, (2) the electron number Z of the material, (3) the spin diffusion length of the material. It is found that lighter elements like Al, Cu, Cr and heavier elements like Ag, Au, are less effective spin sinks since they only have s electrons in their conduction band. However, heavier elements like Pt ($Z = 78$), Pd ($Z = 46$), which have d electrons in their conduction band, are quite efficient in terms of their spin flipping ability[22].

2.2.3 Additional damping by spin pumping for various magnetic heterostructures

The expression for additional damping with an ideal spin sink attached to the ferromagnet is given as $\triangle\alpha = \frac{\gamma\hbar g_r^{\uparrow\downarrow}}{4\pi M_S V}$. The spin mixing conductance term, when determined experimentally are normalized to the cross sectional area. We thus rewrite the additional

damping as:

$$\triangle\alpha = \frac{|\gamma|\,\hbar}{4\pi}\frac{1}{M_S}\left(\frac{g_{eff}^{\uparrow\downarrow}}{S}\right)\frac{1}{t_{FM}}. \tag{2.9}$$

The effective spin mixing conductance $g_{eff}^{\uparrow\downarrow}$ depends on all layers and interfaces the spin current traverses on it's path, and is a function of the layer configuration. We note two important properties of this additional damping caused due to spin pumping:

• The additional damping $\triangle\alpha$ should be Gilbert type damping, and

• The additional damping $\triangle\alpha$ has a linear dependance on the inverse of thickness of the ferromagnetic layer, i.e. $\triangle\alpha \propto 1/t_{FM}$.

The spin pumping damping parameter can alternatively be defined in terms of a Gilbert relaxation rate $G\,(=\gamma\alpha M_S)$. Following eqn. 83 of ref. [22], we can write: $\triangle G = \frac{|\gamma|^2\hbar}{4\pi}\left(\frac{g_{eff}^{\uparrow\downarrow}}{S}\right)\frac{1}{t_{FM}}$. Using $\gamma = \frac{g_L\mu_B}{\hbar}$, the expression for G can be rewritten as: $\triangle G{\cdot}t_{FM} = \left(\frac{g_L\mu_B}{\hbar}\right)^2\left(\frac{g_L\mu_B}{\hbar}\right)[\frac{1}{2}\left(\frac{G_0}{2}\right)\left(\frac{g_{eff}^{\uparrow\downarrow}}{S}\right)]$. The term G_0 is the fundamental quantum conductance defined as: $G_0 = \frac{2e^2}{h} = 7.748\times10^{-5}\Omega^{-1}$, and $\frac{G_0}{2}$ is the conductance per spin. In Ref [31] spin mixing conductances are given in terms of the conductance per spin, $\frac{G_{eff}}{S} = \frac{G_0}{2}\frac{g'_{eff}}{S}$ in units of $10^{15}\Omega^{-1}m^{-1}$.

2.2.4 Forms for effective mixing conductance

2.2.4.1 FM/NM heterostructures

As mentioned earlier for a ferromagnetic heterostructures the effective spin mixing conductance could be a parallel combination of conductances coming from all the interfaces and in some cases from the bulk part as well. In the simplest case of a FM/NM structure, assuming NM is an ideal spin sink, all the pumped out spin current from FM is absorbed in NM. For this structure the effective spin mixing conductance is just the characteristic spin mixing conductance of FM/NM interface seen as:

$$\frac{g_{eff}^{\uparrow\downarrow}}{S} = \frac{g_{FM/NM}^{\uparrow\downarrow}}{S}. \tag{2.10}$$

2.2.4.2 FM/NM1/NM2 trilayers

In this case, we consider ferromagnetic spin pumping into a bilayer $NM1/NM2$ normal-metal system. We assume that the spin current is driven through the first normal metal $NM1$, which offers quasi-ballistic transport to the spin current. The thickness of $NM1$ is smaller compared to it's spin flip diffusion length i.e., $t_{NM} \ll \lambda_{SD}$, and is a light element (small atomic number). From $NM1$, the spin accumulation can diffuse back into the ferromagnet, or it can traverse to reach the $NM2$. It is considered that $NM2$ is an

ideal spin sink, therefore spin current, which reaches $NM2$, is either relaxed immediately by spin-flip processes or is carried away before diffusing back into $NM1$. For such a case the effective spin mixing conductance parameter can be written as:

$$\left(\frac{g_{eff}^{\uparrow\downarrow}}{S}\right)^{-1} = \left(\frac{\tilde{g}_{FM/NM1}^{\uparrow\downarrow}}{S}\right)^{-1} + R_N + \left(\frac{\tilde{g}_{NM1/NM2}}{S}\right)^{-1}, \tag{2.11}$$

where, $R_N = \frac{2e^2}{h} t_{NM}\rho$ is the resistance (per spin, in units of h/e^2) of the $NM1$ layer, and $\tilde{g}_{NM1/NM2}$ is the effective spin conductance of the $NM1/NM2$ interface. We consider an example to look at the contribution from the bulk resistance of the $NM1$ layer. Considering a case of the Cu layer of $t_{NM} = 3nm$, which has typical resistivity at room temperature about $\rho = 20\,\Omega \cdot nm$, the contributed R_N is $\sim 1/215\,nm^{-2}$. This is much smaller compared to the other terms, indicating that Cu is a very good material for this purpose. As we are dealing with these microscopic electrical circuits, we need to realize that as spin current flows from ferromagnets to nonmagnet, or one nonmagnet to another one, the spin current faces different resistances compared to charge currents. In this regard, we have to consider a further resistance known as Sharvin resistance.

Sharvin resistance

Conventional circuit theory and Kirchhoff's laws were developed for macroscopic electrical circuits where the circuit components like resistances, inductances were distinguishable elements. For instance a single resistor could have been assumed to be two resistors with half resistance in series. In nanoscopic structures, devices where electrons propagate ballistically and/or when the wave character comes into play, conventional circuit theory considerations are often not valid. A thin ballistic wire can be taken for an example where the resistance does not depend on its length [24] and is purely geometrical. Most electrons in such a case are reflected from the lateral boundaries, which gives rise to Sharvin point contact resistance. As the constriction goes wider in dimension the Sharvin resistance becomes smaller and negligible in the bulk limit. However, in the intermediate case like ours, the total resistance under approximation is a summation of Ohmic and Sharvin resistance.

Therefore, the re-normalized conductances $\tilde{g}_{NM1/NM2}$ are related with the bare single spin resistance and the Sharvin resistance coming from both sides of the $NM1/NM2$ interface and can be viewed as (see eqn. 32 of [22]):

$$\frac{1}{\tilde{g}_{NM1/NM2}} = \frac{1}{g_{NM1/NM2}^{\sigma\sigma'}} - \frac{1}{2}\left(\frac{1}{g_{NM1}^{Sh}}\right).$$

The bare single spin resistance $\frac{1}{g_{NM1/NM2}^{\sigma\sigma'}}$, of the all-normal interface is corrected for the

$NM1/NM2$	$2AR\,(f\Omega\,m^2)$(exp)	$\tilde{g}/S$ (nm^{-2}) (exp)
Cu/Pt	1.5	17.2
Cu/Pd	0.9	28.7
Cu/Ru	2.2	11.7

Table 2.1: Conductances $g_{N1/N2}/S$ as calculated from experimental resistance-area products $2RA$ tabulated in Ref. [42]

drift effect by subtracting the Sharvin contribution from the $NM1$ side. Note that NM2 is considered as an ideal spin sink. Therefore the Sharvin conductance corrected form of the effective spin mixing conductance is seen as:

$$\left(\frac{g_{eff}^{\uparrow\downarrow}}{S}\right)^{-1} = \left(\frac{g_{FM/NM1}^{\uparrow\downarrow}}{S}\right)^{-1} - \frac{1}{2}\left(\frac{g_{NM1,Sh}^{\uparrow\downarrow}}{S}\right)^{-1} + \frac{2e^2}{h}t_{NM1}\rho + \left(\frac{\tilde{g}_{NM1/NM2}}{S}\right)^{-1}. \quad (2.12)$$

This form of the effective spin mixing conductance will be used for our data extraction in Chapter 4.

Interfacial resistance

The spin conductances $\frac{\tilde{g}}{S}$ for $NM1/NM2$ layers can be converted into an interfacial resistance RA in $f\Omega\,m^2$ by multiplying by the conductance quantum G_0 $(= \frac{2e^2}{h} = 7.748 \times 10^{-5}\Omega^{-1})$ as:

$$RA = \frac{1}{G/S} = \frac{1}{G_0}\left(\frac{\tilde{g}}{S}\right)^{-1}. \quad (2.13)$$

For example, considering $g/S = 10nm^{-2}$, we get

$$2RA = 2.582\,f\Omega\,m^2\left(\frac{10\,nm^2}{g/S}\right)$$

Tabulated values for interfacial resistances $2AR$ (as cited) have been given by Bass et al. [42]. We convert them into spin conductance as shown in Table 1.

In table 2 we convert the Sharvin conductance values given in units of nm^{-2} from Tserkovnyak et al. [22], into $(f\Omega\,m^2)^{-1}$.

2.2.4.3 FM1/NM/FM2 trilayers

For this type of heterostructures with two magnetic layers, the spin current traverses an intermediate NM layer to reach the second ferromagnet FM2. Assuming that $FM2$ randomizes the spins over the short spin coherence length λ_C, the effective spin mixing

NM Metal	$g^{Sh}/S\ (nm^{-2})$	$g^{Sh}/S\ (f\Omega\, m^2)^{-1}$
Cu	15.0	0.58
Ta	25.0	0.97
Pd	16.0	0.62
Pt	17.6	0.68

Table 2.2: Single-layer Sharvin conductances in nm^{-2} and Siemens/area, tabulated in [22] and [31], respectively. Values are related through e^2/h, the one-spin conductance/channel.

conductance for the whole structure can be written as:

$$\left(\frac{g_{eff}^{\uparrow\downarrow}}{S}\right)^{-1} = \left(\frac{\tilde{g}_{FM1/NM}^{\uparrow\downarrow}}{S}\right)^{-1} + \frac{2e^2}{h}t_{NM}\rho + \left(\frac{\tilde{g}_{FM2/NM}^{\uparrow\downarrow}}{S}\right)^{-1}. \tag{2.14}$$

The $\tilde{g}$ refer to re-normalized spin mixing conductances, which is taken from Tserkovnyak's work (eqn. 33 of [22]), and could be written as:

$$\frac{1}{\tilde{g}_{FM/NM}^{\sigma\sigma'}} = \frac{1}{g_{FM/NM}^{\sigma\sigma'}} - \frac{1}{2}\left(\frac{1}{g_{NM}^{Sh}} + \delta_{\sigma\sigma'}\frac{1}{g_{FM}^{Sh}}\right),$$

where $g_{FM/NM}^{\sigma\sigma'}$ is the bare spin mixing conductance for the FM/NM interface and, g_{NM}^{Sh}, g_{FM}^{Sh} are the Sharvin conductances of the NM and FM layer, respectively. As the ferromagnets are considered as ideal spin baths for the spin currents the δ term is zero, leaving,

$$\frac{1}{\tilde{g}_{FM/NM}^{\uparrow\downarrow}} = \frac{1}{g_{FM/NM}^{\uparrow\downarrow}} - \frac{1}{2}\frac{1}{g_{NM}^{Sh}}. \tag{2.15}$$

Considering a special case when $FM1 = FM2$, we obtain:

$$\left(\frac{g_{eff}^{\uparrow\downarrow}}{S}\right)^{-1} = 2\left(\frac{g_{FM/NM}^{\uparrow\downarrow}}{S}\right)^{-1} - \left(\frac{g_{NM}^{Sh}}{S}\right)^{-1} + \frac{2e^2}{h}t_{NM}\rho \tag{2.16}$$

2.3 Literature Review:

In the introductory section the dynamic coupling between a precessing magnetic layer and itinerant electrons in a FM/NM system was independently interpreted by Berger in 1996 [14] and Tserkovnyak et al. in 2002 [21]. Berger's interpretation of the enhanced Gilbert damping of the FM layer in FM/NM system was based on an elementary quantum process of magnon annihilation which is associated with spin flip. This idea was verified by Urban et al. via the study of enhanced Gilbert damping in

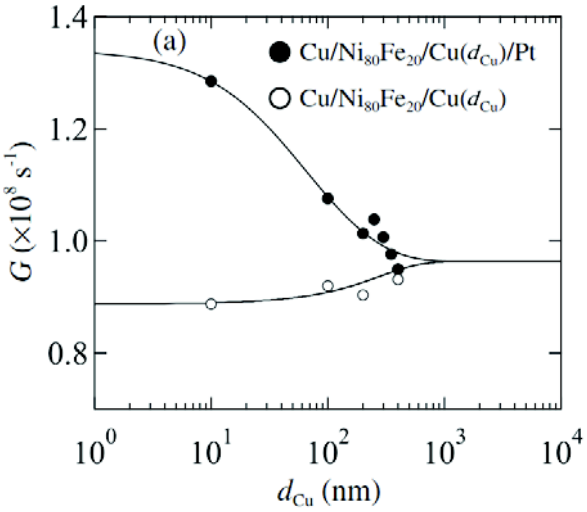

Figure 2.6: Damping parameter α of $NiFe$ as a function of Cu spacer thickness, with, and without Pt overlayer, as observed by Mizukami et al. [46].

magnetic double layer structures $FM1/NM/FM2$ [43]. In order to quantify properly the additional damping due to dynamic coupling, FMR linewidths for the heterostructures $GaAs/Fe(16)/Au(40)/Fe(40)/Au(20)$ and $GaAs/Fe(16)/Au(20)$ was measured. All thicknesses are presented in terms of monolayers (ML). Note that in the first structure it was made sure by introducing the Au(40ML) layer that there is no RKKY coupling between $Fe(16)$ and $Fe(40)$ and the second structure is a reference to the first one which gives the damping without the dynamic coupling effect. Their observation shows that for the double magnetic layered sample the measured damping for $Fe(16)$ is much higher compared to the reference structure. The explanations were sought based on the quantum mechanical picture of magnon creation and annihilation. It was thought that due to the uniform precession of $Fe(16)$, a magnon is annihilated and its energy $\hbar\omega_q$ is transferred to a conduction electron, which traverses the Au spacer and reaches the $Fe(40)$ layer. The magnon is transferred from the conduction electrons to $Fe(40)$ layer and this effectively causes an additional damping to the precessing $Fe(16)$ layer.

Tserkovnyak et al. took a different approach to interpret the dynamic coupling. This approach was based on the formalism of parametric pumping by Büttiker et al. [40], which was later on developed by Brouwer [44], in the context of mesoscopic scattering problems. In a more recent work, a linear response formalism has been put forward by Šimánek and Heinrich [45].

Other well known experimental studies in this domain, were performed by the group of Mizukami, who has done some pioneering experiments (see Figure 2.6). They have performed FMR measurements to extract the linewidth of the Permalloy ($NiFe$) layer

sandwiched between two nonmagnetic layers, where the nonmagnets were Pt, Pd, Ta, Cu [46, 37, 38]. It was shown that nonmagnets like Pt, Pd, which has stronger spin orbit coupling, caused much broader linewidth compared to Ta, Cu. However, the reason of damping enhancement was not precisely understood by this group, and at that time the theoretical development of spin pumping was not established yet. The explanations for this damping enhancement as sought by Mizukami et al. was based on the increase of the Lande g-factor g_L with decreasing $NiFe$ thickness, since the intrinsic damping α, caused due to spin orbit is proportional to $(g_L - 2)^2$. There are few other groups who have also observed this enhanced damping [47, 48] in magnetic heterostructures but none of these effects were analyzed clearly based on spin pumping models proposed by Tserkovnyak.

Even though these alternative models to describe the additional damping are quite familiar to the magnetism community and might be easier to understand conceptually, for a quantitative comparison we find Therkovnyak's model of spin pumping is more suited. Therefore we will present our experimental study, mainly based on the spin pumping model proposed by Tserkovnyak et al. Our experiments concerns mainly two types of studies, (1) we verify the spin pumping model for different ferromagnets and nonmagnets, and (2) we use spin pumping as a method of generation (precessing ferromagnet) and injection of pure spin current. These two types of studies will be presented in Chapter 4 and Chapter 5. The central parameter of our interest is the enhanced Gilbert damping, from which we will extract the spin mixing conductance(FM/NM) and spin conductance (NM1/NM2) parameters for different interfaces. An advantage of these type of measurement is that it doesn't require device nano-fabrication, they are rapid compared with STT device measurements for a given film configuration, allowing a larger number of layers to be characterized in finite time. Finite-size magnetostatic [49] and activation volume [50] effects do not enter in the measurement, hence interpretation becomes easier.

Chapter 3

Experimental methods

In this chapter we present the experimental method that we employ for the growth and characterization of our samples (magnetic heterostructures). In the first part we talk about the film growth technique in ultra-high vacuum (UHV) system using magnetron sputtering deposition technique. In the second and third part we discuss about the magnetic property characterization. This thesis work is primarily focused on the study of the magnetization dynamics. Ferromagnetic resonance measurements are carried out in the field range of 0-0.5T and in the frequency range of 0-24 GHz for the characterization of the dynamics properties. The resonance linewidth is related to the dynamic susceptibility of the magnetic material, which we will discuss in section 2 of this chapter. The operational principle and the component details of our inductive FMR spectrometer, which is capable of characterizing thin (as low as 2.5 nm) films will be discussed. In section 3 of this chapter we will introduce the X-ray magnetic circular dichroism (XMCD) technique. This spectroscopic technique is employed in order to observe induced magnetism in nonmagnetic metals by direct exchange coupling and indirect exchange coupling with a ferromagnet. XMCD is used to support our FMR characterization results.

3.1 Sample preparation: Magnetron sputtering deposition

Our thin films were prepared by magnetron sputtering deposition, using an Actemium sputter deposition machine. This technique is widely used for the production of thin films on the order of few nm to microns. This offers certain advantages over other deposition methods like Molecular beam epitaxy (MBE), Pulsed laser deposition (PLD), Chemical vapor deposition (CVD). Notably it allows the deposition of a wide range of materials such as metals, alloys and dielectrics in a relatively short time scale with a fairly good precession in controlling the thickness and maintaining homogeneity over

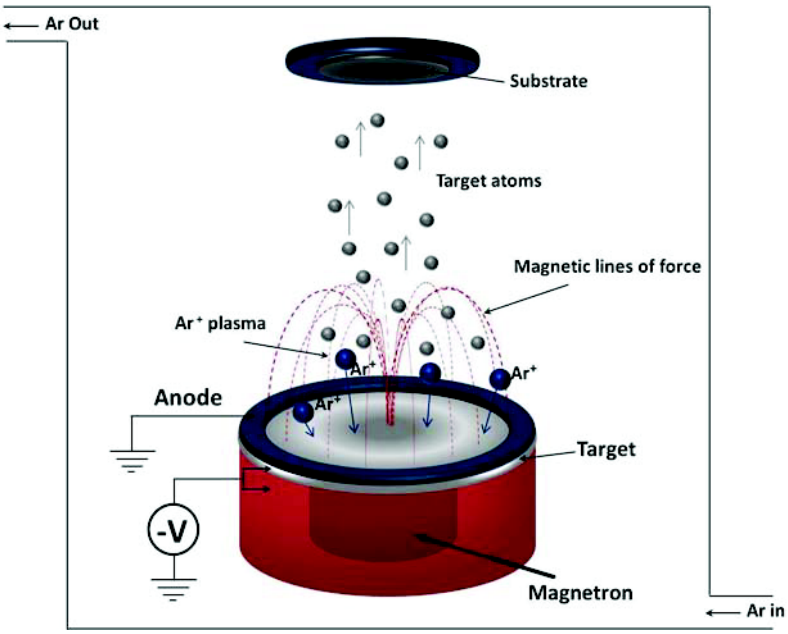

Figure 3.1: Schematic diagram of Magnetron Sputtering deposition system. Energetic ions sputters materials from the target which diffuse through the plasma towards the substrate where it is deposited.

large enough substrates. Sputtering deposition takes place in an ultra high vacuum chamber where both the target (material which is to be deposited) and substrate (on which the material is deposited) is placed. A vacuum level of 10^{-7} to 10^{-9} mbar is necessary to have good deposition, which is reached by using cryogenic pumps and water pumps. An inert gas Argon (which is the most commonly used), which possesses high sputter yield (ionized/sputter atoms) for most metals, is introduced in the deposition chamber (see Figure 3.1). The other reason for using Ar is that it is in-toxic and less expensive compared to other inert gases. To create a plasma in between the cathode (target) and the anode an electrical discharge is created by applying negative voltage to the cathode (target), with respect to the anode and the shielding. The Argon atoms are ionized by means of collision with the electrons as an effect of this electrical discharge. A magnetron is installed inside the cathode, which allows the plasmas (Ar^+ ions, electrons) to concentrate near the surface of the target. Positive atoms (Ar^+) traverse towards the target and collide with it (known as bombardment) to eject materials from the target. This ejected material which carries a huge kinetic energy reaches the substrate gets deposited on it (see Figure 3.1).

The quality of sputter films depends on several parameters such as the vacuum level, deposition rate, substrate temperature, surface energy of the substrate and the nature of the material which is to be deposited. Reaching a certain vacuum level and maintaining it

throughout deposition is very important in obtaining good film quality. If the vacuum is too low the sputtered atoms undergo collisions with plasma species and cannot condense on the substrate. Whereas, if the vacuum level is very high, the number of collisions between ions and the target is insufficient to have material ejection from the target. In between these two limits the deposition rate is maximum. The sputtering rate depends on the DC voltage and can modify micro-structural properties of the material. Using a high sputtering rate one can obtain polycrystalline growth. The thickness of the deposited layer is determined by the exposure time of the substrate above the plasma. A cache located between the target and the substrate can control this time of exposure.

Thickness calibration:

The thickness calibration was done by depositing $40nm$ to $80nm$ of the material on a Si/SiO_2 native oxide substrate. The thickness is obtained by the reflectivity measurement using grazing X-ray. With this soft resonance X-ray scattering Kiessing fringes are obtained, which enables the estimation of the sample thickness with very good precession (tolerance level is about $0.5nm$)

Deposition parameters for our samples:

All of our samples were deposited using the above mentioned Actemium DC magnetron sputtering Machine. Si/SiO_2 native oxide substrates have been used for all our samples. The base pressure was $2 \times 10^{-7} Torr$, whereas the working pressure was $1.5mTorr$ of Argon (Ar) gas. The deposition rate was $\sim 0.24nm/s$ for Cu and $\sim 0.1nm/s$ for the other layers. Most of our samples were seeded with $Ta(5nm)/Cu(5nm)$ bilayers, capped with $2\,nm$ or $3\,nm$ of Aluminum (Al) layers, which then naturally oxidized in air. In Table 2. 1 we present all our deposited heterostructures (seed and cap layers are not shown). In column 1, we refer to the chapters where the dynamics characterization of the corresponding samples are presented, by mentioning the type of study in column 2. In column 3 the central part of the heterostructures is given. Note that the reference layers presented in column 4, are very important for the kind of study that we are doing. We needed these layers in order to quantify pure spin pumping effect accurately.

3.2 Transmission electron Microscopy:

Bright field (BF) and dark field transmission electron microscopy has been carried out by using FEI Titan operating at $300\,kV$. This images ware taken by Eric Gautier. Cross sectional specimen are prepared by first bonding the surface with permanent glue followed by mechanical thinning and ion miling (using 1 KeV Ar ions) for final electron transparency. These experiments were carried out in a scanning transmission electron microscope (STEM) mode and the high angle annular dark field (HAADF) and BF image. Cross sectional TEM images near the substrate-film interface show the presence

Chapter: Set	Study	Heterostructures	Reference
Chapter 4: I	Spin pumping using Pt spin sink, indirect contact with FM	Py(t)/Cu 3/Pt 3	Py(t)/Cu 3
		CoFeB(t)/Cu 3/Pt 3	CoFeB(t)/Cu 3
		Co(t)/Cu 3/Pt 3	Co(t)/Cu 3
Chapter 4:II	Pt in direct contact with FM	Py(t)/Pt 4	Py(t)/Cu 3
Chapter 4: III	Verification of spin pumping with *FM* overlayers	Py(t)/Cu 5/CoFeB	Py(t)/Cu 3
		Py(t)/Cu 3/Co	Py(t)/Cu 3
		CoFeB(t)/Cu 3/Co	CoFeB(t)/Cu 3
Chapter 5: I	Penetration depth of spin current in FMs & AFM	Py 10/Cu 5/Co(t)	Py 10/Cu 5
		Py 10/Cu 3/MnIr(t)	”
		Co 8/Cu 5/CoFeB(t)	”
		Co 8/Cu 5/NiFe(t)	”
Chapter 5: II	Penetration depth of spin current in NM's	Py 10/Cu 5/Pt(t)	Py 10/Cu 3
		Py 10/Cu 5/Pd(t)	”
		Py 10/Cu 5/Ru(t)	”
Chapter 5: III	NM's in indirect contact with FM	Py 10/Pt(t)	Py 10/Cu 3
		Py 10/Pd(t)	”
Chapter 5: IV	Quantifying interface resistance	NiFe 8/ [Cu(6/n)/Al(6/n)]n	NiFe 8/ AlO
		NiFe 8/ [Cu(6/n)/Al(6/n)]n/ Pt 3	
		NiFe 8/ Cu 12/ Pt 3	
		NiFe 8/ Al 12/ Pt 3	
Chapter 5: V	Quantifying spin current reflection	Py 10/Cu 3/Pt(t)/Co8	Py 10/Cu 3
		Py 10/Cu 3/Pd(t)/Co8	”
		Py 10/Cu 3/Ru(t)/Co8	”
Chapter 6:I	XMCD measurement	Py5/ Cu 3/ Pd 2.5/ Cu 3	
		Py 5/ Pd 2.5	
		Py 5/ Cu 3/ Pt 1/ Cu 3	
		Py 5/ Pt 1	

Table 3.1: List of heterostructures grown using our Actemium DC magnetron sputtering Machine on Si/SiO_2 native oxide substrate.

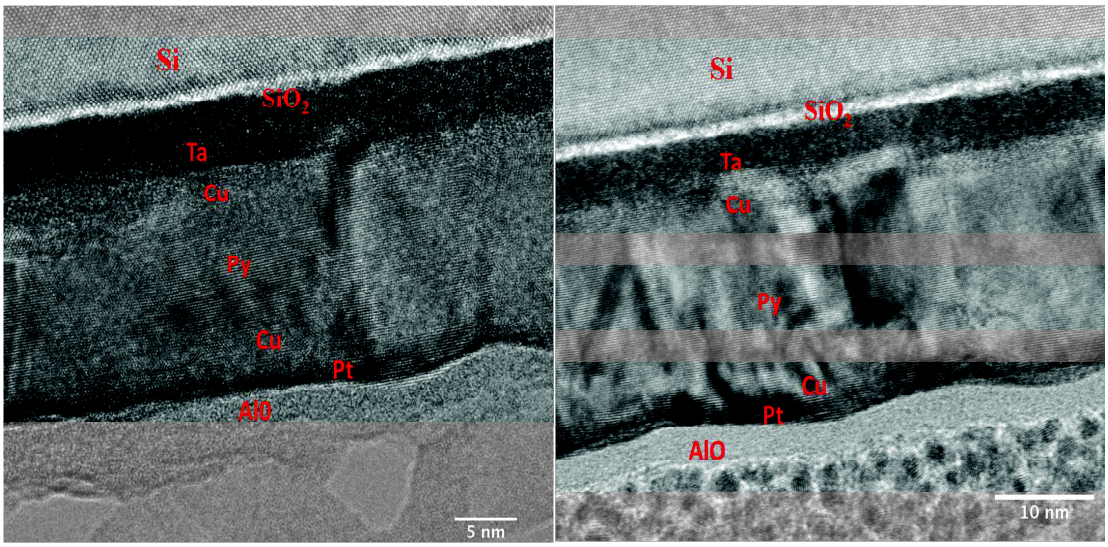

Figure 3.2: Bright-field cross-sectional TEM images for (a) $seed/Ni_{81}Fe_{19}(10nm)/Cu(3nm)/Pt(0.5nm)/AlO(3nm)$ and (b) $seed/Ni_{81}Fe_{19}(10nm)/Cu(3nm)/Pt(1.2nm)/AlO(3nm)$.

of amorphous oxide at the interface.

In Figure 3.2, we present bright-field cross-sectional TEM images for (a) $seed/Ni_{81}Fe_{19}(10nm)/C$ and (b) $seed/Ni_{81}Fe_{19}(10nm)/Cu(3nm)/Pt(1.2nm)/AlO(3nm)$ heterostructures. We see that the growth is quite good. Some roughnesses is observed at the top of the heterostructures. We find, even the $0.5nm$ of Pt layer is seemed to be have a continuous coverage. It is hard to distinguish $Cu/NiFe$, as they have very similar atomic number.

3.3 Ferromagnetic resonance (FMR) measurement (inductive technique)

Ferromagnetic resonance is a very well known technique and has been extensively employed for the study of magnetization dynamics since many decades. Fig 2.2. shows a schematic illustration of this technique, that we use. We consider a magnetic thin film where the magnetic moments are confined in the film plane by the act of demagnetizing field. A DC bias field (H_B) is applied along the film plane, which aligns the magnetization of the film M along H_B. If M is now subjected to a perturbation, it will experience a torque that results in a gyroscopic motion of M around H_B. The presence of damping will make it relax and it will be finally restored along the bias field again. This fundamental phenomenon i.e gyroscopic motion and relaxation of magnetization is the basis of ferromagnetic resonance. The perturbation of the magnetic moment is created by a high

frequency (GHz) electromagnetic (microwave) field h^{rf}, which is applied perpendicular to the bias field H_B, in order to have a continuous torque to the magnetization M. This microwave field h^{rf} drives the magnetization into precession around H_B. Corresponding to a particular value of H_B, the resonance of this precessional motion occurs at a specific frequency of h^{rf}, or vice verse. This resonance phenomenon is known as ferromagnetic resonance.

At resonance, the absorption of the microwave field by the magnetization is maximum. The absorption characteristics has a Lorentzian lineshapes and the line width contains information about the relaxation of the magnetization. The line position i.e. the resonance position contains information about the saturation magnetization, surface anisotropy etc. Note, that in our case considering an in plane bias field geometry is more suitable, which makes the characterization of certain parameters, of our interest, much easier. The field-frequency relation for the ferromagnetic resonance absorption is known as the Kittel relation which was discussed in Chapter 1. Note, that FMR measurements can be performed in two ways: (1) by keeping the bias field H_B constant and sweeping the frequency of the microwave h^{rf} and (2) by keeping the frequency of the microwave h^{rf} constant and sweeping bias field H_B . Our FMR spectrometer is capable of working in a broadband frequency range of 0-24 GHz and a field range of 0-0.8T. Since we use a co-planner waveguide along with several microwave components to transmit the microwave signal, using frequency swept method might be less sensitive as the circuit can have slightly different responses at different frequencies. However, since all of these circuit components were nonmagnetic; fixed frequency field swept FMR seemed a preferable choice for us. Therefore, all of our magnetization dynamics characterizations were done using a typical field swept fixed frequency FMR at different frequencies in the broadband range of $2 - 24GHz$.

FMR Spectrometer

Fig 1 shows the schematics of our *inductive* FMR spectrometer. A Rohde & Schwarz zva24 vector network analyzer is used as a source for the microwave signal h^{rf}; capable of producing the signal in the frequency range $10\,Mhz - 24\,GHz$. This microwave signal is transmitted through a double ground plane coplanar waveguide (CPW), which is 50Ω impedance matched. The details about this CPW, which is placed in between the magnetic poles (gap of $20\,mm$), is discussed later. The sample is placed on top (up side down) of the CPW. The microwave input power was kept at $15dBm$ to ensure a linear response. The static magnetic field was applied in the plane of the film, perpendicular to the microwave field, as shown in Figure 3.3 and 3.4(a). The transmitted signal, as received, is passed through a Schottky diode detector which converts the electromagnetic

field into voltage. To enhance the signal to noise ratio, phase sensitive lock-in detection is employed (this will be discussed more details in a later part of this section). The processed signal as received from the lock-in amplifier is a derivative of the absorbed power (in principle Lorentzian) versus field profile. We put the sample on the CPW where the field is homogeneous. The derivative of the absorption signal (Lorentzian) is plotted after the dispersion correction. From this plot the resonant field corresponding to the fixed frequency and the linewidth is extracted.

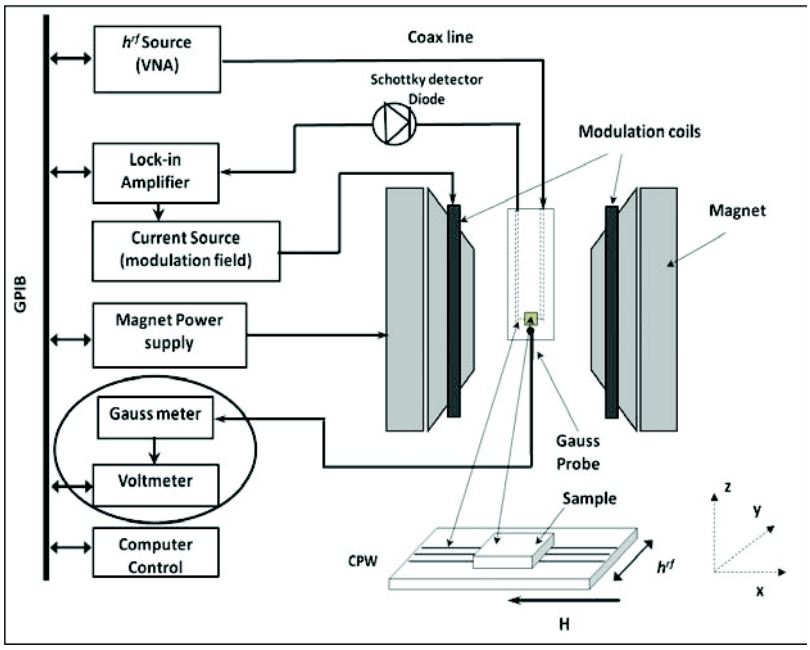

Figure 3.3: Schematic diagram of the FMR spectrometer. Microwave radiation is transmitted through a CPW, located between the pole pieces of the electromagnet. Transmitted power is converted into voltage using a Schottky diode and used as the Lock-in Amplifier input.

CPW design and Field direction

The coplanar waveguide (CPW) used by us consists of a central strip conductor of width $w = 375\,\mu m$ surrounded by two co-planer ground planes in each side. The gap between the central line and the ground planes is $140\,\mu m$. The substrate used here is Rogers-RO4350 high frequency circuit material. The thickness of the substrate is $10 mil$ or $0.254 mm$ and the dielectric constant is 3.66. Cr/Au is used as the metallic conductor deposited on the substrate for microwave propagation. Our CPW is specially designed so that the bottom part of the substrate is also Gold plated and grounded as shown in

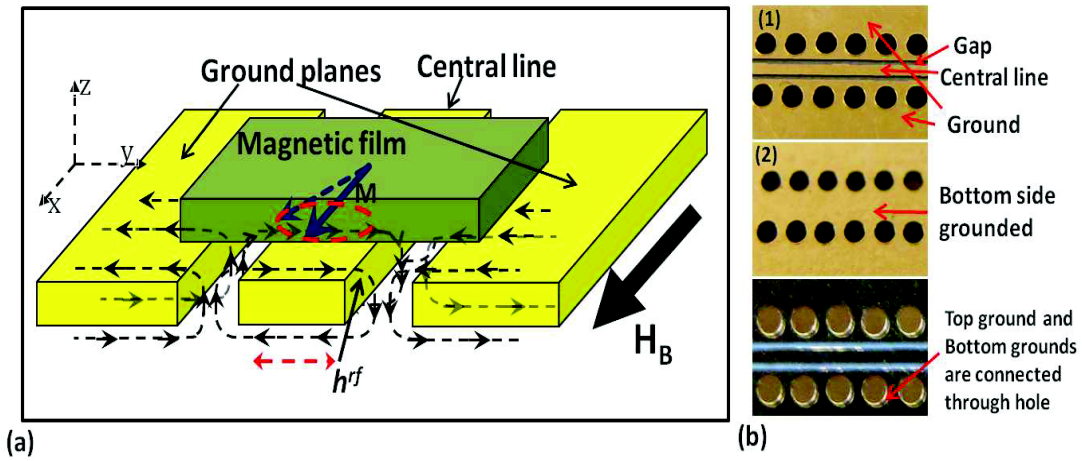

Figure 3.4: Cross sectional diagram of a coplanar waveguide (CPW) showing the rf filed (h^{rf}) configuration. h^{rf} is considered approximately parallel to the plane of the CPW, except in the middle of the gap. The magnetic sample is placed on top of it.

Figure 3.4(b). The ground planes on the two sides of the substrate are connected via several holes (shown in Figure 3.4(b). It is slightly easier to fabricate a CPW compared to other transmission lines, like the microstrip lines which consist of metallic layers in planner form, requiring more processing steps for the development. Our CPW is capable of working at the frequency range of $0 - 50GHz$, but above this, the wave propagation mode becomes non-TEM[51].

Figure 3.4(b) shows a schematic (holes connecting grounds of both sides of the substrate are not shown) of the CPW and the magnetic field lines for it. The magnetic field lines which are of primary interest, turn around the central conductor as it does in the case of a coaxial line. But since the central conductor has a rectangular shape, where it's width is much greater compared to it's thickness, the magnetic field lines, just on top of the conductor, are parallel to the surface. In the gaps the magnetic field turns out of plane. However this contribution is neglected as the parallel contribution dominates over this perpendicular contribution.

Lock-in Modulation technique: Field modulation, Frequency modulation

In FMR, the power absorbed by the magnetic sample can be directly measured in order to extract parameters from the linewidth. However, measuring the power directly is not always useful as sometimes the signal to noise ratio can be poor. One way of improving the signal to noise factor is by employing the method of modulation (applied field or frequency) and using a Lock-in amplifier to perform a phase sensitive detection of the signal. Two coils in Helmholtz configuration have been used to modulate the DC

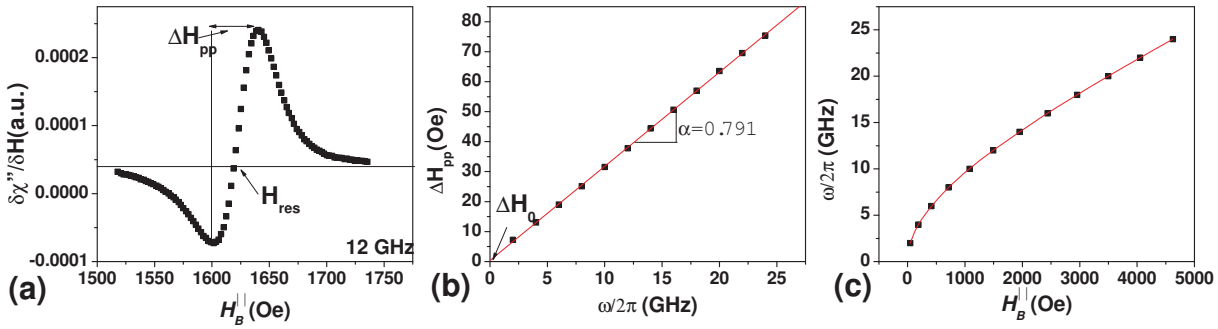

Figure 3.5: (a) Sample Lineshape obtained by our FMR spectrometer. (b) peak-to-peak linewidth $\triangle H_{pp}$ obtained at different microwave frequencies are plotted. Damping parameter α obtained from the slope of the plot. (c) Resonance fields H_{res} are plotted as a function of applied microwave frequencyω (Kittel plot).

field with amplitudes varying from $2Oe$ - $20Oe$ at a constant frequency of 201Hz. This field is controlled by the Lock-in amplifier which sends an a.c. voltage to the Kepco power amplifier which runs the modulation coils. The transmitted high frequency signal is converted into voltage by a Schottky diode and given to the input of the Lock-in amplifier. In this method, we are in fact measuring the slope of the absorbed power with respect to DC magnetic field H_B. This bias field H_B is then swept to obtain different slopes as a function of H_B (see Figure 3.5(a)). This measurement is referred to as fixed frequency (microwave) swept field FMR.

Lineshape characterization

It was discussed in Chapter 1 that the imaginary part of the susceptibility is responsible for the absorption of the microwave energy in the magnetic system (see eqn. 1.20 of Chapter 1). As the imaginary part of the susceptibility is a Lorentzian, absorbed power in principle is also a Lorentzian. However, as we are using Lock-in phase sensitive detection, our spectra is a derivative of Lorentzian. Therefore we extract the peak-to-peak linediwth $\triangle H_{pp}$, from this derivative curve, which is related to the original Lorentzian linewidth $\triangle H$ as: $\triangle H = \frac{\sqrt{3}\triangle H_{pp}}{2}$. As our spectrometer is capable to do the measurement in a broad field and frequency range, we extract the field linewidths at different frequencies. In Figure 3.5(b) ΔH_{pp} is plotted as a function of microwave frequency ω. The damping parameter α is extracted from the slope of a linear fit ($\triangle H$ vs. ω). Note that there are several mechanisms which can cause relaxation in a ferromagnetic sample (see the last section of Chapter 1). The Gilbert type relaxation (in LLG) is linear. It is noted that sample inhomogeneity can also contribute to damping, it needs to be separated from the Gilbert damping, which was possible by using the well-known relation: $\Delta H_{pp}(\omega) = \Delta H_0 + \left(2/\sqrt{3}\right)\alpha\omega/|\gamma|$[7]. The advantage of performing FMR measurement in a broadband frequency range over a single frequency measurement is that the error

in α can be minimized since it is averaged over many frequency points and also the inhomogeneous contributions in linewidth can be separated.

3.4 X-ray magnetic circular dichroism (XMCD)

X-ray resonant absorption can be described in a simplified manner by considering a core electron, after absorbing photon energy, excited into an unoccupied electronic state. Since the magnetic properties of transition metals ($Fe: 4s^2 3d^6$, $Co: 4s^2 3d^7$, $Ni: 4s^2 3d^8$) are usually governed by their d electrons, we are therefore more interested in X-ray resonant absorption involving d electrons. For these materials we consider the X-ray absorption for the $L-edge$, where the *electron* from the "*initial*" spin-orbit split $2p_{3/2}$ and $2p_{1/2}$ levels are excited to the "*final*" valance d states ($3d$ or $4d$) after absorbing photon energy. However, this one electron transition picture is sometimes misleading since it depicts the spin–orbit splitting of the p core shell as an "initial state" effect. Also, it is found that, the the spin orbit coupling constant ζ for the core $2p$ shell is considerably larger (of order 15 eV) compared to that of valence $3d$ shell ζ (of the order of 50 meV). Meaning that $2p$ shell is more compact and also the $2p$ "*splitting*" dominates over the splitting of d states. Therefore for the proper description of the X-ray absorption process, it is more convenient to consider a *hole* transmission from "*initial*" d state to "*final*" $2p$ state. The X-ray absorption can be calculated using the time dependent perturbation of the sample by an electromagnetic field, which induces transitions between an initial state $|\psi_i\rangle$ to the final state$|\psi_f\rangle$. The transition probability, by considering an interaction or perturbation Hamiltonian H^{int} as given according to the Fermi golden rule:

$$W_{fi} = \frac{2\pi}{\hbar} \left| \langle \psi_f | H^{int} | \psi_i \rangle \right|^2 \delta_{E_f - E_i - \hbar\omega}$$

X-ray magnetic circular dichroism (XMCD) measures the dependence of X-ray Absorption on the helicity of the x-ray beam by a magnetic material. This type of X-ray absorption process is spin dependent and the intensity sum rule for the *number* of holes is applicable here. Therefore it is possible to measure an intensity difference corresponding to the number of spin-up or spin-down holes, which is the basics of XMCD spectroscopy. With this method X-ray absorption spectra are obtained in a magnetic field; one with left circularly polarized light and another with right circularly polarized light. The difference spectrum is measured, which can provide information about spin and/or orbital magnetic moment of the atom. In order to obtain maximum XMCD effect it is necessary to have the angular momentum of the photon L_{ph} collinear with the magnetization M of the sample. The dichroism effect is measured as the difference in the intensity of $p \rightarrow d$ transition (X-ray absorption), measured for photons with positive angular momentum

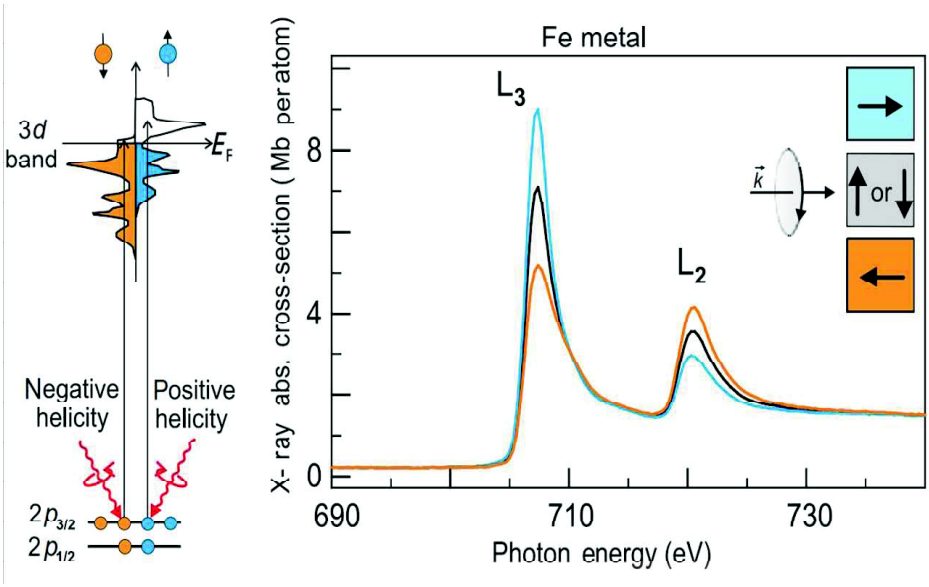

Figure 3.6: Schematic of X-ray magnetic circular dichroism (XMCD) effect for L-edge, with LCP and RCP X-rays. This figure was taken from ref. [52].

($q = +1$, L_{ph} points in direction of wave vector k) and negative angular momentum ($q = -1$, L_{ph} points in direction of wave vector $-k$) aligned along the fixed magnetization direction M of the sample. Equivalently, by switching the magnetization direction while the X-ray photon spin direction (polarization or helicity) is fixed, this effect can be observed. To understand this phenomenon for transition metals we consider a two step model.

This model was proposed by Stöhr and Wu in order to understand XMCD at the L-edges of $3d$ transition metals. In the first step, the circularly polarized X-ray interacts with the electrons in the p (core) shell and excites spin-polarized electrons (see Figure 3.6). This core p shell is viewed as a localized "source" of spin-polarized electrons. The spin-polarization of the excited electron depends on the L-edge ($2p_{3/2} \rightarrow L_3$ and $2p_{1/2} \rightarrow L_2$) and on the helicity of the X-ray. At the L_3 edge (lower energy), the LCP X-ray beam excites 62.5% of spin up electrons and 37.5% spin down electrons, while the RCP X-ray does the opposite. Whereas at the L_3 edge (higher energy), the LCP X-ray excites 25% of spin up electrons and 75% spin down electrons, while the RCP light does the opposite. For a nonmagnetic material the total transition intensity, i.e. spin up plus spin down intensity are same for LCP and RCP light. But, for ferromagnetic, paramagnetic or nonmagnetic materials, where there is an imbalance in the number of available empty spin up and spin down states, the absorption of the two polarizations becomes different. This difference is opposite at the $L_{3,2}$-edges. In the second step,

the spin-polarized electrons are analyzed by a spin-resolving detector consisting of the exchange split d final state. Note that, in order to have a complete description of X-ray dichroism in the one-electron model, one need to include spin-orbit coupling in the d-band.

Sum rules of XMCD

The intensity sum rules has been developed by Thole et al.[53] at the beginning of the 1990's. We note that the total number of empty d states above the Fermi energy E_F, which is nothing but the number of valence holes represented by N_h, is simply the number of spin up plus down states. Considering one electron model the core p state is spin orbit spitted into $2p_{3/2}$ and $2p_{1/2}$ states, which gives rise to L_3 and L_2 edge spectra, respectively. The intensity sum rule states that the transition intensity is proportional to the total number of empty d states N_h, when we sum over the $2p_{3/2}$ and $2p_{1/2}$ contributions. Intuitively this is seem to be correct as the intensity should increase if more empty final stated are made available for the transition. Applying the sum rule, the ground state expectation values of the spin magnetic moments $\langle S_z \rangle$, and orbital magnetic moments $\langle L_z \rangle$ can be obtained. The sum rules have been in the origin of a strong development of XMCD, which has now become a very strong technique for studying magnetic properties in thin magnetic films.

Chapter 4

Spin pumping in magnetic heterostructures

This chapter of the thesis concerns the verification of the spin pumping phenomenon in a broader range of ferromagnetic materials using various spin sink layer metals. We will demonstrate that spin pumping is a general phenomenon and that it is not restricted to certain materials. In section 1, we will describe the basis of our characterization method. In section 2 of this chapter we will present the results for spin pumping in magnetic heterostructures of the form $FM/Cu/Pt$, using three structurally distinct ferromagnets $\{FM = Ni_{81}Fe_{19}$ ("Py"), $Co_{60}Fe_{20}B_{20}$ ("$CoFeB$"), pure $Co\}$ and Pt as the spin sink layer. In section 3 of this chapter we study the additional damping caused due to ferromagnetic overlayers in $FM1/Cu/FM2$ heterostructures, using different ferromagnet combinations. In section 4 we will discuss the spin pumping for the case when paramagnetic spin sink Pt is deposited directly on top of the Py. For all these measurements the central parameter of our interest is the additional damping and from that we will extract the interfacial spin mixing conductance ($g^{\uparrow\downarrow}$) and the spin conductance (g) parameters. Our results will be compared to theoretically and experimentally published ones.

4.1 Ferromagnetic resonance measurement and extraction of parameters

The FMR spectrum contains a line position and a line-width, both of which, in our case, are determined in terms of field (Oe). In Figure 4.1, a typical FMR spectrum as obtained by our spectrometer, at microwave frequency of 12 GHz, is shown. Since we perform phase sensitive lock in detection, our spectrum is a Lorentzian derivative. The black squares represent the line shape for 6 nm of NiFe and the red dots represent the lineshapes of 6 nm of CoFeB. Both of these ferromagnetic layers were embedded in dif-

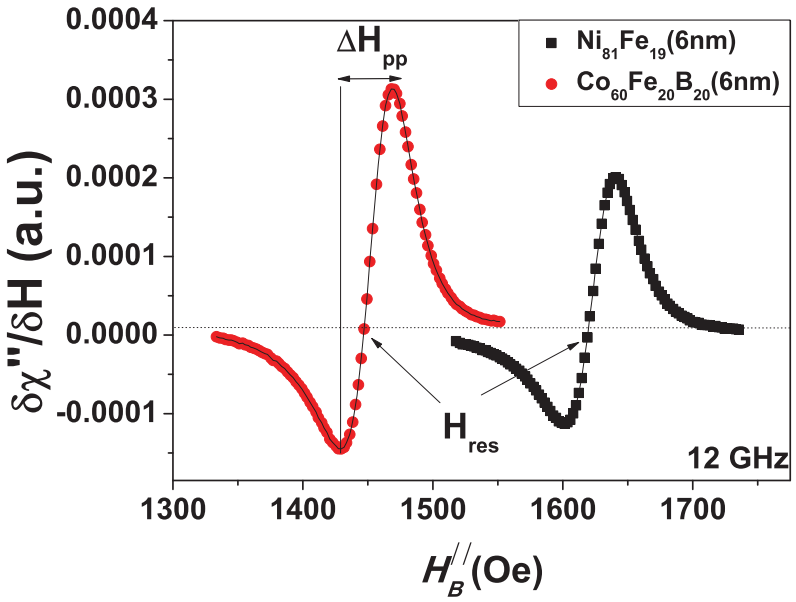

Figure 4.1: lineshapes and fits for films with (filled circles) and without (open squares) Pt overlayers, FM=$Ni_{81}Fe_{19}$ (red, right), CoFeB (blue left)

ferent magnetic heterostructures with seed and cap layers. We observe some asymmetry. We suppose that this asymmetry arises from the coupling between the magnetic layer and the CPW, which can partly mix the real and the imaginary part of the susceptibility. A phase factor is therefore considered, while extracting the peak to peak linewidth, to take care of this phase mixing, as shown in APPENDIX I. We fit these lines to extract the peak-to peak linewidth $\triangle H_{pp}$ and the resonance field H_{res} corresponding to a particular frequency of h^{rf}. Below we discuss the static and dynamic information (parameter) that can be extracted using the line position and the line width. We separate the parameter characterization into two parts, (1) **Characterization using line position:** This will include the extraction of the effective saturation magnetization M_s and surface anisotropy energy K_s, effective in-plane anisotropy H_K and (2) **Characterization using linewidth:** To extract the Gilbert damping parameter (relaxation) of the magnetization. In this first section, the data that we present are for magnetic heterostructures without any spin sink layers, but seeded with bilayer $Ta\,(5nm)/Cu\,(5nm)$ and capped with AlO. Information about the samples can be found in the fourth column of Table 3.1 (reference layers for Chapter 4: I).

4.1.1 Characterization using line position:

Kittel relation: The resonant fields H_{res}, as extracted from the FMR spectra, are plotted as a function of microwave frequency and fitted by the Kittel relation (as shown

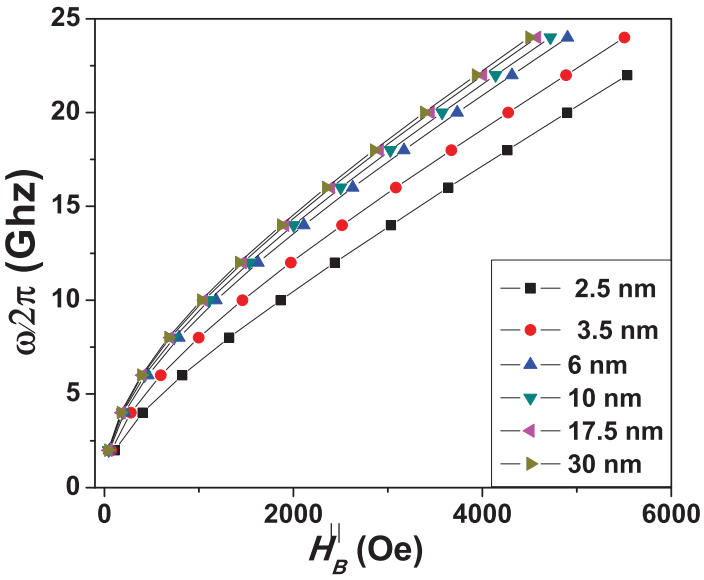

Figure 4.2: Fields for resonance $\omega(H_B)$ for in-plane FMR, $FM = Ni_{81}Fe_{19}$, $2.5nm \leq t_{FM} \leq 30.0nm$; solid lines are Kittel fits.

in Figure 4.2, see eqn 1.17):

$$\omega(H_B) = |\gamma|\sqrt{\left(H_B^{\|} + H_K\right)\left(4\pi M_s^{eff} + H_B^{\|} + H_K\right)}. \tag{4.1}$$

Note that the Kittel relation here is defined for an in-plane bias field ($H_B^{\|}$) configuration. The effective saturation magnetization M_S^{eff} and the effective field for in-plane anisotropy H_K are extracted from fitting these lines, whereas γ is used as a fixed parameter. In Figure 4.2, field-for-resonance data for NiFe(t_{FM}) are presented. It is noted that there is a size effect in $\omega(H_B)$: the thinner films have a substantially lower resonance frequency. For $t_{FM} = 2.5nm$, the resonance frequency is reduced by $\sim 5\,GHz$ from that of $t_{FM} = 30nm$, at $H_B \simeq 4kOe$. Similar size effects were observed for the other two ferromagnets $CoFeB$ and Co as well (not shown here). The induced anisotropy field H_K was found to be less than $10Oe$ in all layers for Py and $CoFeB$, and H_K didn't seem to follow any particular trend for different ferromagnetic layer thickness (therefore, we don't show it). However some of the films with Co showed a greater H_K value. For all our characterization the gyromagnetic ratio γ, which is related to the Lande g-factor g_L as[7]: $g_L/2 = |\gamma|/(e/mc)$, $|\gamma| = 2\pi \cdot (2.799 Mhz/Oe) \cdot (g_L/2)$, was assumed to be constant for each of the ferromagnets (for all thicknesses). The assumed g_L values are shown in Table 4.1. below.

Effective saturation magnetization: The effective saturation magnetization M_S^{eff},

Ferromagnet	g_L[54, 55, 7]	$4\pi M_s^{eff}(kG)$	$K_S(erg/cm^2)$
$Ni_{81}Fe_{19}$	2.09	10.7	0.69
$Co_{60}Fe_{20}B_{20}$	2.07	11.8	0.64
Co	2.15	18.3	1.04

Table 4.1: g_L is used as a constant parameter for the three Ferromagnets, $4\pi M_s^{eff}$ and K_S are extracted from Kittel fits.

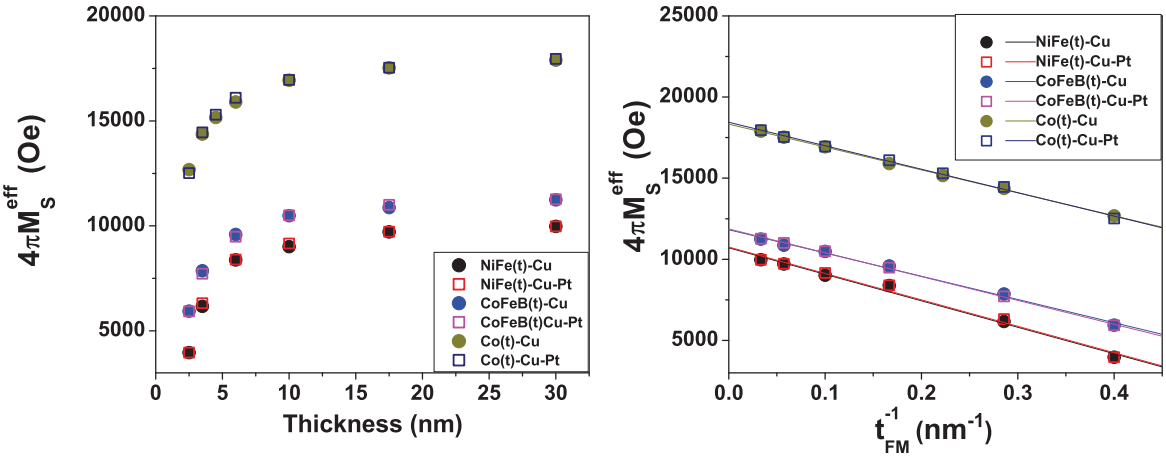

Figure 4.3: $4\pi M_s^{eff}$ for all three FM/Cu, with (filled circles) and without (open squares) Pt overlayers. Left figure shows the variation of $4\pi M_s^{eff}$ as a function of thickness of FM, and the right figure shows the same variation in inverse FM thickness.

as extracted from fitting the Kittel line, are plotted as a function of the ferromagnetic layer thickness shown in Figure 4.3(a). It is observed that M_S^{eff} depends on the thickness of the ferromagnetic layer, and this dependance is very similar in nature for all three ferromagnets ($NiFe$, $CoFeB$, Co). This variation in effective magnetization as a function of ferromagnetic layer thickness indicates that surface anisotropy plays a role. Therefore, following section 3 of chapter 1 (although we are using c.g.s. units here) we have fitted the effective saturation magnetization as: $4\pi M_s^{eff}(t_{FM}) = 4\pi M_s - (2K_s/M_s)\, t_{FM}^{-1}$[56]. These fits are shown in Figure 4.3(b). This allows the extraction of the bulk magnetization $4\pi M_s$ and surface anisotropy K_s. We tabulate all the extracted (and assumed) parameters from line position characterization in Table 4.1. The $4\pi M_s$(bulk) values are taken to be size-independent and are in good agreement with bulk values: extracted $4\pi M_s$ values are slightly larger (by 2-9%) than those measured by calibrated VSM in separate depositions of thick films. The extracted surface anisotropies are much higher than some of the published works [56]. We note that the presence of the Pt overlayer in

the heterostructures does not affect the effective magnetization of the ferromagnet.

4.1.2 Characterization using linewidth:

In Figure 4.4, we present our linewidth data. We show the linewidth variation as a function of microwave frequency, for different thicknesses of each of three ferromagnets. We have mentioned in Chapter 1 and 3, that the damping parameter α is separated from inhomogeneous broadening (if at all present) using the relation $\Delta H_{pp}(\omega) = \Delta H_0 + \left(2/\sqrt{3}\right)\alpha\omega/|\gamma|$[7]. We observe that the slope of the linear fit increases as the ferromagnetic layer thickness goes down (see Figure 4.4). This means that there is a ferromagnetic layer size effect on α, especially when the layers are thin (below 10 nm). The data for Py and $CoFeB$ show very good proportionality, with negligible inhomogeneous component $\Delta H_0 \leq 4\,Oe$ even for the thinnest layers, facilitating the extraction of the intrinsic damping parameter α (see Figure 4.4(a) and 4(c)). However for Co films a larger inhomogeneous linewidth ΔH_0 is observed whose value increases with decreasing thickness. For the thinnest Co layer it was observed to be $20\,Oe - 30\,Oe$. However, the linearity of linewidth vs. frequency is still maintained (see Figure 4.4(e)). The plots in the right side of Figure 4.4(b), (d) , (f) show the extracted α's a function of the ferromagnetic layer thickness. The extracted damping for $NiFe$, as extracted $\alpha_0^{Py} = 0.0067$ for the thickest films ($t_{FM} = 30.0nm$) to $\alpha = 0.0092$ for the thinnest films ($t_{FM} = 3.0\,nm$), increases by a factor of ~ 0.4. The same *size effect* was observed for $CoFeB$, where we find $\alpha_0^{CoFeB} = 0.0065$ for the thickest films ($t_{FM} = 30.0nm$) to $\alpha = 0.0102$ for the thinnest films ($t_{FM} = 2.5\,nm$), an increment of about factor ~ 0.5. These size effects are discussed below.

The variation of damping for the Co films are little different compared to that of $NiFe$ and $CoFeB$. We find $\alpha^{Co} = 0.0084$ for $10nm$ of Co and below this thickness the damping increases like it does for $NiFe$ and $CoFeB$, and we see $\alpha^{Co} = 0.0101$ for the thinnest films ($t_{FM} = 2.5\,nm$). But, above the thickness of $10nm$, the damping for Co increases (unlike $NiFe$ or $CoFeB$) as the thickness increases, and we find $\alpha_0^{Co} = 0.0092$ for the thickest films ($t_{FM} = 30.0nm$). The reason for this type of anomaly is not really clear to us. A possible explanation would be that surface Eddy currents might playing a role here.

We have tried to fit all of these damping values shown in Figure 4.4, with the equation $\alpha(t_{FM}) = kt_{FM}^n + C$. But we find $n \neq -1$, meaning this damping do not have inverse ferromagnetic layer thickness dependence. In fact this thickness dependence of damping was not found to follow any particular form. As we are characterizing the damping parameter, we note that sometimes it is preferred to express the damping in the form of the Gilbert damping rate $G(= \gamma\alpha M_S)$. We have presented both of these parameters

Ferromagnet	α_0	$G_0 = \gamma\alpha_0 M_S$(MHz)
$Ni_{81}Fe_{19}$	0.0067	105
$Co_{60}Fe_{20}B_{20}$	0.0065	111
Co	0.0092	234

Table 4.2: Damping parameter $\alpha_0$and Gilbert damping G_0 is presented for the thickest layer for three FM materials. The subscript (0) is used to indicate that these values are close to the bulk values.

in Table 4.2, for the thickest ferromagnetic layers which we assume are close to bulk/ intrinsic values.

Discussion of ferromagnetic layer size effect in damping:

We observe that damping in these heterostructures increases by an amount 20-50% from the thickest measured film to the thinnest one. We propose an explanation for this based on surface scattering for electrons. We find these results are analogous to the assumption made for electron scattering in the Fuchs-Sondheimer theory of surface scattering[57]. When the thickness of the ferromagnets goes down, the surface to volume ratio becomes important. More diffuse surface scattering, for thinner films, increases the resistivity, which for the short spin diffusion length (λ_{sdl}) FM materials, increases damping. It is known that the spin diffusion length λ_{sdl} for Py and $CoFeB$ are of the same order but for Co it is an order of magnitude higher. Our observed effect is stronger for Py and $CoFeB$, and roughly of the same magnitude, but not as much for Co, which validates the argument based on electron scattering from surfaces. This discussion will be continued in the last part of the next section.

4.2 Spin pumping & additional damping

One of the consequences of spin pumping is that the Gilbert damping parameter is affected by it, since it represents a loss of angular momentum. This loss mechanism and the related fundamentals were discussed in chapter 3. Here we present our experimental results and start by verifying certain theoretical predictions[22]. For this study heterostructures of the form $FM(t)/Cu/SS$ were chosen, where the damping of the precessing ferromagnet (FM) is studied as a function of its thickness, while the spin sink (SS) layer thickness was kept constant. The SS layer absorbs the pumped current from FM by means of spin flip processes or spin dephasing. Different ferromagnets Py, $CoFeB$ and Co were tested for the purpose of generating a spin current and for the spin sink SS layer, first we use Pt is used in the first series of measurement. The spin flip processes in Pt, causes the spin current absorption. Next, we use a second ferromagnet $FM2$ instead of Pt in the magnetic heterostructures $FM1(t)/Cu/FM2$. Here the spin dephasing mechanism

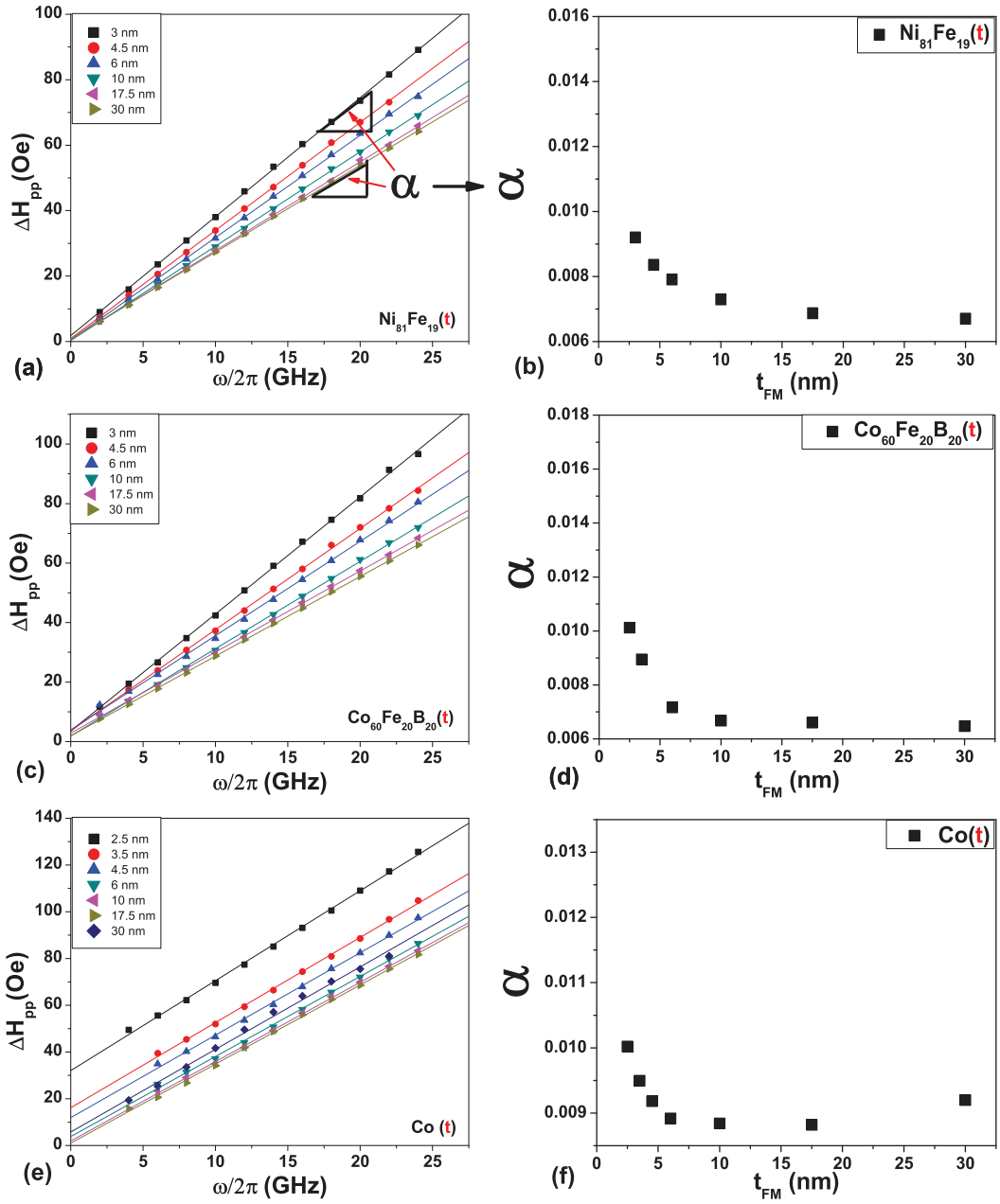

Figure 4.4: In the left side, Frequency-dependent peak-to-peak FMR linewidth $\Delta H_{pp}(\omega)$ for $FM = Ni_{81}Fe_{19}$, t_{FM} as noted, films with Pt overlayers. In the right side the extracted damping α form the linear fit.

in the second ferromagnet $FM2$, causes the spin current absorption. Based on the theory of spin pumping the damping parameter of the ferromagnetic layer which loses angular momentum to the spin sink is written in a generalized form as $\alpha\,(t_{FM}) = \alpha_0 + \triangle\alpha\,(t_{FM})$, where α_0 is the intrinsic part of the damping of the ferromagnetic layer (extracted in the previous section) and $\triangle\alpha\,(t_{FM})$ is the additional term contributed due to absorption of the spin current, by a nonlocal spin sink layer. The Gilbert damping G, $(G = \gamma\alpha M_S)$ therefore can also be expressed as $G(t_{FM}) = G_0 + \triangle G\,(t_{FM})$.

Theoretical predictions on spin pumping

There are mainly two theoretical predictions of spin pumping by Tserkovnyak et. al.[22], which was discussed in chapter 2:

• The additional damping $\triangle\alpha$ should be a Gilbert type damping, because in the LLG equation, this additional damping term has a similar form as the Gilbert damping term. This can be verified by checking the linearity of $\Delta H_{pp}(\omega)$ as a function of ω.

• The additional damping $\triangle\alpha$ has a linear dependance on the inverse of thickness of the ferromagnetic layer, i.e. $\triangle\alpha \propto 1/t_{FM}$.

4.3 Spin pumping in FM/Cu/Pt heterostructures

For the verification of spin pumping in $FM/NM1/NM2$ heterostructures, six series of heterostructures were deposited as listed in Table 3. 1 (in Chapter 3). For the FM layers: $NiFe$, $CoFeB$, and Co were tested and their thicknesses were varied from $2.5nm$ to $30nm$. More information about the growth and material composition of these heterostructures can be found in chapter 3. For each ferromagnetic layer type FM, one thickness series t_{FM} was deposited with the $Pt\,(3nm)$ overlayer (separated from FM by $NM1 = Cu$ spacer) and one thickness series t_{FM} without the Pt overlayer. This makes it possible to record the additional damping $\Delta\alpha\,(t_{FM})$ introduced by the $Pt\,(3nm)$ overlayer alone, independent of size effects present in the $FM/Cu/AlO$ layers as discussed in the last section (see Figure 4.4). The thickness of Cu is chosen to be $3nm$ which is much smaller compared to it's spin flip diffusion length i.e., $t_{Cu} \ll \lambda_{SD}^{Cu}$, and it does not contribute to spin flip. The spin pumped current which is injected to Cu reaches the $NM2 = Pt$ layer, where it is absorbed. Ideally one would like to have the $NM2 = Pt$ layer to be an ideal spin sink. A brief discussion on spin sinks was done in chapter 2, and we find, in practice it is hard to determine a material which is an ideal spin sink. However, Pt is an already tested material to be a good spin sink and $3nm$ thick Pt should be good enough spin sink [38]. The underlayer $Ta\,(5nm)/Cu\,(5nm)$ was necessary for the growth of Co to make sure that it always grows in the same crystalline phase. In order to have a good comparison of all there ferromagnetic layer types, the same underlayer

was also used for Py and $CoFeB$ structures.

$\Delta\alpha$ Gilbert type: To verify the additional damping $\Delta\alpha$ is Gilbert type, we first start with the question, what is Gilbert type damping? In the LLG equation the damping term is $\alpha\left(\mathbf{m}\times\frac{d\mathbf{m}}{dt}\right)$, better known as Gilbert damping term. In a magnetic system when the damping is purely Gilbert damping (because damping can also be caused due to two magnon scattering process, or other processes as well, see chapter 1), then the FMR linewidth ΔH_{pp} varies linearly with frequency ω, and the damping parameter α is extracted from the slope of the line. From the theory of spin pumping (discussed in chapter 2), we find the additional term, due to spin pumping (loss of spin current), added to the LLG equation, given (in a simplified form) as: $\Delta\alpha\left(\mathbf{m}\times\frac{d\mathbf{m}}{dt}\right)$. Therefore, according to the theory, if the additional damping is caused due to spin pumping, then the linewidth which contains $\alpha+\triangle\alpha$, should be linearly varying with the microwave frequency ω, which will lead to the conclusion that $\triangle\alpha$ is Gilbert type damping. To verify this, we have plotted our linewidths ΔH_{pp} as a function of frequency ω, shown in the left column of Figure 4.5, for the three FM layer materials, in heterostructures where a Pt (spin sink) overlayer is used. It is clearly seen for all the samples, that ΔH_{pp} varies linearly with frequency ω, leading to the conclusion that $\triangle\alpha$ is Gilbert type and not caused by any other processes.

$1/t_{FM}$ dependance of $\Delta\alpha$: The damping parameters, as extracted from the slope of the linear fit of linewidth vs. frequency (as shown in Figure 4.4), are plotted as a function of the FM layer thickness, shown in the right column of Figure 4.5. Black squares representing damping for structures without the Pt overlayer, and the red dots represent the ones with Pt overlayer. It is clear from these figures that the introduction of Pt in these structures enhances the damping of the FM layers. The effect is more prominent for thinner FM layers. We seek all our interpretation of this nonlocal damping size effect based on spin pumping models presented by Tserkovnyak et. al.[21]. An explicit prediction of Tserkovnyak's model is that the magnitude of the nonlocal relaxation rate $\triangle\alpha$ is only weakly dependent upon the FM layer type. The effect has been calculated following section 2.4 of Chapter 2 as [22]:

$$\triangle\alpha=\frac{|\gamma|\,\hbar}{4\pi}\frac{1}{M_S}\left(\frac{g_{eff}^{\uparrow\downarrow}}{S}\right)\frac{1}{t_{FM}}, \tag{4.2}$$

where the effective spin mixing conductance $g_{eff}^{\uparrow\downarrow}/S$ is given in units of channels per area.

In order to check for the thickness dependance ($\triangle\alpha\propto 1/t_{FM}$)**,** we take the difference $\Delta\alpha(t_{FM})$ for identical $FM(t_{FM})/Cu(3nm)/AlO(3nm)$ depositions with and without the

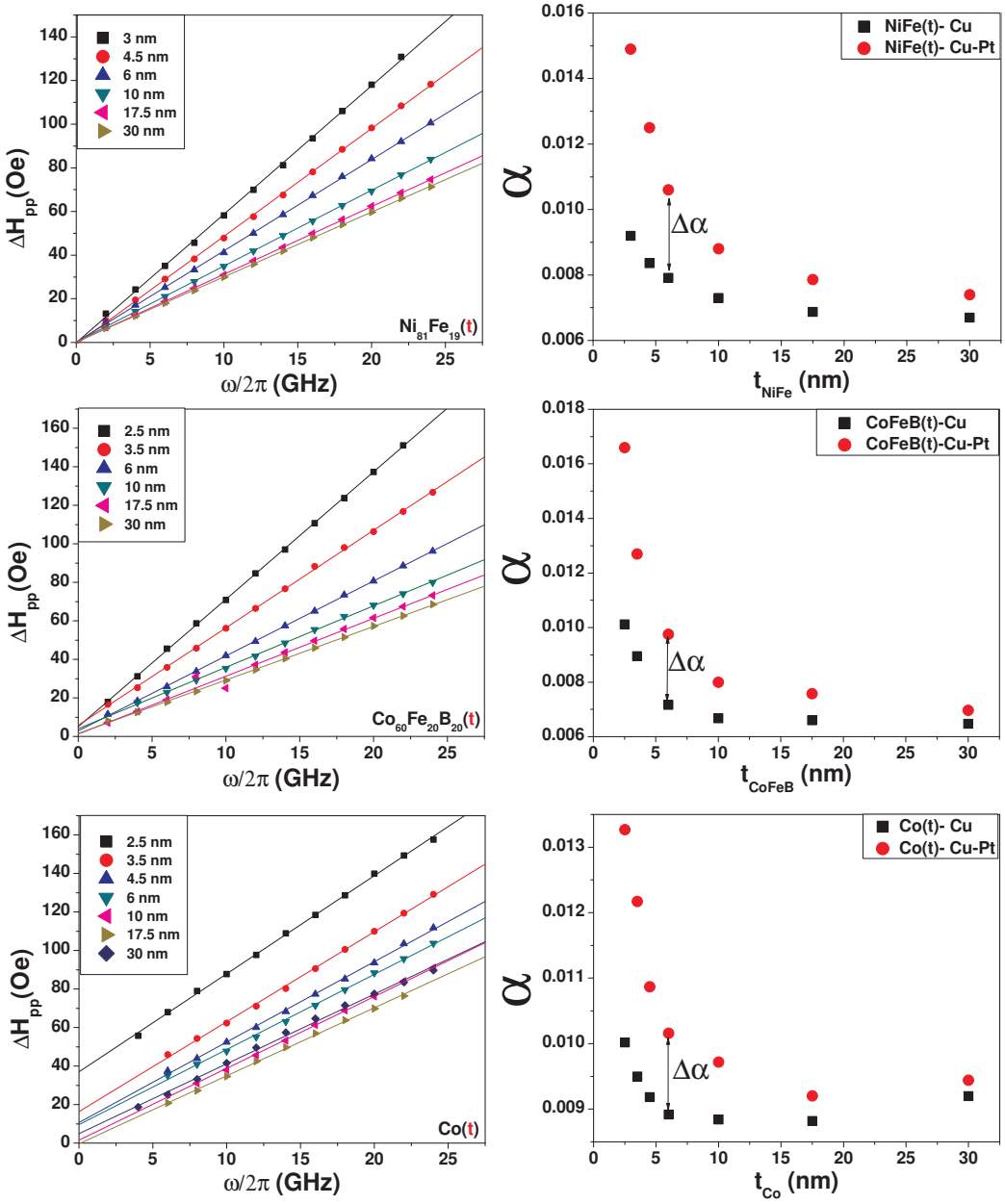

Figure 4.5: The one's in the left side represents $\Delta H_{pp}(\omega)$ as a function of ω for NiFe, CoFeB and Co heterostructures with the Pt overlayer. The one's in the right side are the contributed Gilbert damping $\Delta\alpha(t_F) = \alpha_{Pt}(t_F) - \alpha_{noPt}(t_F)$ for NiFe, CoFeB and Co

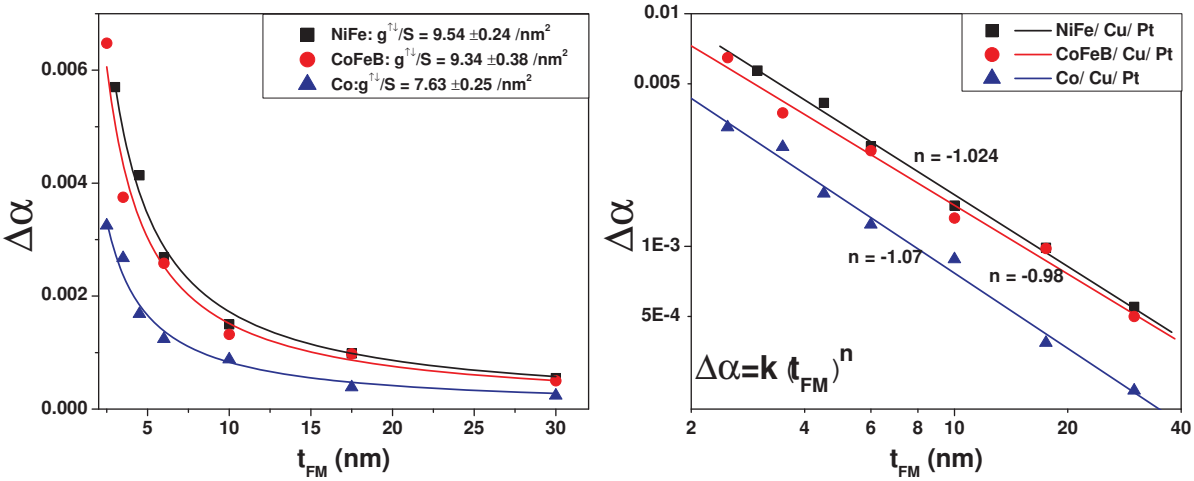

Figure 4.6: Contributed Gilbert damping $\Delta\alpha(t_{FM}) = \alpha_{Pt}(t_{FM}) - \alpha_{noPt}(t_{FM})$ for FM ($=Py$, $CoFeB$, and Co), plotted (a) in a linear scale, (b) in a log-log scale. The slopes express the power law exponent $n = -1.03 \pm 0.04$.

insertion of $Pt(3nm)$ after the Cu deposition, i.e. subtracting the black squares from the red dots. In this way the effect of the Pt overlayer i.e. the pure effect of spin pumping on the FM damping is isolated. This method will be followed for all measurements of spin pumping in this thesis. This additional damping $\Delta\alpha(t_{FM})$ is plotted as a function of the ferromagnetic layer thickness in Figure 4.6; (a) in a linear scale, (b) in a log-log scale, for all three ferromagnets. Figure 4.6(b) shows that $\Delta\alpha(t_{FM})$ is linear in t_{FM} for all three ferromagnets. All these data are found to obey a power law $\Delta\alpha(t_{FM}) = kt_{FM}^{n}$, with $n = -1.02 \pm 0.05$. This is in excellent agreement with an inverse thickness dependence $\Delta\alpha(t_{FM}) = k/t_{FM}$, where the pre-factor clearly depends on the FM layer type, highest for Py and lowest for Co. This $1/t_{FM}$ dependance of $\Delta\alpha$ leads to the conclusion that the nonlocal damping caused to the ferromagnet is due to spin pumping.

Figure 4.6(a) shows the $\Delta\alpha(t_{FM})$ variation with t_{FM} in linear scale, for three different FM layer materials. These lines are fitted with eqn. 4.2, and M_S, γ are used as constant fitting parameters (bulk values) taken from Table 4.1. From these fits of Figure 4.6(a), the effective spin mixing conductance per interfacial area $\frac{g_{eff}^{\uparrow\downarrow}}{S}$ for $FM/Cu/Pt$ structures were extracted and are listed below in Table 4.3. Note that this effective spin mixing conductance for $FM/NM1/NM1$ structures (adapting to $FM/Cu/Pt$) is a combination of several interfacial spin conductance terms and bulk terms as discussed in Chapter 2. We can write the *effective spin mixing conductance* as:

FM/Cu/Pt	$\frac{g_{eff}^{\uparrow\downarrow}}{S}$ (nm^{-2})	FM/Cu	$g_{FM/Cu}^{\uparrow\downarrow}$ (nm^{-2})
Py/Cu/Pt	9.54 ± 0.24	Py/Cu	13.25
CoFeB/Cu/Pt	9.34 ± 0.38	CoFeB/Cu	12.87
Co/Cu/Pt	7.63 ± 0.25	Co/Cu	9.8

Table 4.3: First two columns: effective spin mixing conductance $g_{eff}^{\uparrow\downarrow}$ for FM/Cu/Pt combinations, extracted from the data in Figure 4.6; second two columns: interfacial spin mixing conductance $g_{F,N}^{\uparrow\downarrow}$ from $g_{eff}^{\uparrow\downarrow}$. See text for details.

$$\left(\frac{g_{eff}^{\uparrow\downarrow}}{S}\right)^{-1} = \left(\frac{g_{FM/Cu}^{\uparrow\downarrow}}{S}\right)^{-1} - \frac{1}{2}\left(\frac{g_{Cu,Sh}^{\uparrow\downarrow}}{S}\right)^{-1} + \frac{2e^2}{h}t_{Cu}\rho + \left(\frac{\tilde{g}_{Cu/Pt}}{S}\right)^{-1}, \tag{4.3}$$

where $g_{FM/Cu}^{\uparrow\downarrow}$ is the interfacial *spin mixing conductance* of the FM/Cu interface, $g_{Cu,Sh}^{\uparrow\downarrow}$ is the Sharvin conductance of Cu, and $\tilde{g}_{Cu/Pt}$ is the interfacial *spin conductance* of Cu/Pt interface. For the bulk contribution of the $3nm$ Cu spacer, we consider at room temperature $\rho_{Cu} = 20\,\Omega \cdot nm$, and obtain: $\frac{2e^2}{h}t_{NM1}\rho \sim 1/215\,nm^{-2}$[58]. We can assume the Sharvin conductance contribution of Cu as $g_{Cu,Sh}^{\uparrow\downarrow}/S = 15.0\,nm^{-2}$, in order to extract the few unknown parameters. Therefore we are left with four unknown quantities now, which are $g_{FM/Cu}^{\uparrow\downarrow}$ for three FM/Cu combinations and $\tilde{g}_{Cu/Pt}$. But, we have three equations from three different series of measurements. Therefore we assume one more quantity which is $\tilde{g}_{Cu/Pt}/S = 17.2\,nm^{-2}$ from Table 3. 1 (in Chapter 3). Inserting all these parameters we extract $g_{FM/Cu}^{\uparrow\downarrow}/S$ for three FM/Cu combinations, which are shown in column 4 of Table 4.3. We see that our extracted $g_{FM/Cu}^{\uparrow\downarrow}/S$ [58] values are slightly lower compared to the calculated ones (from Table 1 of ref. [22] we find $g_{Co/Cu}^{\uparrow\downarrow}/S = 14.1\,nm^{-2}$ and experimentally measured by us, which will be discussed in the next section [33]. This small discrepancy could be due to slightly different values assumed for certain parameter(s).

Expressing now the additional Gilbert relaxation rate as $\Delta G(t_{FM}) = |\gamma| M_s \Delta\alpha(t_{FM}) = |\gamma| M_s K_{FM}/t_{FM}$, we plot $\Delta G \cdot t_{FM}$ in Figure 4.7. We find $\Delta G \cdot t_{Py} = 263 \pm 30 Mhz$, $\Delta G \cdot t_{CoFeB} = 258 \pm 35 Mhz$, and $\Delta G \cdot t_{Co} = 216 \pm 40 Mhz$, as shown by the dotted lines. The similarity of values for $\Delta G \cdot t_{FM}$ is in good agreement with predictions of the spin pumping model expressed by the equation: $\Delta G \cdot t_{FM} = |\gamma|^2 \hbar/4\pi \left(g_{eff}^{\uparrow\downarrow}/S\right)$, given that interfacial spin mixing parameters are nearly equal in these systems. The ferromagnetic layer thickness dependance of nonlocal damping has been reported in the past by several groups [38, 39, 47], but interpreted based on different mechanism, which we have already

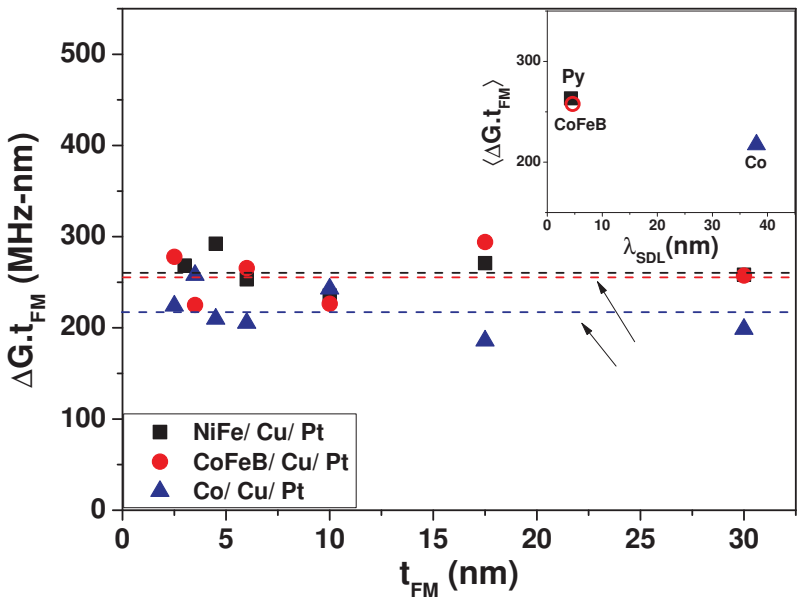

Figure 4.7: The additional nonlocal relaxation due to Pt overlayers, expressed as a Gilbert relaxation rate - thickness product $\Delta G \cdot t_{FM}$ for Py, CoFeB, and Co. *Inset:* dependence of $\Delta G \cdot t_{FM}$ on spin diffusion length λ_{SD} as tabulated in ref. [42].

discussed in the last section of Chapter 2. In one such work, the nonlocal damping was interpreted based on a "resistivity-like" mechanism by Ingvarsson et. al. [47]. Below, we discuss Ingvarsson's interpretation and why we believe that spin pumping is causing this nonlocal damping and discard the "resistivity-like" mechanism.

Additional damping: Spin pumping or Resistivity?

The nonlocal size effect in damping, which we claim, is due to spin pumping, is also a strong reminiscent of the electrical resistivity in ferromagnetic ultrathin films. Electrical resistivity ρ is size-dependent and it varies in a similar manner as the nonlocal damping does for a similar range of t_{FM}. Also it is known that the resistivity $\rho(t_{FM})$ is nonlocal and it depends on layers which are not in direct contact with the ferromagnet [59, 60]. Therefore, it is plausible that the nonlocal damping and nonlocal electrical resistivity share a common origin in momentum scattering (with relaxation time τ_M) by overlayers.

While discussing the possible origins of intrinsic damping in Chapter 1, we have discussed two mechanisms based on scattering of itinerant electrons with phonons and magnons, which leads to spin flip. In those two mechanisms, we have found there are ferromagnets like Fe and few alloy's, for which damping is 'resistivity' like. For alloy's, it is thought that their short spin diffusion length λ_{sdl}, makes them falling into this category and for them the damping is thought to be inversely proportional to the orbital relaxation time: i.e. τ_{orb}^{-1} (ref. [8]). However, metals like pure Ni or Co with a long λ_{sdl},the

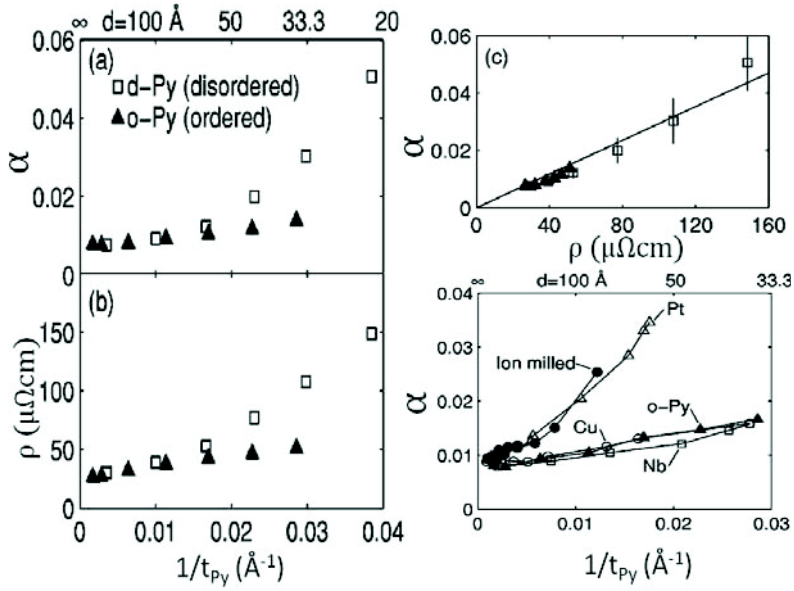

Figure 4.8: On the left damping α and resistivity ρ for disordered Permalloy (d-Py) and ordered Permalloy (o-Py) are plotted as observed by Ingvarsson et. al[47]. On the right, correlation between α and ρ is shown (top), and the effect of Pt, Nb layers (in direct contact with Py), on Py damping is shown (bottom).

relaxation is found to be either nearly constant with temperature or "conductivity-like", scaling as τ_{orb}.

The claim for "resistivity-like" damping has been made explicitly for $Ni_{81}Fe_{19}$ by Ingvarsson et. al. [47], based on Fuchs-Sondheimer theory of electron scattering from surfaces. They have studied damping (intrinsic + nonlocal) and resistivity as a function of $NiFe$ layer thickness, which is shown in Figure 4.8. Resistivity ρ and damping α is found to vary quite similarly with t_{Py}, for the same t_{Py} range. In our study of spin pumping the ferromagnets, Py, $CoFeB$ and Co, that are used have different spin diffusion lengths $\lambda_{sdl}^{Py} = 3 - 5\,nm$, $\lambda_{sdl}^{CoFeB} = 4 - 6\,nm$, $\lambda_{sdl}^{Co} = 38 - 58\,nm$ [61, 62, 42, 63]. In Figure 4.7, *inset*, we show the dependence of $\Delta G \cdot t_{FM}$ upon the tabulated λ_{sdl} of these layers. It can be seen that λ_{sdl}^{Co} is roughly an order of magnitude longer than it is for the other two FM layers, Py and $CoFeB$, but the contribution of Pt overlayers to damping for these three ferromagnets are very close to their average. However, if the nonlocal damping arises from nonlocal scattering τ_{orb}^{-1}, there should be a marked dependence on the ferromagnetic material. Since under the resistivity mechanism, only Py and $CoFeB$ should be susceptible to a resistivity contribution in $\Delta\alpha(t_{FM})$, and Co should be susceptible to a conductivity contribution, the results imply that the contribution of Pt to the

nonlocal damping size effect has a different origin, which is spin pumping.

Summary:

To summarize, we have presented a common methodology, by taking into account damping size effects (without spin sink), of studying spin pumping in magnetic heterostructures using different ferromagnets. In prior work, study of nonlocal damping has been reported for different ferromagnets: Py [64, 37, **?**], $CoFeB$ [65] and Co [66, 67]. However, we find that the nonlocal damping in these studies were interpreted based on different mechanisms. Therefore, the numerical comparison of the results obtained by them becomes difficult and sometimes problematic as these experiments do not share a common methodology. Note that, many times the analysis to some extent can be model-dependent [49]. In our experiments, we have taken care to isolate the nonlocal damping contribution due to Pt overlayers only, controlling for growth effects, interfacial intermixing, and inhomogeneous losses. The only variable in our comparison of nonlocal damping $\Delta\alpha(t_{FM})$, to the extent possible, has been the identity of the FM layer. We have observed that the additional damping contributed due to spin pumping is Gilbert type. We observe, for Cu/Pt overlayers, the same power law in thickness $t^{-1.02\pm0.05}$, and very similar materials independence. The rough independence of the FM spin diffusion length, shown here for the first time, argues against a resistivity-based interpretation for the effect.

4.4 Spin pumping and enhanced damping in Py(t)/ Pt structures:

As an extension of our spin pumping study for $FM(t)/Cu/Pt$ heterostructures as presented in the last section, we present here a specific case where the spin sink is in direct contact with the ferromagnet. We have used $Py(t)/Pt$ heterostructures and the reference structure $Py(t)/Cu$ for this study, and in both these cases the seed layer and the cap are the same as before (for more details see Table 3.1 in Chapter 3). Note that unlike the last section where in all the cases the precessing ferromagnet was always surrounded by Cu from both the sides, in this case we will have Pt in one side, however for the reference structure it is still Cu. Since our data extraction and interpretation depends a lot on comparison of structures with and without spin sink, we must be careful and consider it is not exactly the same here.

The verification of Gilbert type damping (linewidth $\Delta H_{pp}(\omega)$ is linear with microwave frequency ω) was done for $Py(t)/Pt$ structure (not shown here). The damping parameter $\alpha(t_{Py})$ as extracted from the slope of $\Delta H_{pp}(\omega)$ vs. ω plot, is presented in Figure 4.9(a) $Py(t)/Pt$ and $Py(t)/Cu$ structures. It is clearly observed that the enhancement

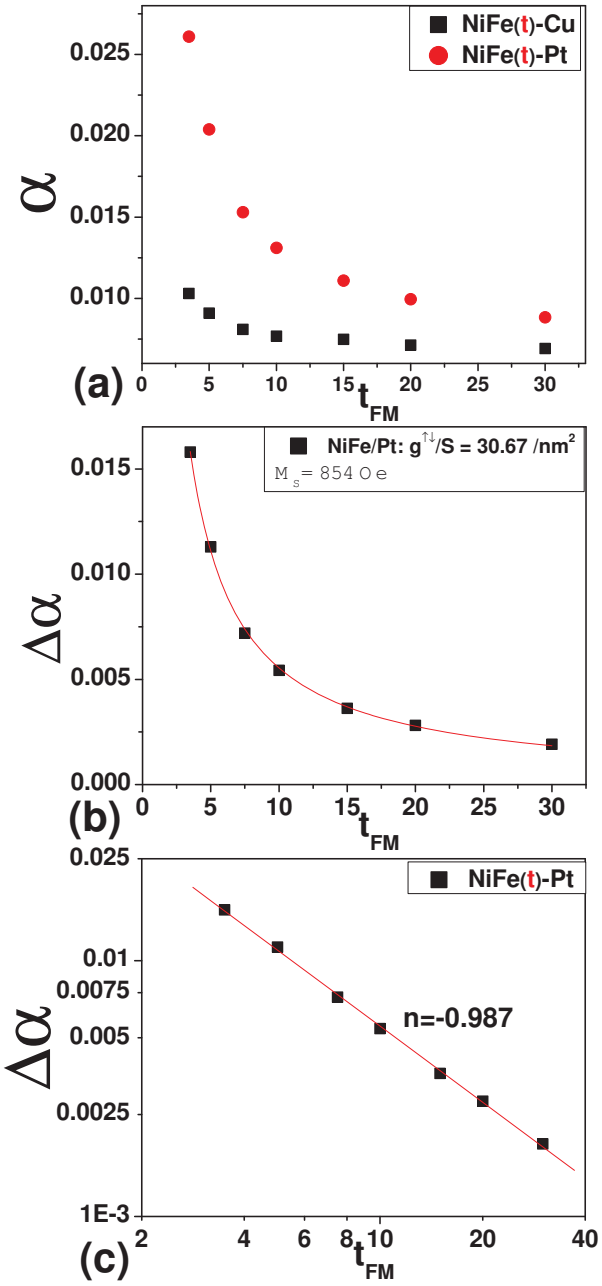

Figure 4.9: Damping parameter for Pt in direct contact with Py. (a) red dots represents $\alpha(t_{Py})$ for Py/Pt structure and black squires represents $\alpha(t_{Py})$ without the Pt overlayer. (b) Additional damping $\Delta\alpha(t_{Py})$ is plotted as a function of t_{Py} (b) in linear scale, (c) in Log-log scale.

in damping by the addition of Pt directly on top of Py is much more prominent as compared to $Py(t)/Cu/Pt$ structures as presented in Figure 4.5. The additional damping $\triangle\alpha$ is plotted as a function of t_{Py} in Figure 4.9(b) in a linear scale, and 9(c) in a log-log scale. From the linear scale plot, we fit the curves using eqn. 4.2, which enables us to extract the spin mixing conductance per interfacial area for the Py/Pt interface, which is $\frac{g^{\uparrow\downarrow}_{Py/Pt}}{S} = 30.67\, nm^{-1}$. From the log-log plot we verify the second prediction of spin pumping that $\triangle\alpha$ varies as $\Delta\alpha(t_{FM}) = kt^n$; finding the power of t as: $n = -0.987$. Our extracted spin mixing conductance parameter is in good agreement with the observation of Mizukami et. al.[46, 64]. Note that when the Cu spacer is introduced in between Py and Pt layer, the interfacial spin conductances are added in parallel, reducing the effective value for the whole structure.

4.5 Spin pumping in spin valve FM1(t)/ Cu/ FM2 structures

In this section we discuss our study of spin pumping in $FM1(t)/NM/FM2$ "spin-valve" structures. The sample preparation method was the same as before and the complete heterostructures list is given in Table 3.1 (in chapter 3). The $FM1/FM2$ combinations chosen were $Py/CoFeB$, Py/Co, $CoFeB/Co$, which was done keeping in mind the separation of FMR of the $FM1$ and $FM2$ layers. A discussion on separating resonances in this type of structure will be presented in Chapter 5. The Cu spacer, which separates $FM1$ and $FM2$, was chosen to be $5nm$ to be sure about the absence of the RKKY exchange interaction. Like the last section here also for each of the $FM1$ type one layer was prepared with, and without $FM2$ ferromagnetic overlayer, and the thickness of $FM1$ was varied between $3 - 30nm$. The additional damping caused purely due to the $FM2$ overlayers have been extracted in a similar manner as discussed in the previous section. A sample data of $NiFe(t)/Cu5nm/Co5nm$, showing the linewidth variation with frequency ω, is presented in Figure 4.10(a). This shows that the nonlocal *additional damping* is Gilbert type. Figure 4.10(b) shows the extracted damping α of $NiFe(t)$; red dots represents $\alpha_{FM2}(t_{FM1})$ (with $FM2 = Co$ as overlayer) and black squares represents $\alpha_{noFM2}(t_{FM1})$ (without the $FM2 = Co$ overlayer) as extracted from the slope of ΔH_{pp} vs. ω plot. It is clearly observed that the addition of the $FM2$ layer, enhances the damping of $FM1$, and this effect is more dominant for thinner $FM1$ layers.

The difference $\Delta\alpha(t_{F1}) = \alpha_{FM2}(t_{F1}) - \alpha_{noFM2}(t_{F1})$ which isolates the sole effect of $FM2$ in the damping of precessing $FM1$, is plotted in Figure 4.11; (a) in a linear scale, (b) in a log-log scale, for all three ferromagnets. For the verification of the second prediction of spin pumping, we look at the slope of the line plot in log-log scale (Figure 4.11), which

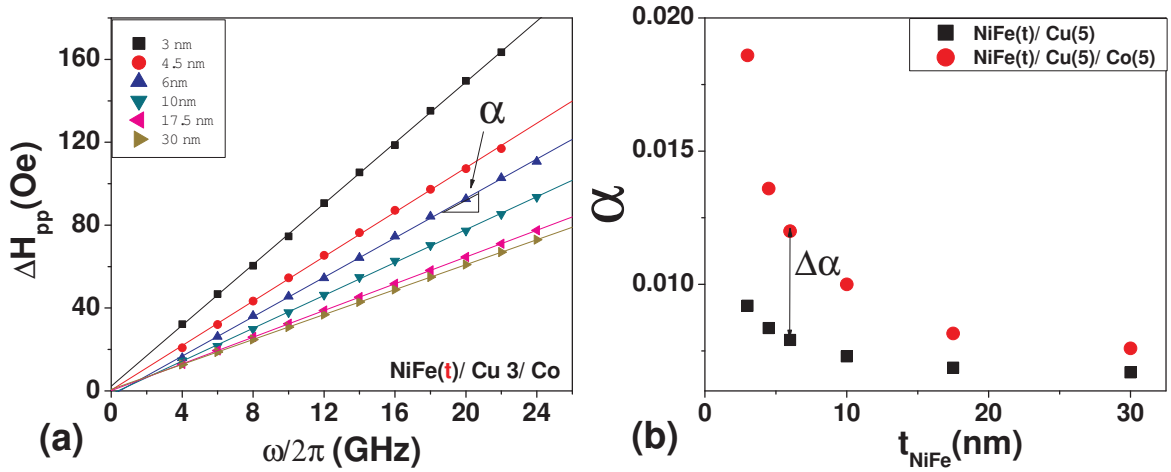

Figure 4.10: (a) Frequency-dependent peak-to-peak FMR linewidth $\Delta H_{pp}(\omega)$ for $FM = Ni_{81}Fe_{19}$, t_{FM} as noted, films with $Co(5nm)$ overlayers. (b) red dots represents$\alpha_{FM2}(t_{F1})$ (with the $FM2 = Co$ overlayer) and black squares represents $\alpha_{noFM2}(t_{F1})$ (without the $FM2 = Co$ overlayer) as extracted from the slope of ΔH_{pp} vs. ω plot.

shows $\Delta\alpha(t_{FM1}) = Kt_{FM1}^{n}$, with $n = -1.07 \pm 0.05$. For power-law, this is in excellent agreement with the inverse thickness dependence of contributed damping predicted from spin pumping; $\Delta\alpha(t_{FM1}) = |\gamma|\hbar/4\pi M_s g_{eff}^{\uparrow\downarrow}/t_{FM1}$.

The effective spin mixing conductance per interfacial area $\frac{g_{eff}^{\uparrow\downarrow}}{S}$, for our heterostructures are extracted from fitting our data in Figure 4.10(a) by eqn. 4.2. These parameters are listed in the second column of Table 4.4. As discussed in Chapter 2, the effective spin mixing conductance parameter for the $FM1/NM/FM2$ structures, after considering the Sharvin conductance of NM and ignoring the bulk resistivity term, can be written in the form:

$$\left(\frac{g_{eff}^{\uparrow\downarrow}}{S}\right)^{-1} = \left(\frac{g_{FM1/NM}^{\uparrow\downarrow}}{S}\right)^{-1} - 2\cdot\left[\frac{1}{2}\left(\frac{g_{NM}^{Sh}}{S}\right)^{-1}\right] + \left(\frac{g_{FM2/NM}^{\uparrow\downarrow}}{S}\right)^{-1}, \qquad (4.4)$$

where $\frac{g_{FM1/NM}^{\uparrow\downarrow}}{S}$, $\frac{g_{FM2/NM}^{\uparrow\downarrow}}{S}$ are the interfacial *spin mixing conductances* for $FM1/NM$, $FM2/NM$ interfaces and $\frac{1}{2}\left(\frac{g_{NM}^{Sh}}{S}\right)$ is the Sharvin conductance term coming from the Cu side, for each of the FM/Cu interfaces[22]. Assuming the Sharvin conductance value for Cu to be $g_{S,N} = 15.0nm^{-2}$[22], the effective spin mixing conductance for each of the three different FM/Cu interfaces are extracted in the following manner. Three linear equations for $\left(g_{eff}^{\uparrow\downarrow}/S\right)^{-1}$ can be written in terms of two values of $\left(g_{FM1,2/Cu}^{\uparrow\downarrow}/S\right)^{-1}$ each; the system is solved for the three unknown interface values $g_{FM/Cu}^{\uparrow\downarrow}/S$. The "bare" spin mixing conductances $g_{FM/Cu}^{\uparrow\downarrow}/S$ are tabulated in column 4 of Table 4. 4, for comparison

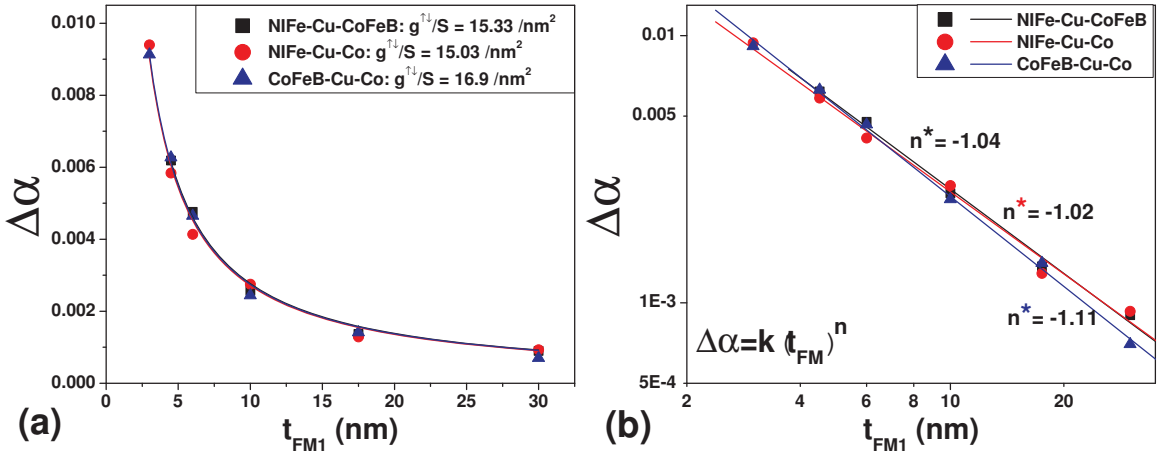

Figure 4.11: Contributed Gilbert damping $\Delta\alpha(t_{FM1}) = \alpha_{FM2}(t_{FM1}) - \alpha_{noFM2}(t_{FM1})$ from the introduction of a second $FM2$ interface in $FM_1(t_{FM_1})/Cu(5nm)[/FM_2]/AlO(2nm)$ structures, plotted (a) in a linear scale, (b) in a log-log scale.

$FM1/NM/FM2$	$\frac{g_{eff}^{\uparrow\downarrow}}{S}$ (nm^{-2})	$FM1/Cu$ (analyzed)	$\frac{g_{FM/Cu}^{\uparrow\downarrow}}{S}$ (nm^{-2})
Py/Cu/Co	15.0 ± 1.5	Py/Cu	14.4 ± 1.4
Py/Cu/CoFeB	15.3 ± 1.5	CoFeB/Cu	16.0 ± 1.6
CoFeB/Cu/Co	16.8 ± 1.6	Co/Cu	15.7 ± 1.6

Table 4.4: First two columns: effective spin mixing conductance $g_{eff}^{\uparrow\downarrow}$ for $FM1/Cu/FM2$ combinations, extracted from the data in Figure 4.10; second two columns: interfacial spin mixing conductance $g_{FM,NM}^{\uparrow\downarrow}$ from $g_{eff}^{\uparrow\downarrow}$. See text for details.

with calculated values.

We highlight the close agreement of the three polycrystalline interfacial spin mixing conductances with each other and with theory. The three $g_{FM/Cu}^{\uparrow\downarrow}/S$ values found from measurements of $\Delta\alpha$ all agree with the theoretical $g_{FM/Cu}^{\uparrow\downarrow}/S$[22] for alloyed Co/Cu, $14.6\,nm^2$, within 10%. The measurements presented so far strongly support the idea that the interfacial damping in $FM1/Cu/FM2$ arises from the spin pumping effect.

4.6 Summary

The primary motivation of this chapter was to verify the spin pumping mechanism for different ferromagnets using different spin sink materials. This was to show that spin pumping is not a material specific phenomenon, rather it is a general spin current transport related phenomenon. This effect has always been existing in ferromagnetic heterostructures whenever there is precession of magnetization. However in the past this effect as observed by others, was understood and interpreted differently [38, 39, 47]. In this chapter of the thesis, we have presented a systematic experimental study by

considering a common methodology, and have tested several materials. Our experimental method of broadband field swept ferromagnetic resonance is a very well established method and quite simple to use. Broadband FMR measurement has it's merit over the single frequency FMR (cavity) measurements, as the the extracted data is averaged over many points, the error is minimized. Because these measurements do not require device nanofabrication, they are rapid, allowing a larger number of layers to be characterized in finite time. In prior experimental work, studies on spin pumping has been reported, but this is the first time the subtraction method is employed to extract nonlocal additional damping ($\Delta\alpha(t_{FM}) = \alpha_{SS}(t_{FM}) - \alpha_{noSS}(t_{FM})$) caused due to spin pumping effect. For most of our studies (other than $Py(t)/Pt$ series), the ferromagnet under investigation (precessing layer) was always surrounded by Cu from both the sides, to avoid the effects of any different interface, that makes the comparison more difficult. For all our studies we have verified two main predictions of spin pumping, which are (1) additional nonlocal damping caused due to spin pumping is Gilbert type, and (2) the additional nonlocal damping is inversely proportional to the ferromagnetic layer thickness. The rough independence on FM spin diffusion length, shown here for the first time, argues against a resistivity-based interpretation for the effect. Our study of nonlocal additional damping, enabled us to characterize a very important spin current transport related interfacial parameter $\frac{g_{eff}^{\uparrow\downarrow}}{S}$. This parameter known as spin mixing conductance has been characterize for the whole magnetic structure, due to the combination of different FM plus NM materials in the heterostructures, it was possible under some approximation, to isolate $\frac{g_{eff}^{\uparrow\downarrow}}{S}$ for three particular FM/Cu interfaces. It was shown in chapter 2, that these spin mixing conductance parameters are the same for STT and spin pumping. This makes, the characterization of this parameter, even more important and the technique that we have shown here is quite convenient, rapid and a very reliable method.

Chapter 5

Spin injection in FMs, NMs and AFM

As demonstrated in Chapter 4, precession of magnetization of a ferromagnetic (FM) layer can be used to generate a pure spin current into it's adjacent metallic layers, via the spin pumping effect. This pure spin current can be injected into the other metallic layers, present in the magnetic heterostructures, which can be a nonmagnetic metal or a second ferromagnet or an antiferromagnet, separated by a spacer (nonmagnets can be used in direct contact with the ferromagnet) [43, 39]. This offers an alternative means for the study of spin current transport in metals, where a precessing ferromagnet is used as the source of pure spin current. This type of spin injection has been used to study the inverse spin hall effect (ISHE) [23]. In this chapter we focus on the spin current decay/ absorption by different spin sink materials. Mesoscopic transport using charge currents or *spin polarized* charge currents (i.e. spin current coupled to charge current), has been an important field of study in nanoscience in the last two decades. However, the realization of pure spin currents and it's impact on magnetic structures is relatively recent, and is currently studied in many experiments. Our detection technique for spin current (absorption) is indirect. as we study the enhancement of FMR linewidth. This is somewhat different compared to spin polarized charge current transport, as we do not use any external bias voltage or current.

The schematic in Figure 5.1 shows pure spin current generation by ferromagnet and its injection and absorption in a ferromagnet (antiferromagnet) or nonmagnet (paramagnet). The precessing ferromagnet ($FM1$, FM) generates a pure spin current in Cu, which results in an imbalance in the chemical potential $\triangle\mu = \mu^{\uparrow} - \mu^{\downarrow}$ at the vicinity of the $ferromagnet/Cu$ interface. Since Cu has a large spin diffusion length λ_{sdl} [42], it is considered that a very thin layer of Cu $(3-5nm)$ does not flip the injected spin current.

Therefore, the injected spin current after traversing through the Cu ($t_{Cu} \ll \lambda_{sdl:Cu}$) spacer, reaches the *spin sink* (FM_2 *or* AFM *or* PM) layer, where it is absorbed. We note that the pumped out spin current traveling perpendicular to the FM/Cu interface, has a *transverse* and a *longitudinal* component (see Chapter 2, and ref. [22]). Considering small angle precession, only the transverse component contributes to the additional damping $\triangle\alpha$. In this chapter, $\triangle\alpha$, which is a measure of transverse component of spin current loss, is studied as a function of thickness of various spin sink materials. This study will enable us to understand, mainly, how the transverse component of the spin current decays in various materials and the length scales of the decay. Since the spin current absorption mechanism in different spin sinks (ferromagnets, antiferromagnets and paramagnets) are different, it is expected to observe different absorption characteristics and length scales for different materials. Throughout this chapter we will present the consequences of these different absorption mechanisms and we will try to address certain fundamental questions related to pure spin current absorption. Similar type of studies has been reported by Taniguchi et al. [34] for the ferromagnetic spin sink absorber, Foros [68] and Mizukami [38] for paramagnetic absorbers. However, our results with ferromagnetic spin sink absorber is not quite in agreement with Taniguchi et al. Even though, our results with paramagnetic spin sink layers agrees with Foros et al. and Mizukami et al.'s work, the model that they have used for their interpretation, is something that is less convenient for us.

5.1 Spin current absorption by spin sink metals

In this section we will discuss briefly the mechanisms involving spin current decay/ absorption in ferromagnets and nonmagnets (paramagnets). The schematics shown in Figure 5.1(a) demonstrates spin current decay in ferromagnets, and (b) shows the same in nonmagnets (or paramagnets). In our discussion of spin transfer torque in chapter 2, we have already mentioned that when spin polarized current enters a ferromagnet through a NM/FM junction, the transverse component of it precesses around the exchange field of the ferromagnet which eventually results in classical *dephasing* of the transverse component. The length scale is set by the transverse spin coherence length, given to first order by $\lambda_J \sim \pi/|k_f^{\uparrow} - k_f^{\downarrow}|$ where $k_f^{\uparrow(\downarrow)}$ are the majority (minority) Fermi wave vectors[31], or equivalently $\sim h v_g/2\Delta_{ex}$, with v_g as the spin-averaged group velocity and Δ_{ex} the exchange splitting[69]. This quantity is estimated at $1 - 2\,nm$ near the Fermi energy in $3d$ ferromagnets[70]. The functional form predicted for the total transverse spin current absorption approximates an algebraically decaying sinusoid about a step function [32, 71], with differences depending upon the Fermi surface integration[70, 31, 32, 72].

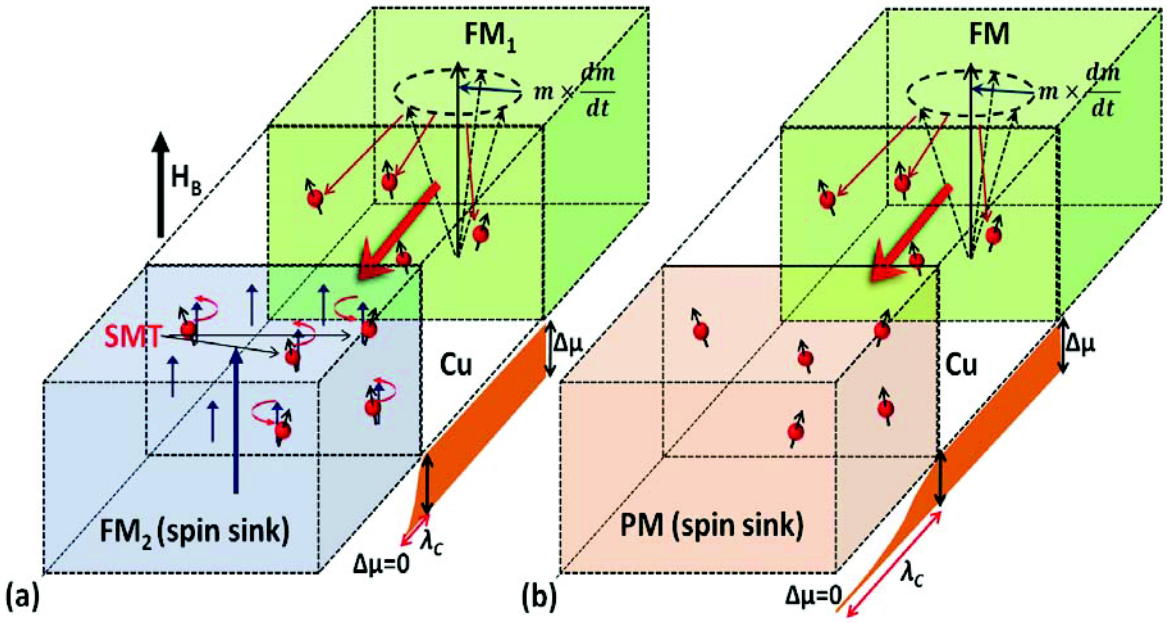

Figure 5.1: Pure spin current emitted from the precessing ferromagnet traversing through Cu spacer to (a) ferromagnet (b) paramagnetic spin sink layer where it is absorbed.

Experimental results in the regime $t \leq \lambda_J$ exist only for hot electrons $E - E_F \geq 5eV$, injected and detected from vacuum using Mott polarimetry[69, 73].

Prior magneto-transport measurements have indicated the existence of a *characteristic length* for spin current absorption near the Fermi energy in $3d$ ferromagnets. An exponential decrease of spin polarized current density with increasing depth z in the ferromagnet as $\exp -z/\lambda_{sdl}$, was revealed by giant magneto-resistance measurements[74, 75], where λ_{sdl} is the spin diffusion length. The exponential depth dependence reflects a Poisson process for spin relaxation: spin-flip scattering events are uncorrelated over a distance with a uniform probability depth distribution. However, we find all of these measurements refer to the *longitudinal* component of spin, parallel and anti-parallel to the direction of magnetization $\mathbf{m}$ of FM, whereas we are interested in the absorption of the transverse component. Even though this *decoherence* length for the transverse component has been calculated theoretically, not much of experimental evidence exist to support this. Therefore, studying this spin dephasing phenomenon in terms of spin current absorption in ferromagnets and characterizing the length scale was one of our primary interest. In the following section of this chapter, we will present our study of the spin dephasing length in various ferromagnetic ($NiFe$, $CoFeB$, Co), and one anti-ferromagnetic ($MnIr$) spin sink.

The spin current absorption by nonmagnets (or paramagnets) could be understood by their spin flip mechanism. The paramagnetic spin sinks chosen by us (Pt, Pd, Ru)

are known to have a large spin relaxation rate or relatively short spin diffusion lengths. As discussed in chapter 2, the spin flip efficiency and the length scale depends primarily on three factors, (1) it's spin diffusion length, (2) availability of p or d electrons in it's conduction band and (3) its atomic number Z. It is also noticed that the spin-flip efficiency of a dirty metal could be determined by defects and impurities as well. The injection of a spin current at the Cu/PM interface decays over the paramagnets spin diffusion lengthλ_{sdl}. We study spin current absorption in various nonmagnets (or paramagnets) and compare our results the predictions [22], and with others work[38, 68]. While studying the spin current absorption by paramagnets we will consider two types of structures, (1) when these above mentioned spin sink layers are separated from the ferromagnet with a Cu spacer, and (2) when they are in direct contact with the ferromagnet.

5.2 Spin injection FM1/ Cu/ FM2(t) structures

In this section we present our study of spin injection in ferromagnets and antiferromagnets using a spin-valve structures $FM1/\,NM/[\,FM2(t)\,or\,AFM]$, where the precessing layer $FM1$ sources ("pumps") a spin current across the $NM(Cu)$ and into $FM2$ or AFM , where it is absorbed after transferring momentum. We have used three structurally diverse ferromagnets ($Ni_{81}Fe_{19}$ ("Py,"), $Co_{60}Fe_{20}B_{20}$ ("$CoFeB$"), pure Co and one antiferromagnet ($Ir_{80}Mn_{20}$ ("$IrMn$")) as a spin current absorber. The thickness-dependent onset of the enhanced damping has been used as a measure of spin current absorption. The additional damping $\Delta\alpha$ contributed by the ferromagnet FM_2 or AFM to the precessing ferromagnet FM_1 is the parameter of our interest. The thickness ranges used for the spin sink FM_2, AFM layer were; $t_{F2,AFM} = 0.5 - 15nm$. Three series of heterostructures were deposited using $FM1 \mid FM2\,(t_{FM2})$ combinations as: $Py(10nm) \mid Co(t)$, $Co(8nm) \mid CoFeB(t)$, and $Co(8nm) \mid Py(t)$. Details about the heterostructures can be found in Table 1 of Chapter 3. Care has been taken in the deposited sample series to isolate the effect of these covering layers (to extract $\Delta\alpha$) alone by preparing one sample without the spin sink overlayer coverage. The technique is the same as was presented in Chapter 4.

Since for this study, two ferromagnets have been used, special care has been taken so that the resonances of the two ferromagnetic layers stays apart. This was done by choosing suitable combinations and thicknesses of the precessing layer $FM1$. However, for frequencies below $6\,GHz$ resonance separation wasn't possible and all our data obtained for this study was therefore in the range $6 - 24\,GHz$. A sample data is presented in Figure 5.2(a) showing field-swept FMR spectra at $16\,GHz$ for $Co(8nm)/Cu(5nm)/CoFeB(t_{CoFeB})$,

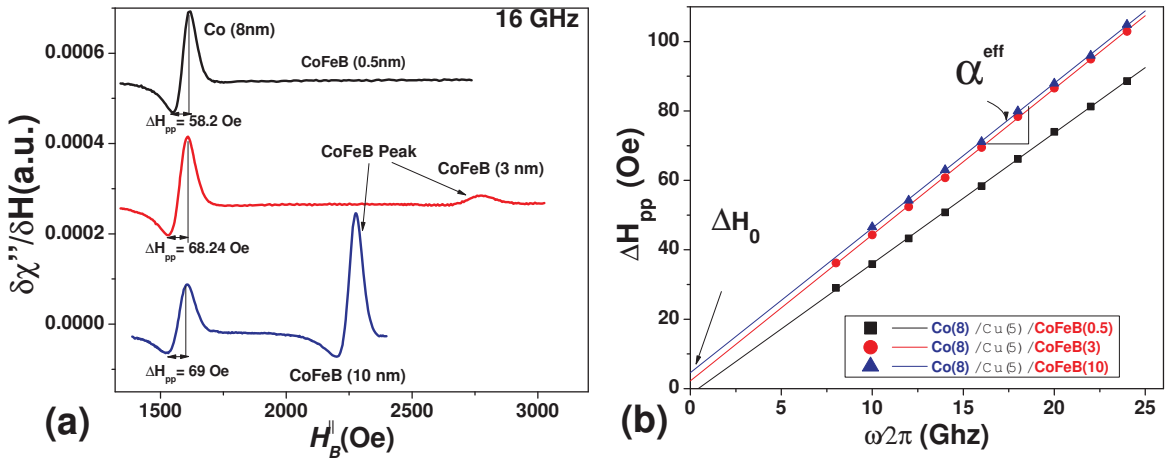

Figure 5.2: Isolation of contribution to Gilbert damping in $FM1/Cu/FM2(t_{F2})$, $FM1 = Co(8nm)$, $FM2 = CoFeB(t_{CoFeB})$. (a) Derivative FMR spectra, $16\,GHz$, $t_{CoFeB} = 0.5nm$, $3.0nm$, and $10.0nm$. Note the increase in linewidth for the *Co resonance* (low field) as a function of t_{CoFeB}. (b) separation of intrinsic and extrinsic damping for different t_{CoFeB}.

$t_{CoFeB} = 0.5$, 3.0, and $10.0nm$. Resonances are well-separated (through the choice of $FM1$, $FM2$ combinations) and the *low-field* $Co(8nm)$ resonance is monitored as a function of $CoFeB$ coverage. The effect of $CoFeB$ thickness increment from $0.5\,nm$ to $10\,nm$ is clearly seen as the linewidth of Co increases from $58.2\,Oe$ to $69\,Oe$. From this we see that it is possible to detect the effect of angstrom-scale coverages of $CoFeB$ ($FM2$) on the low-field Co resonance ($FM1$). Even as the $CoFeB$ resonance itself is at the threshold of visibility, not observed at $0.5\,nm$ and eventually observed at $3.0\,nm$, the spin current absorption in $CoFeB$ can be measured through an increase of the Co linewidth by$\sim 10\,Oe\,(19\%)$. In Figure 5.2(b), the linewidth of $FM1$ is plotted as a function of the microwave frequency ω for the three samples. The slope of the fitted lines gives the effective damping. The separation of the inhomogeneous part and the extraction of additional damping was carried out in the same manner as done in chapter 4. The linearity of linewidth vs. ω, a primary requisite for spin pumping, was verified for all the cases (not shown here).

We present our central result for this section in Figure 5.3. The spin current absorption property of four spin sink ($FM2$, AFM) overlayers are measured through the additional damping $\triangle\alpha = \frac{|\gamma|\hbar}{4\pi M_s t_{FM1}}\left(g_{eff}^{\uparrow\downarrow}/S\right)$ contributed to $FM1$ as a function of $t_{FM2,AFM}$. We find striking similarity in the spin current absorption property of these spin sinks. For the ferromagnets $CoFeB$, Py, and Co, $\triangle\alpha$ increases linearly as a function of t_{FM2} , rising to a maximum value and cutting off and quite sharply at a critical thickness $t = \lambda_C$, $\lambda_C = 1.2 \pm 0.1nm$. Above this critical thickness of t_{FM2}, $\triangle\alpha$ remains constant. The nature of the absorption curve for the antiferromagnet $IrMn$ is very similar to that

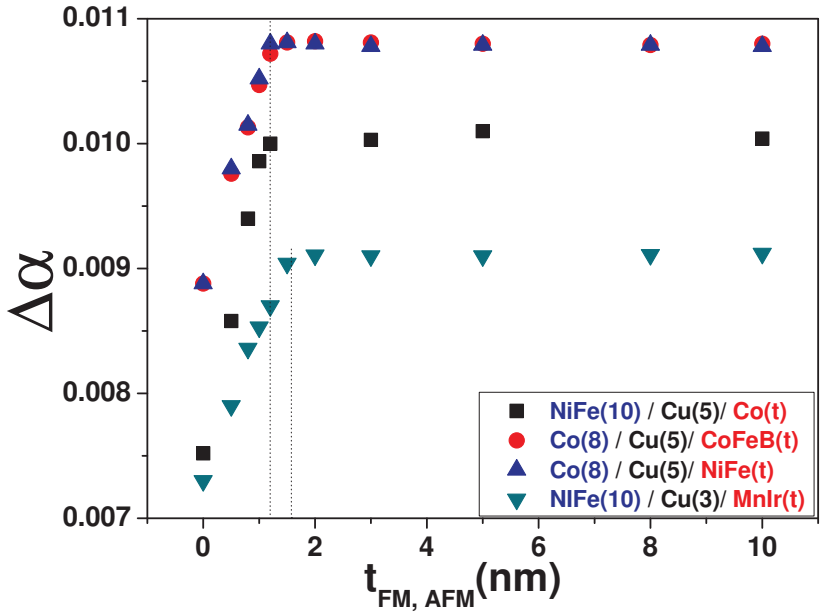

Figure 5.3: Gilbert relaxation rate - $FM1$ layer thickness product contributed by ultrathin ferromagnets $CoFeB$, Py, and Co and antiferromagnet $IrMn$ to to the $FM1$ layer resonance in $FM1/Cu(5nm)/FM2(t_{FM2})or AF(t_{AF})$. Saturation level converts to $\Delta\alpha = 1.9 \times 10^{-3}$ for $Co(8nm)$ ($\Delta H = 0.73Oe/Ghz$), $\Delta\alpha = 2.7 \times 10^{-3}$ for $Py(10nm)$ ($\Delta H = 1.1Oe/Ghz$).

of the ferromagnets but the critical length λ_C is found to be bit higher, about $1.7nm$. The three $FM2$ layers that we use for this study are structurally diverse, with FCC order for Py, mixed FCC/HCP for Co, and disorder likely for $CoFeB$. Nevertheless, the onset of spin current absorption is identically proportional to thickness in these layers, which highlights the correlated nature of transverse spin-current absorption, which is more of a dephasing mechanism and not material dependent, as predicted by theory. In prior works, a thickness-proportionality of transverse spin current rotation about the magnetization $\mathbf{m}$ in the hot-electron polarimetry measurements was observed in case of transmission [69] as well as in reflection [73]. Our observation shows linear convergence, as a function of t_{FM}, towards the saturation value of the spin mixing conductance $g^{\uparrow\downarrow}$. The net transverse spin current absorption does not result from a Poisson scattering process of uncorrelated spin-flip scatterers, but rather an angular average of continuous spin rotations for each electron wave vector in FM. Tight-binding calculations [76, 72] have predicted that point-defects (Fe in $Ni_{80}Fe_{20}$) are fully effective in suppressing oscillations predicted for Cu/Ni; a very similar t_F/λ_C to cutoff dependence is predicted with $\lambda_C \sim 0.7nm$ for (100) and $\sim 1.1nm$ for (111) structures [72]; the latter is close to our result for the FM layers. The longer value of λ_C found for the bulk antiferromagnet is

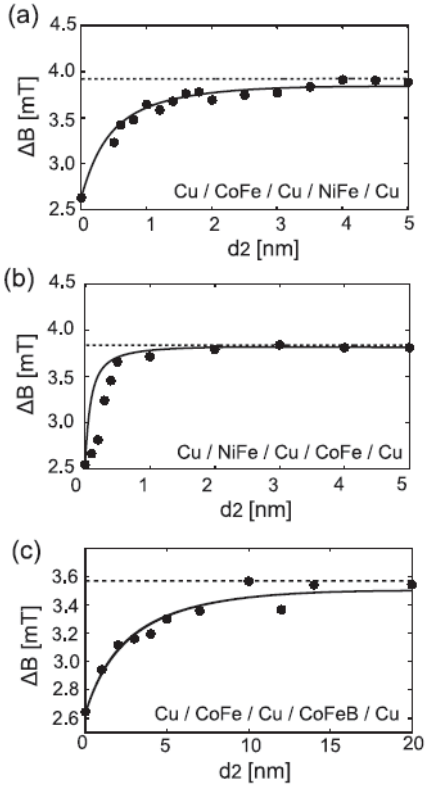

Figure 5.4: The FM_2 thickness dependence of the line width of the FMR power absorption spectra for $FM1/Cu/FM2$ structure, as observed by Taniguchi et al. [34]. Materials of the FM_2 layer are (a) $Ni_{80}Fe_{20}$, (b) $Co_{75}Fe_{25}$ and (c) $Co_{40}Fe_{40}B_{20}$, respectively.

consistent with weakened exchange; IrMn is nearer its Curie point of $\sim 400°C$.

Prior work, by Taniguchi et al. [34], who have made the observation of spin current absorption in three different ferromagnets: $NiFe$, $CoFe$ and $CoFeB$, is shown in Figure 5.4 for comparative understanding. We find our measurements are inconsistent with their experimental reports of an exponential onset of spin current absorption in these $FM2$ layers. These results differ significantly to the predicted theory of algebraic functional form of spin current decay in ferromagnets. Moreover, the characteristic lengths for spin current absorption for these ferromagnets, as found by them were: $3.7\,nm$ for $NiFe$, $2.5\,nm$ for $CoFe$ and $12\,nm$ for $CoFeB$, which are much higher than what we have found and the predicted scale of spin dephasing lengths.

5.3 Spin injection in FM1(t)/ Cu/ NM(t) structures

We extend our study of spin current injection as we move on from using ferromagnets and antiferromagnet as spin sinks to nonmagnetic or paramagnetic spin sink. The mechanism of spin current absorption by paramagnets are assumed to be distinctly different compared to that of ferromagnets and the antiferromagnet. In the introduction of this chapter this mechanism was discussed. For this study, the paramagnets chosen were

Pt, Pd and Ru, which was done based on their relatively short spin diffusion lengths as reported from studies in ref. [42]. We note that there are some key factors which differentiate a good spin sink from a poor one. It is found that a normal metal, which has a high spin-flip probability is good spin sink. Lighter metals such as Cu, Al, Cr and heavier metals such as Au, Ag, which have s-electrons in their conduction band are poor spin sinks. These metals have fairly small spin orbit coupling typically corresponding to $\epsilon \leq 10^{-2}$[77, 74], where ϵ is the ratio of momentum to spin flip flip scattering time $\epsilon = \frac{\tau}{\tau_{sf}}$, which is an important parameter in this regard. On the other hand, the heavier elements (atomic number Z) with p or d electrons in their conduction band, are very good or nearly perfect spin sinks since they have $\epsilon \geq 10^{-1}$[77]. However there are cases where the value of ϵ doesn't explain everything. We will find this out in the discussion at the end of section 4 in this chapter.

The other aspect of using these materials is that they are often used in spintronics devices, and in terms of spin polarized current transport studies, these are very well studied materials. Spin polarized current transport in these materials are known to be diffusive in nature, meaning, the injected spin accumulation (imbalance of spin up and spin down electron population) is diffused over the length scale corresponding to their spin diffusion length. Therefore, it is very interesting to study the spin current transport in these materials and compare that with existing and well established methods[42].

We will consider two types of heterostructures for this study; (1) In which a $3nm$ Cu spacer will be used to separate the paramagnetic spin sink layers from the ferromagnet, will be discussed in this section, and (2) the paramagnetic spin sink layers will be directly in contact with the ferromagnet, which will be discussed in the next section. The idea behind using these two types of heterostructures is that, inserting the nonmagnetic Cu in between the ferromagnet and the paramagnets, introduces an additional interfacial conductance ($g^{\uparrow\downarrow}_{Cu/NM}$) which adds in parallel with the other interfacial terms, reducing the effective value. Note that paramagnets like Pt, Pd are known to induce some perpendicular anisotropy when they are in direct contact with the ferromagnet (Co/Pt are very well known for this). Also in case of direct contact with a ferromagnet, magnetic moments could be induced in these paramagnets (This will be discussed in the next chapter in greater detail)[78]. These studies, with both the indirect ($FM/Cu/NM$) and direct contact (FM/NM) heterostructures, brings open questions which requires a rigorous study of the transport (emphasized on decay) of transverse component of pure spin current in these paramagnets.

Spin current absorption for heterostructures of the form $FM/Cu/[Pt, Pd, Ru]$ is presented in this section. For the details of the full sample structures, we refer to Table

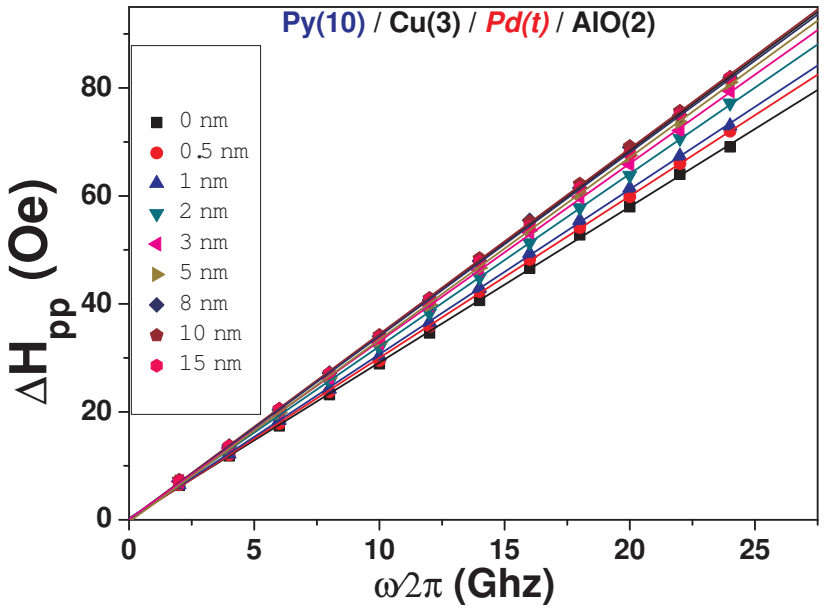

Figure 5.5: Frequency-dependent peak-to-peak FMR linewidth $\triangle H_{pp}(\omega)$ for $Ni_{81}Fe_{19}\,(10nm)$, plotted as a function of ω, for various thicknesses of spin sink Pd overlayer.

1 of chapter 3. The extraction of additional damping $\triangle\alpha$ and data analysis method is the same as presented in the last section. In Figure 5.5, the frequency ω dependent peak-to-peak FMR linewidth $\triangle H_{pp}(\omega)$ for $NiFe\,(10nm)$ for various thicknesses of a Pd overlayer, in $NiFe(10)/Cu(3)/Pd(t)$ heterostructures, is shown as a sample data. It is clearly visible that as the thickness of the Pd layer increases the slope of the lines increases, and above a certain thickness (about $8nm$) the lines merge on top of each other. The linearity of the data confirms the additional damping is Gilbert type, which was verified for the other two paramagnetic spin sink metals Pt, Ru as well, but not shown here.

In Figure 5.6, the central result for this section is presented, where $\triangle\alpha$, which is a measure of spin current absorption is plotted as a function of t_{NM}. The precessing ferromagnet is $10\,nm$ of $NiFe$ and the NM overlayers are Pt, Pd, and Ru. We find that the absorption characteristics for these materials are very different in nature compared to that of the ferromagnets and antiferromagnet as seen in the last section. These paramagnetic layers show an exponential depth dependence of spin current absorption, similar to that observed by others [68, 79] as $1 - \exp(-2t/\lambda_C)$; λ_C is a characteristic length for spin relaxation in the NM. We also observe two distinct features of these absorption characteristics; (a) the depth (threshold) inside the paramagnets, where the spin current absorption reaches maximum, are different for different NMs, and (b) the level of absorp-

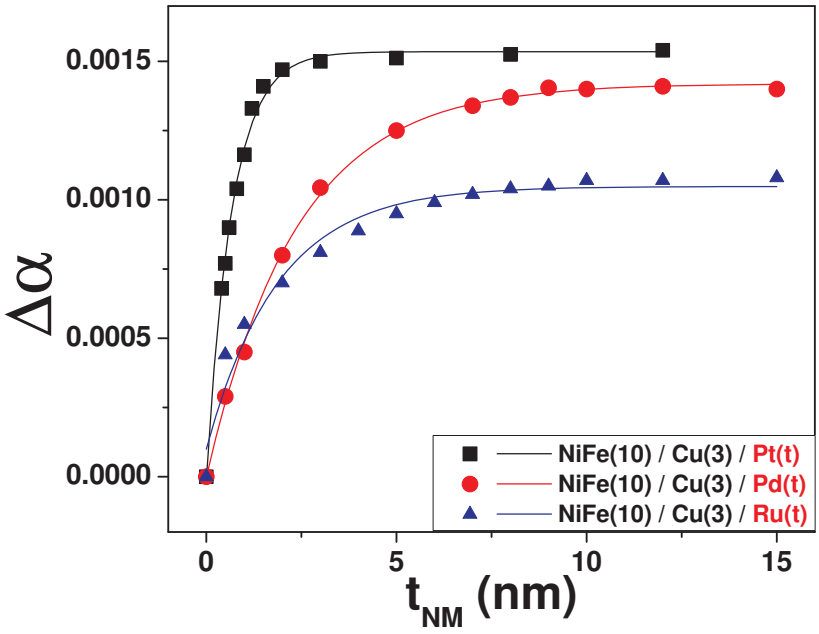

Figure 5.6: Additional damping $\triangle\alpha$ for 10 nm of $NiFe$, caused due to the nonmagnetic (paramagnetic) overlayers, plotted as a function of t_{NM}; $NM = Pt$, Pd, Ru.

Sample	$g_{eff}^{\uparrow\downarrow}/S$ (nm^{-2})	λ_C (nm)	$\triangle\alpha\vert_{NiFe\,10nm}$
$NiFe/Cu/Pt$	8.52	$\lambda_C^{Pt} = 1.38nm$	$\Delta\alpha^{Pt} = 0.00154$
$NiFe/Cu/Pd$	7.86	$\lambda_C^{Pd} = 4.7nm$	$\Delta\alpha^{Pd} = 0.00142$
$NiFe/Cu/Ru$	6.5	$\lambda_C^{Ru} = 4.4nm$	$\Delta\alpha^{Ru} = 0.00113$

Table 5.1: Effective spin mixing conductance $g_{eff}^{\uparrow\downarrow}/S$ for $NiFe(10n)/Cu(3)/PM(t)$ structures are given in column 2. In column 3 the characteristic length λ_C as extracted for different NM. In column 4, the maximum additional damping contributed by the NM overlayers are listed.

tion maximum or the absorption saturation is also different for different NMs used. Our data is fitted with: $\triangle\alpha = \frac{|\gamma|\hbar}{4\pi M_s t_{FM}} \left(g_{eff}^{\uparrow\downarrow}/S\right)(1-\exp(-2t_{NM}/\lambda_C))$, where M_S is the bulk saturation magnetization used from our previous measurements and $g_{eff}^{\uparrow\downarrow}/S$ is the effective spin mixing conductance parameter for the whole structure. λ_C is the characteristic length for the NMs which determines the depth in the NMs where the threshold of absorption maximum (saturation level of absorption) is reached. A factor 2 in the exponent is considered to take care of the effective thickness that the spin current traverses in the nonmagnet before returning back to FM. Parameters like the characteristic lengths λ_C, effective spin mixing conductance $g_{eff}^{\uparrow\downarrow}/S$, which are extracted from the fits are tabulated in Table 1.

Explanations for different penetration depths for spin current in these paramagnets, were sought based on their spin diffusion lengths. Unlike the spin dephasing in ferro-

Metal	T (K)	Technique	l_{sf}^{N} (nm)	ρ_0; $\rho(T)$(nΩ m)	ρl_{sf}^{N}(fΩ m^2)
Pd	4.2	CPP-S/SV	25^{+10}_{-5}	40	1
Ru	4.2	CPP-S/SV	~14	95	1.3
Pt	4.2	CPP-S/SV	14 + 6	42	0.6

Table 5.2: Spin diffusion length λ_{sdl} for nominally pure nonmagnetic Pt, Pd, Ru, as found in Table 2 of ref. [42].

magnets, the spin current absorption process in these paramagnets are govern by spin flipping mechanism. The paramagnets, which have a short spin diffusion length λ_{sdl}, absorb the spin currents within a very short depth as the injected spin relaxes immediately very close to the interface. Those with longer spin diffusion length λ_{sdl}, the spin currents traverses some length in the paramagnets before being completely absorbed. Our extracted values of the characteristic length λ_C for these paramagnets are much shorter compared to their bulk spin diffusion lengths as listed in Table 5.2 below (from ref. [42]). However we find from previous experimental studies, very similar characteristic lengths for Pt, was observed by Mizukami et al, using $Cu/NiFe\,(3nm)/Cu\,(10nm)/Pt(t)/Cu$ heterostructures [38], and for Pd; Foros et al. [68] have observed this characteristics length about $9nm$, using epitaxial $Pd(t)/(001)Fe(16ML)$ films. In both these cases the absorption characteristic (see Figure 5.8(a), (b)) is very similar to what we observe. The consistency in the observation of much shorter characteristic lengths for spin current absorption λ_C for the paramagnets under consideration, compared to their respective spin diffusion lengths, reveals that there is a possible ground to re consider the absorption mechanism for the transverse component of pure spin current in these paramagnets.

The explanations for the variations in the saturation value of $\triangle\alpha$ for the three NM layer coverages can be interpreted through different interface conductances $g_{Cu/NM}/S$ for the three Cu/NM interfaces[58]. These parameters govern the spin injection into NM through the Cu/NM interface. We will also have a discussion and comparison on these issues at the end of section 4.

5.4 Spin injection in FM1(t)/ NM(t) structures

In this section our depth dependance spin current study is performed in heterostructures, where the paramagnetic spin sink layers are in direct contact with the precessing ferromagnet. In Figure 5.7, we have plotted $\triangle\alpha$ as a function of paramagnetic coverage (t_{PM}), for the two paramagnets Pt and Pd. For a better understanding and comparison, we have added data from the last section as well. In the plot, black squares present the data for structures with Cu spacer i.e. for $(Ni_{81}Fe_{19}/\,Cu/\,Pt\,or\,Pd)$, and the red circles present data for structures without the Cu spacer, i.e. for $(Ni_{81}Fe_{19}/\,Pt\,or\,Pd)$.

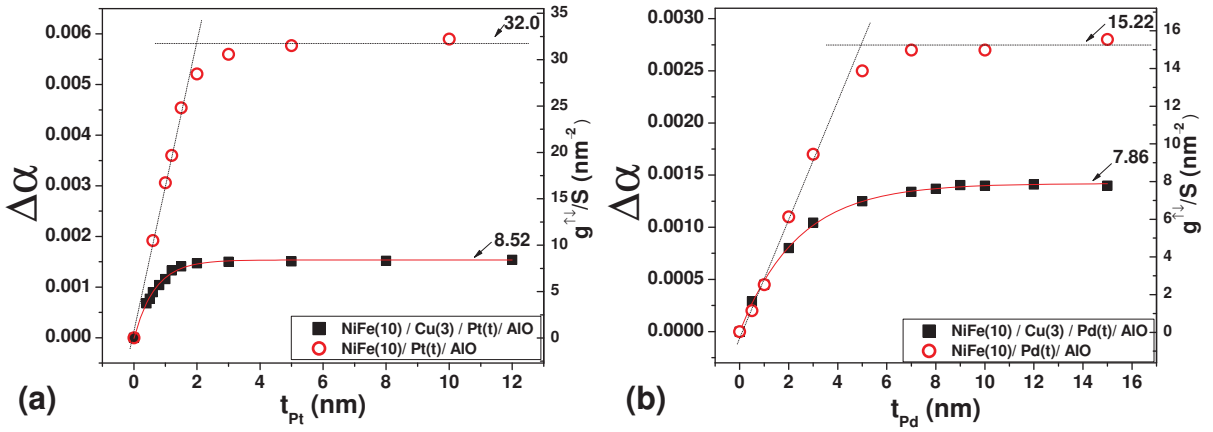

Figure 5.7: $\triangle\alpha$ for $10\,nm$ of $NiFe$ as a function of t_{PM} for (a) Pt, (b) Pd. Red circled represents the data for structures where Pt or Pd are in direct contact to $NiFe$, and black squares represents where $3\,nm$ of Cu spacer separates $NiFe$ from Pt or Pd.

Two features are common to both Pt and Pd layers, shown in Figure 5.7(a) and (b), respectively. First, the thickness dependence of the damping enhancement $\triangle\alpha(t_{NM})$ is little different for Pt and Pd, when they are in direct contact with $NiFe$ (we will refer to them as direct contact layers), compared to when they are separated from $NiFe$ by with $Cu(3nm)$ (we will refer to them as indirect contact layers). Direct contact Pt, Pd layers, exhibit a broad range of *linear* increase in $\Delta\alpha$, up to a cutoff thickness $t_c^{Pt}\sim 2nm$ for Pt and $t_c^{Pd}\sim 4.5nm$ for Pd, fitted well by $\triangle\alpha(t_N)\simeq\triangle\alpha_{max}t_N/t_c$. Whereas the indirect contact layers, exhibit an *exponential* approach to saturation, fitted well as $\triangle\alpha = \triangle\alpha_{max}(1-\exp -2t_{NM}/\lambda_\alpha)$, as discussed in the last section.

Second, for both Pt and Pd, the saturation level $\triangle\alpha_{max}$ is significantly higher for the direct contact case, compared with indirect contact case. For Pt (Figure 5.7(a)), the difference in saturation level is roughly a factor of four: $\triangle\alpha_{max} = 1.5\times 10^{-3}$ for indirect contact samples and 5.8×10^{-3} for direct contact samples. For Pd (Figure 5.7(b)), the levels are $\triangle\alpha_{max} = 1.4\times 10^{-3}$ and 2.7×10^{-3}, respectively. The direct and indirect contact layers have $\triangle\alpha(t_{NM})$ tangent at the origin for Pd, but for Pt, the increase in damping is more rapid near $t_{Pt}=0$, i.e. in the regime of direct exchange coupling with $NiFe$.

First, we consider the data in terms of spin pumping with diffusive transport in the paramagnets. This model was first identified in ref. [21, 22], and applied very recently to inverse spin Hall data for $Ni_{81}Fe_{19}/Pt$ [23], for thick Pt layers, $t_{Pt}\geq 10nm$. Here the (exponential) characteristic length for spin current absorption λ_C is the spin diffusion length λ_{sdl}, which by definition exceeds the electronic mean free path λ_M. We find that this model is not applicable given our measured resistivity for Pd and Pt of

$\rho_{Pd} = 18\mu\Omega cm$, $\rho_{Pd} = 20\mu\Omega cm$ [1]. The tabulated (see Table 2. of ref. [42]) resistivity-mean-free-path products $\rho{\cdot}\lambda_M$ for Pt, Pd layers of 200 $\mu\Omega{\cdot}cm{\cdot}nm$ imply $\lambda_M{\sim}10nm$. This exceeds λ_α for Pt and Pd of $0.67nm$ and $2.3nm$, when extracted using the model described above. This inequality was first pointed out in [68] for Pd but is more pronounced in Pt.

For the direct contact structures, $Ni_{81}Fe_{19}/NM(t_{NM})$, shown in Figure 5.7(a) for $NM = Pt$, and in Figure 5.7(a) for $NM = Pd$, the damping enhancement $\triangle\alpha$ is proportional to thickness t_{NM} over a broad range up to cutoff thickness t_c, after which it remains constant. The linearity is accurate to $\Delta\alpha{\sim}70 - 80\%$ of saturation. This dependence is characteristic of pumped spin current into ferromagnetic layers, as seen for several $FM1/Cu(5nm)/FM2(t)$ structures in the second section of this chapter, ref [33]. We fit the data to $\triangle\alpha(t_{NM}) = \triangle\alpha_{max}t_{NM}/t_c$, finding $t_c(Pd) = 4.5\,nm$ and $t_c(Pt) = 1.9\,nm$. Using the maximum value of $\triangle\alpha$,which is $\triangle\alpha_{max}$, we have extracted the effective spin mixing conductances per interfacial area for these structures as: $\frac{g^{\uparrow\downarrow}_{NiFe/Pt}}{S} = 32.0\,nm^{-2}$, $\frac{g^{\uparrow\downarrow}_{NiFe/Pd}}{S} = 15.22\,nm^{-2}$. These data, of effective spin mixing conductance, show a good agreement with ref. [64, 37]. In order to understand the difference we have sought arguments based on atomic number of Pt and Pd. We find that the atomic number Z of Pt is 78 and its electronic configuration is : $[Xe]\,6s1\,4f14\,5d9$. For Pd, the atomic number is $Z = 46$ and the electron configuration is : $[Kr]\,5s1\,4d9$. For both Pt and Pd, the conduction band is hybridized with d orbitals, which makes them good spin sinks. But since the atomic number of Pt is much higher (almost double) than that of Pd, the damping saturation $\triangle\alpha_0$ caused by Pt is also much higher than Pd, for the direct contact samples[22]. Based on this argument we see that $\frac{g^{\uparrow\downarrow}_{NiFe/Pt}}{g^{\uparrow\downarrow}_{NiFe/Pd}} \sim 2.1$, and $\frac{Z_{Pt}}{Z_{Pt}} \sim 1.7$. This is a very intuitive way of understanding the differences in the interfacial spin mixing conductances.

Comparison with prior works and discussion

We compare our spin current absorption characteristics in paramagnets with few prior works. In Figure 5.8(a) we present Mizukami's study of $NiFe\,(3\,nm)$ linewidth variation as a function of Pt overlayer thickness in sputter deposited $Cu/NiFe(3nm)/Cu(10nm)/Pt(d)/Cu$ films [38] . FMR measurements were carried on using a X-band ($9.77GHz$) ESR spectrometer and a **TE** 102 cavity. The observation they made regarding the effect of Pt layer thickness is very similar to our study that is presented in Figure 5.5. In both these cases spin sink Pt is separated from the ferromagnet by a Cu spacer (in our case $3nm$, and in Mizukami's case $10nm$). We note that the length scale at which the damping (linewidth) reaches its saturation is very similar to what we observe in our study. The

[1] The resistivity was measured using four probe method, at room temperature.

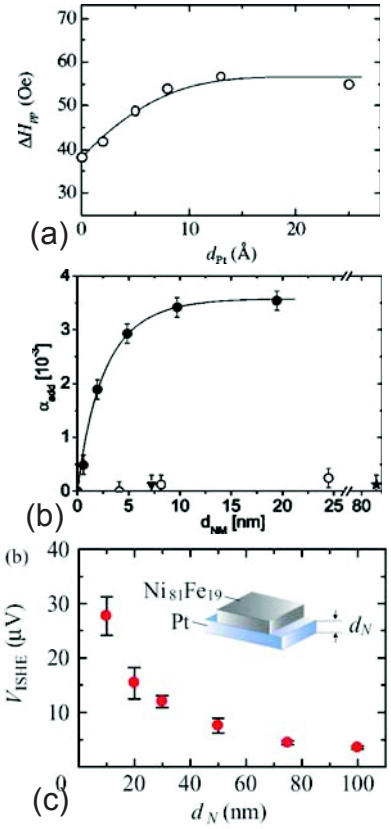

Figure 5.8: (a) $\triangle H_{pp}$ as a function of Pt layer thickness (in figure shown in $\mathring{A}$ units) for$Cu/NiFe(3nm)/Cu(10nm)/Pt(d)/Cu$ films as measured by Mizukami et al. [38]. (b) Additional damping contributed by Pd layer, in $Pd(t)/Fe(16ML)$ heterostructures, plotted as a function of Pd layer thickness, as measured by Foros et. al. [68]. (c) Inverse Spin Hall Voltage (V_{ISHE}) measured as a function of Pt layer thickness for $Pt(d)/NiFe(10nm)$ heterostructures, as observed by Nakayama et. al. [23].

percentage change in linewidth in their observation was found 50% for $3\,nm$ of $NiFe$ and in our case this percentage change was 20% for $10\,nm$ $NiFe$ layer. Normalizing for the thickness of the $NiFe$ layer we find our observation (200% per nm of $NiFe$) is in relatively good agreement with Mizukami's one (150% per nm).

In a different work presented by Foros et al. (Figure 5.8(b)) on MBE grown $Pd(t)/(001)Fe(16ML$ heterostructures on $GaAs(001)$ substrates, FMR measurement at 24 and $36\,GHz$ show similar additional damping caused due to Pd layer as observed by us (presented in Figure 5.6(b)) [68]. In both these cases the spin sink Pd layer is directly in contact with the ferromagnet (Fe for Foros et al. and $NiFe$ for us). They have estimated the characteristic length for spin current absorption in Pd about $9nm$, which is about the double to what we estimate.

Figure 5.8(c) is more recent, inverse spin Hall effect (ISHE) study for $NiFe/Pt$ structures[23]. Spin accumulation is created in Pt using spin pumping via precession of $NiFe$. This spin accumulation creates a flow of charge and creates voltage drop across Pt, which is measurable. In Figure 5.8(c) we show this inverse spin Hall voltage V_{ISHE}, measured across Pt layer, as a function of Pt layer thickness. The variation in V_{ISHE} as a function of Pt layer thickness is an exponential characteristic, from which characteristic length (spin diffusion length, as this corresponds to charge current) for Pt was extracted as $9nm$[23]. These comparisons hints at possibly different length scales for pure spin current absorption and charge current (or spin polarized charge currents) absorption in these strong spin-orbit materials like Pt, Pd.

5.5 Impact of interface resistance in spin pumping

In this section we present our study on the effect of interfacial resistance coming from nonmagnetic metals which are not spin sinks. Materials like Cu, Al are known as poor spin sinks. We create a magnetic heterostructures in which the spacer layer, separating the spin sink Pt from $NiFe$, is Cu plus Al. When pumped out spin current flows from Cu to Al, it faces an interfacial resistance (for spin). As none of Cu, and Al are spin sinks, this study provides a means to study this interfacial resistance.

For the samples, we have chosen $NiFe\,8nm$ as the precessing ferromagnet and $Pt\,3nm$ as spin sink, capped with $2nm$ of AlO. The spacer layer between $NiFe$ and Pt, which is of our primary interest, is a Cu/Al multilayer of the form $[Cu\,(6/n)\,nm/Al\,(6/n)\,nm]n$, where $n = 1, 2, 3, 4, 6$. The total thickness of the spacer $(Cu + Al)$ is chosen to be $12\,nm$, which was kept constant. Our observable parameter is the damping parameter α of $NiFe\,8nm$ as a function of the number n of Cu/Al interfaces, as shown in Figure 5.9. We observe that the damping for structures with Pt spin sink layer (red circles),

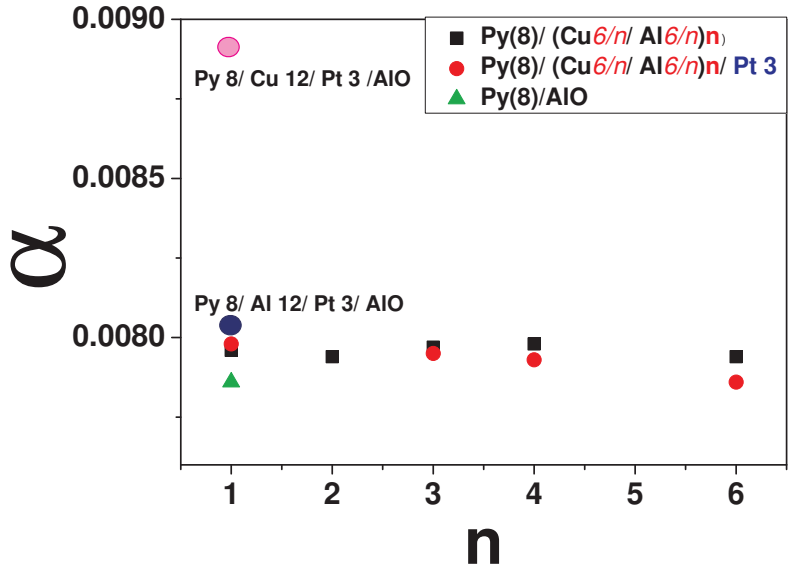

Figure 5.9: Effect of interfacial resistance, coming from Cu/Al spacer layer, in damping of FM layer in $FM\,8nm/[Cu\,(6/n)\,nm/Al\,(6/n)\,nm]n/Pt\,3nm$ heterostructures.

and without Pt spin sink layer(black squares), do not differ much. Moreover, no clear (striking) variation of α as a function of n was observed, and it is found to be very much constant throughout the span of n.

Comparing the damping α for the structures with $12nm$ of Cu (only) spacer, and $12nm$ of Al (only) spacer, we find for the Cu case, α for $NiFe$ is much higher than for the case of Al. This indicates that Al is blocking the spin current to pass through it, in other words it is more resistive to spin currents and prevents spin current from reaching the Pt overlayer. This causes less loss of spin current (the blue circle and the green triangle is very close), hence less damping contributed. We conclude form these measurements that bulk Al offers a lot of resistance for the spin current flowing through it. Therefore even if the Cu/Al interfacial resistance exists, it is dominated by Aluminum's bulk resistive effect.

5.6 Spin current reflection form NM1/NM2 interfaces

We have observed in Figure 5.6, that different NM layers (Pt, Pd, Ru), even when not in direct contact with $NiFe$, but separated by Cu, causes different damping saturation maxima $\triangle\alpha_{max}$. We have interpreted this differences on the basis of different interface conductances $g_{Cu/PM}/S$ for spin current for different Cu/NM interfaces. In order to quantitatively study the spin current back flow from bulk $NM1$, or reflection from the $NM1/NM2$ interface, in these $FM/NM1/NM2$ heterostructures, we are pre-

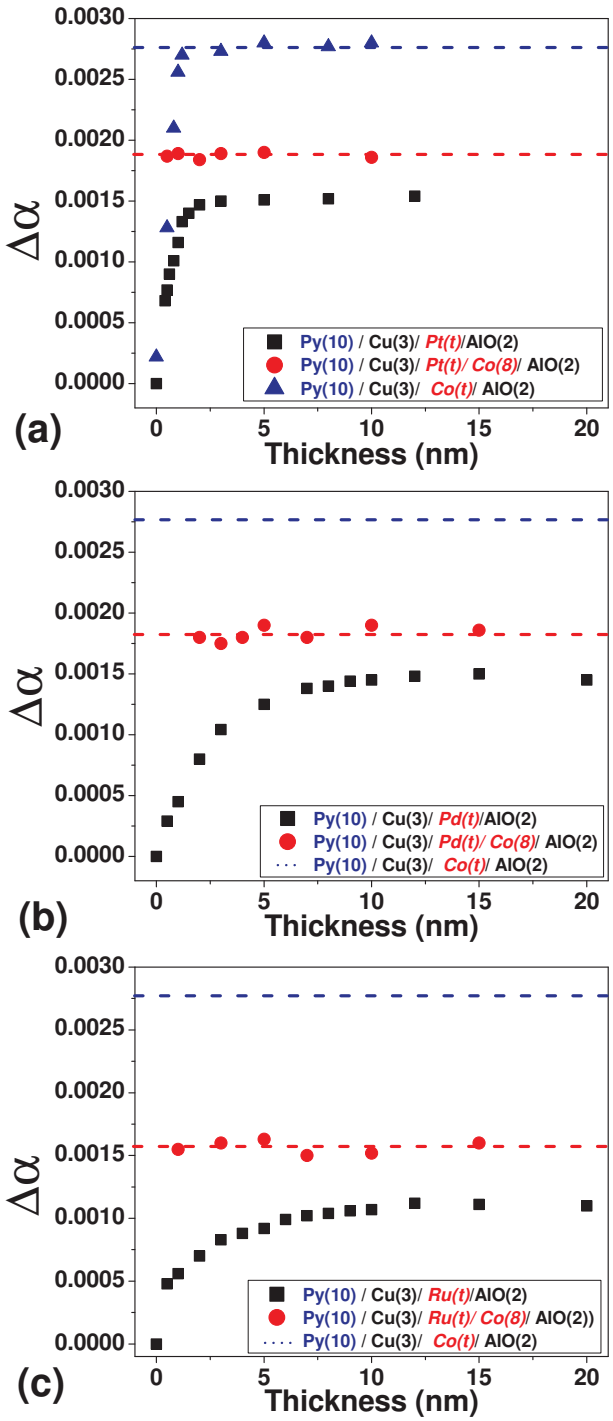

Figure 5.10: Qualitative study of spin current back flow from bulk $NM1$, or reflection from $NM1/NM2$ interface, in a $FM/NM1/NM2$ heterostructures.

senting a series of measurements, which we have termed as reflection measurement. In Figure 5.10(a) the blue triangle represents the absorption characteristics obtained for $NiFe\,(10nm)/Cu\,(5nm/Co(t)$, which shows larger $\triangle\alpha_{max}$ compared to the paramagnetic spin sink of indirect contact cases. Therefore we have decided to use $Co(8nm)$ on top of the paramagnets i.e. the heterostructures for this series of measurements are of the form $Ni_{81}Fe_{19}\,(10nm)/\,Cu(3nm)/\,NM(t)/Co(8)$. We have expected that $\triangle\alpha = \triangle\alpha_{max}$, for this series would be flat, and the value of $\triangle\alpha_{max}$ will be very much the same as without the $Co(8)$ layer.

In Figure 5.10, this study of ours is presented for three $NM2$ layer types. The flatness of the absorption characteristics is observed which reveals that whatever spin current is penetrated through the $NM2$, is absorbed by $Co(8)$ layer. We find, $\triangle\alpha_{max}$ is not the same, for the same NM layer type, with and without the $Co(8)$ layer, as a shift is identified. This shift was noticed for all three studies (Figure 5.10(a), (b), (c)). We do not have a very good understanding for this shift of $\triangle\alpha_{max}$, when the top $Co(8)$ layer is added. We seek interpretation for this using our XMCD measurement (presented in the next chapter). It is observed that there is surprisingly a large interfacial moment in Cu/Pd, and Cu/Pt. This suggests an interfacial susceptibility very much larger than the bulk and we think that the major contribution to spin current scattering in the paramagnet is localized near the Cu interface and not in the bulk. The energy for the interfacial moment is very close to k_BT, however, so it should be subject to thermal fluctuations. Since its spin direction is not constant it could scatter spin current effectively, and with the very short characteristic length we see. The saturation level of damping enhancement does not correspond to a full randomization of spin current inside of the NM layer. Rather, it corresponds to a maximum effect of this interfacial spin fluctuation, the magnitude for which does not need to be the same for Cu/Pt, Cu/Pd, and Cu/Ru. We had interpreted this variation of the saturation level as a finite conductance at the Cu/NM interface, but we haven't been able to validate that with a known interfacial resistance in the absence of spin fluctuations.

5.7 Summary

The central motivation of this chapter was to characterize the spin current absorption length (spin dephasing) in different ferromagnetic and paramagnetic spin sink layers. The observed spin current absorption length and algebraic form of decay in ferromagnets were in accordance with the theoretical predictions. We find, the onset of spin current absorption is identically proportional to thickness in these layers, which highlights the correlated nature of transverse spin-current absorption, which is more of a dephasing

mechanism and not strongly material dependent. The dephasing length found for three structurally distinct ferromagnets ($NiFe$, $CoFeB$, Co) is $\lambda_C = 1.2 \pm 0.1\, nm$. Moreover, the algebraic functional form of this type of decay was verified in all these cases. The same length for the antiferromagnet $IrMn$ is found to be slightly higher $\lambda_C \sim 1.7\, nm$, interpreted based on weakened exchange coupling.

The spin current absorption length for the paramagnetic Pt, Pd, Ru was found to be much shorter than their respective spin diffusion lengths. The comparison with some of the prior work based on nonlocal damping measurement (related to transverse component of spin current), in this regard, shows similar shorter length scales. These studies (comparisons) provide a basis to think about considering slight modifications or incorporating certain assumptions in the spin pumping model, for the heavy spin orbit metals like Pt, Pd. Note that, for the case of inverse spin Hall effect [23], spin pumping created spin accumulation induces charge flow in Pt, which leads to V_{ISHE} across Pt. The length scale observed in this measurement is much higher compared to our results. The similar length scale was observed in the direct contact cases as well. We believe this is due to the fact that in these measurements, the characteristics for charge current are measured while we are dealing with pure spin current. A possible explanation for these could be that the longitudinal relaxation time T_1 for spins current in these heavy spin orbit materials like Pt, Pd is greater than the transverse spin relaxation time T_2 (BB formalism), i.e. $T_1 > T_2$. Even though for normal metals it is known that $T_1 = T_2$, a more detailed study on this topic is required.

The studies for the interface resistance effect in damping with Cu/Al multilayer structure, does not show a clear indication of the impact of interfacial resistance effect on damping. We believe the choice of Al was perhaps not the best, as it provides lot of bulk resistance when spin current traverses through it. Replacing Al by Au, might show some clear indication.

Chapter 6

Role of induced Pt and Pd moments in spin pumping

In the last two chapters, we have observed that the paramagnetic spin sink layers (Pd, Pt) caused significantly larger nonlocal damping to $NiFe$ layer, when they are in direct contact with $NiFe$ layer compared to when they are separated from $NiFe$ via a Cu spacer. Mainly two differences were noticed for this direct contact samples from that of the indirect contact ones. (1) The maximum value of additional damping $\triangle\alpha_{max}$ is much higher for the direct contact case, and (2) in the low t_{NM} regime, $\triangle\alpha$ has a linear onset for the direct contact samples, instead of an exponential increase, which is seen for the indirect contact ones. The arguments for the former case was sought based on the atomic number (Z) for Pd and Pt. However, the linear onset for the spin current absorption in Pd, Pt which are directly coupled to $NiFe$ cannot be understood using that argument. Therefore, it required us to investigate this problem using a different experimental means, which will be discussed in this chapter. We have performed X-ray magnetic circular dichroism (XMCD) measurement to show that, when Pt and Pd are in direct contact with $NiFe$, the formation of induced interfacial magnetic moments in these paramagnets, could cause spin scattering near the interface.

Direct exchange interactions from $3d$ ferromagnetic moments are known to induce sizable local moments on Pd atoms. Neutron diffraction [80] shows up to $0.4\mu_B$/Pd atom in Pd_3Fe. Pd moments of similar magnitude are also induced by direct exchange at interfaces with Fe in ultrathin Pd/Fe super-lattices[78]. However, indirect exchange interactions have not yet been shown to have an effect on the magnetism of Pd or Pt. These materials are among very few $3d$, $4d$, or $5d$ transition normal metals (or paramagnets) through which no oscillatory interlayer exchange coupling (IEC, or RKKY-like[81]) between adjacent ferromagnets (FM)[82] has been observed in a $FM/NM/FM$

structure[83]. The tendency towards ferromagnetic order in Pd and Pt might explain the absence of antiferromagnetic coupling in $FM/(Pd\,or\,Pt)/FM$ multilayer, but it might also seem to predict the possibility of ferromagnetic order induced through a $FM/NM/(Pd\,or\,Pt)$ structure. In this Chapter, we report evidence of direct and indirect static exchange coupling acting on Pd, Pt moments in $FM/[Cu/]Pd$ and $FM/[Cu/]Pt$ super-lattice using XMCD measurements. These XMCD measurements and the data analysis, were done by F. Wilhelm and A. Rogalev, at the European Synchrotron Radiation Facility (ESRF).

6.1 Experiment

Four multilayer structure; two for Pd and two for Pt, were prepared. Each multilayer was deposited with buffer layers of $Ta(5nm)/Cu(3nm)$ to promote fiber texture[84], and was capped with $Py(5nm)/Cu(3nm)/Ta(5nm)$. Each of the multilayer structures consisted of 20 repeats, as $substrate/seed/[repeat]_{20}/cap$. For the investigation of direct exchange with Pd and Pt , the *repeat* unit was $[Py(5nm)/Pd(2.5nm)]$ and $[Py(5nm)/Pt(1nm)]$. We will refer to this sample as "Py/Pd", and "Py/Pt". For the sample in which we investigate induced moments by indirect exchange with Pd and Pt, the repeat unit was $[Py(5nm)/Cu(3nm)/Pd(2.5nm)/Cu(3nm)]$ and $[Py(5nm)/Cu(3nm)/Pt(1nm)/Cu(3nm)]$. We will refer to this sample as "$Py/Cu/Pd$" and "$Py/Cu/Pt$". The total Pd thickness in each multilayer was thus $50nm$; each Pd layer consists of roughly 22 monolayers, assuming the bulk FCC lattice constant of $3.89\,\mathring{A}$. Whereas for Pt the total thickness in each multilayer was $20nm$, and in each of the Pt layers, about 4.5 monolayers was present, assuming the lattice constant of bulk FCC Pt as $3.92\,\mathring{A}$.

The L-edge XMCD for both Pd and Pt was measured at Beamline ID-12 at the European Synchrotron Radiation Facility (ESRF)[85]. The first harmonic of the helical undulator HELIOS II was used to provide circularly polarized X-rays in the energy range, between 3.15 and 3.37 keV for Pd, and between 11.52 and 13.37 keV for Pt. At these energies, the Bragg angle of the Si $\langle 111 \rangle$ double crystal monochromator is close to the Brewster angle of 45°, with a consequent reduction of the circular polarization rates from 97% to about 12.6% at the Pd L_3 edge (3165 eV) and 21.9% at the Pd L_2 edge (3323 eV). The samples were mounted in a vacuum chamber inserted between poles of an electromagnet generating a magnetic field of 0.6 T, and the chamber was kept at room temperature. The incident X-ray beam was parallel/antiparallel to the direction of applied magnetic field, while the angle of incidence at the sample was ∼15°. Our spectra were recorded in total fluorescence yield detection mode (TFY). XMCD signals were recorded by flipping the direction of magnetic field at each energy point of the

spectra. The XMCD spectra were measured for both the opposite (LCP, RCP) helicities of X-rays.

For quantitative analysis, the XMCD spectra were corrected for incomplete circular polarization and normalized, setting the x-ray absorption above the L_3 edge equal to unity and to 0.5 above the L_2 absorption edge. To derive the spin and orbital moments carried by the Pd $4d$ electrons, and Pt $5d$ the so-called magneto-optical sum rules were applied to the normalized XMCD spectra, using[53, 86]:

$$\langle S_z \rangle = \frac{3}{2}(A_3 - 2A_2)(n_{qd}/\sigma_{tot}) - \frac{7}{2}\langle T_z \rangle , \tag{6.1}$$

and

$$\langle L_z \rangle = 2(A_3 + A_2)(n_{qd}/\sigma_{tot}). \tag{6.2}$$

where A_2 and A_3 denotes the integrated XMCD intensities at the L_2 and L_3 edges, respectively. n_{qd} is the number of holes in the qd shell; $q = 3, 4, 5$. For Pd ($q = 4$), n_{4d} is the number of hole in $4d$ state , and for Pt ($q = 5$) n_{5d} is the number of hole in $5d$ bands. σ_{tot} is the total absorption cross-section corresponding to $2p \rightarrow 4d$(Pd), or $2p \rightarrow 5d$(Pt) transitions, and $\langle T_z \rangle$ is the expectation value of the spin magnetic dipole operator. In the analysis, the contribution of the spin magnetic dipole, $\langle T_z \rangle$, was neglected.

Estimation of number of holes:

The number of holes can be estimated following the well established procedure in ref.[78]. The normalized X-ray absorption cross-section per number of qd holes , n_{qd}/σ_{tot} , was determined, for Pd (see Figure 6.1(a)), by subtracting the $Ag\,([Kr]\,5s1\,4d10)$-foil $L_{2,3}$ spectra from the experimental Pd $L_{2,3}$ spectra measured on the *pure* Pd (not shown) and taking the theoretical value for the difference in the $4d$ holes equal to 0.92. For Pt (see Figure 6.1(b)), this was done by subtracting the $Au\,([Xe]\,4f14\,5d10\,6s1)$-foil $L_{2,3}$ spectra from the experimental Pt $L_{2,3}$ spectra measured on the *pure* Pt (not shown) and taking the theoretical value for the difference in the $5d$ holes equal to 1.018. The same procedure was applied to estimate the number of holes n_{qd} on Pd, Pt atoms in the multilayer structures.

6.2 Results

$L_{2,3}$-edge x-ray absorption near-edge structure (XANES) and x-ray magnetic circular dichroism (XMCD) spectra are shown in Figure 6.1(a) for Pd and in 6.1(b) for Pt. The XANES spectra for $Ag\,([Kr]\,5s1\,4d10)$ is also shown in Figure 6.1(a) for comparison with Pd, similarly XANES spectra for$Au\,([Xe]\,4f14\,5d10\,6s1)$ is shown in Figure 6.1(b) for comparison with Pt. Figure 6.1(a) show that at Pd L_3, L_2-edge (3173 eV and 3331 eV) the absorption for the Py/Pd sample (black lines) is higher compared to the $Py/Cu/Pd$

sample (red lines). This is attributed to a difference in the number of Pd $4d-$holes, as indicated in Table 6.1, larger in the case of Py/Pd. The difference can be attributed to charge transfer from the Cu layer into Pd, where sp electrons from Cu fill some of the $4d$ holes near the interface with Pd. According to the analysis described in the previous section, we estimate a difference in the number of Pd $4d-$holes as $n_{4d} = 1.36$ for the Py/Pd sample and $n_{4d} = 1.33$ for the $Py/Cu/Pd$ sample. The same is observed (see Figure 6.1(b)), at the L_3-edge (11572 eV) of Pt, when the XANES spectrum for the Py/Pt sample is compared to the $Py/Cu/Pt$. But not much difference, is observed for these two XANES spectra, at the Pt L_2-edge (13282 eV). For the case of Pt L_3-edge, the difference is attributed to a difference in the number of Pt $5d-$holes, indicated in Table 6.1, larger in the case of Py/Pt.

At the L_3 edge, typical negative magnetic circular dichroism (XMCD) spectra, at the L_2 edge, positive magnetic circular dichroism, for both Pd and Pt is clearly seen for the Py/Pd and Py/Pt multilayer. For Py/Pd, a maximum XMCD of $\sim -10\%$ at the L_3 edge and $\sim +8\%$ at L_2 and for Py/Pt a maximum XMCD of $\sim -7.2\%$ at the L_3 edge and $\sim +3.3\%$ at L_2 is observed. According to eqn. 6.1 and 6.2, the imbalance in integrated intensities at the $L_{2,3}$ edges indicates a nonzero orbital moment m_L/m_S.

In Figure 6.2 the XMCD spectra for the direct contact super-lattices are compared to the indirect contact super-lattices. In Figure 6.1, it is seen that the magnitude of XMCD spectra for the $Py/Cu/Pd$ and $Py/Cu/Pt$ multilayer structures are quite small, therefore they needed to be rescaled for a better comparison. This is done by multiplying the XMCD of $Py/Cu/Pd$ by a factor of 30 and that for $Py/Cu/Pt$ by a factor of 100, which are presented in Figure 6.2. As we compare the XMCD signals for the direct contact (black line) and indirect contact (red line) structures, we find that the XMCD signal is clearly present (Figure 6.2(a)) in the $Py/Cu/Pd$ super-lattice, roughly 3% in magnitude that observed for Pd in the Py/Pd super-lattice. It is also apparent in the spectra that the relative weights of the Pd L_3 XMCD is reduced and the Pd L_2 XMCD is increased, respectively, through addition of the $3nm$ Cu spacers. This reduces the asymmetries between the integrated intensities of $L_{2,3}$ edges, indicating a more nearly pure-spin type moment in Pd for the indirect exchange-coupled sample. However, the rescaled XMCD for $Py/Cu/Pt$, presented in Figure 6.2(b), shows a high noise level, and a clear conclusion can not be drawn from this figure.

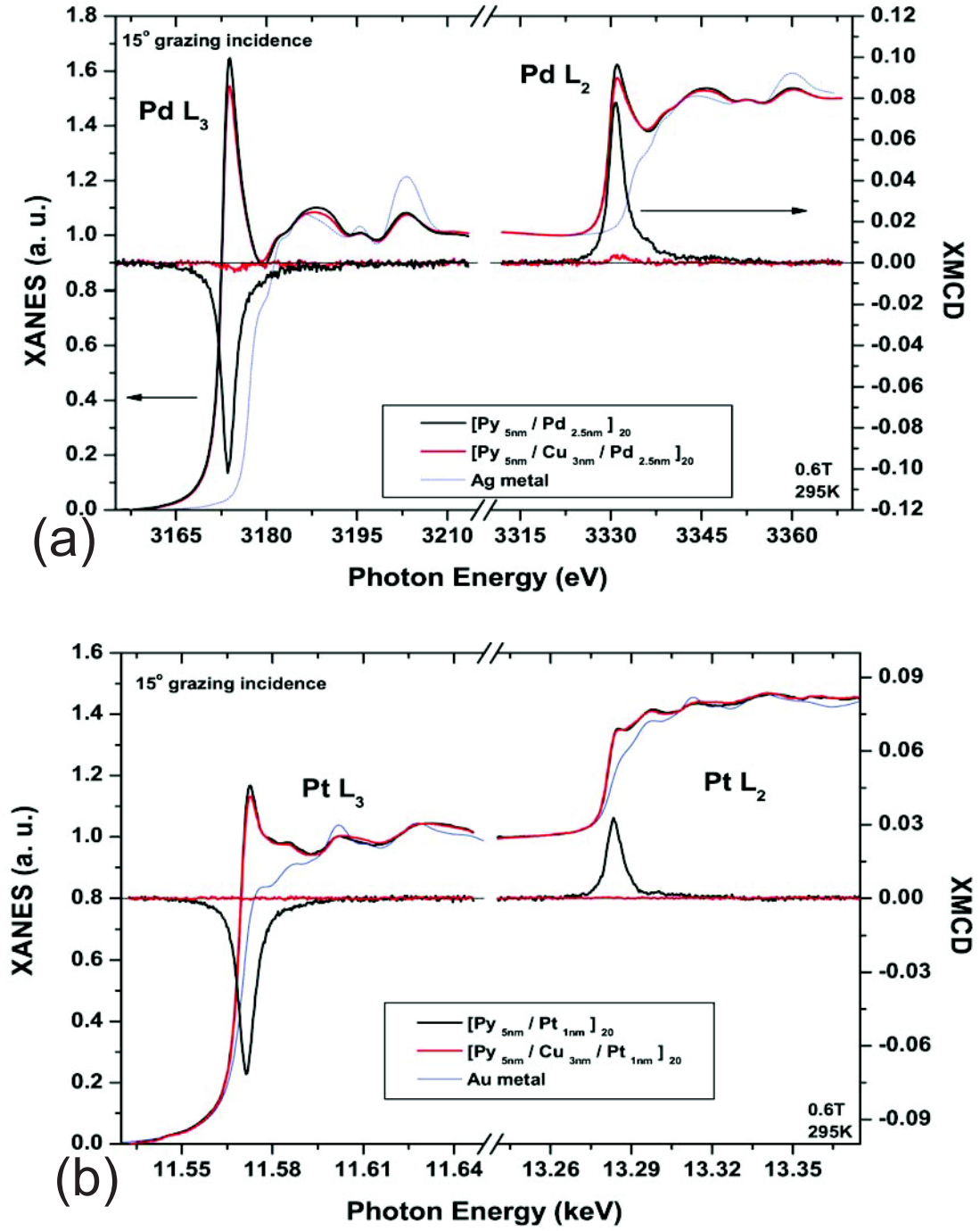

Figure 6.1: X-ray absorption near-edge structure (XANES) and x-ray magnetic circular dichroism (XMCD) for (a) direct exchange-coupled $[Py(5nm)/Pd(2.5nm)]_{20}$ and indirect exchange-coupled $[Py(5nm)/Cu(3nm)/Pd(2.5nm)/Cu(3nm)]_{20}$ with Ag XANES (b) direct exchange-coupled $[Py(5nm)/Pt(1nm)]_{20}$ and indirect exchange-coupled $[Py(5nm)/Cu(3nm)/Pt(1nm)/Cu(3nm)]_{20}$ samples, with Au XANES reference.

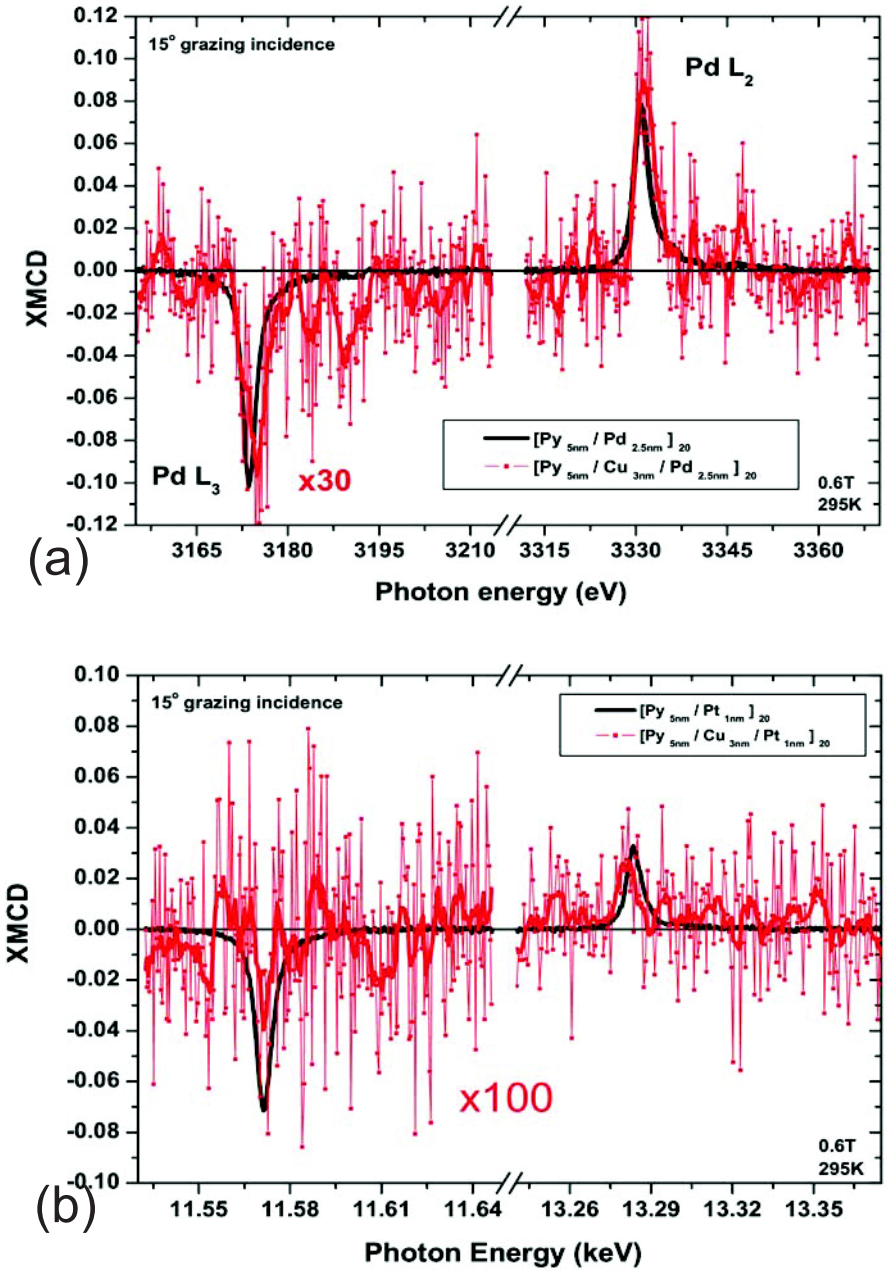

Figure 6.2: XMCD spectra for (a) direct exchange-coupled $[Py(5nm)/Pd(2.5nm)]_{20}$ and indirect exchange-coupled $[Py(5nm)/Cu(3nm)/Pd(2.5nm)/Cu(3nm)]_{20}$ samples (magnified by a factor of 30). (b) direct exchange-coupled $[Py(5nm)/Pt(1nm)]_{20}$ and indirect exchange-coupled $[Py(5nm)/Cu(3nm)/Pt(1nm)/Cu(3nm)]_{20}$ samples (magnified by a factor of 100).

Sample	$m_{NM}^{tot}(\mu_B/atom)$	m_L/m_S	$n_{h,4d}/at$
Py/Pd	$+0.116 \pm 0.0007$	0.0485 ± 0.002	1.36
Py/Cu/Pd	$+0.0037 \pm 0.0007$	$0.028 \pm 0.08*$	1.33
Py/Pt	$+0.27 \pm 0.007$	0.176 ± 0.014	–
Py/Cu/Pt	+0.001	–	–

Table 6.1: Pd-site total magnetic moments m^{tot}, ratio of orbital to spin moments m_L/m_S, and number of $d-$holes extracted from $Pd\ L-edge$ XMCD measurements.

Analysis:

As mentioned earlier, these analysis of the XMCD spectra were carried out by F. Wilhelm and A. Rogalev, at the ESRF. The extracted moments using intensity sum-rules are presented in Table 6.1. For the direct exchange coupled multilayer, the estimated orbital to spin moment ratio for Pd is found to be $m_L/m_S = 0.0485 \pm 0.002$ and for Pt: $m_L/m_S = 0.176 \pm 0.014$. For the indirect exchange coupled case the moment induced in Pd through Cu is weaker by a factor of 30, but clearly visible in the spectrum, which corresponds to an effective field acting on Pd of $\sim 2T$. Sum-rules analysis indicates that $m_L/m_S = 0.028$, with a reduced fraction of the moment coming from the orbital component. The greater spin-type component is consistent with RKKY-type exchange through Cu, which possesses induced spin moments with negligible orbital components[87], acting on Pd. Error bars are large on the estimate due to the small magnitude of the moment, but the relative increase of the L_2 dichroism for the indirect contact (exchange) sample is clear in Figure 6.2(a). However, poor signal to noise ratio makes this analysis impossible for the indirect contact Pt multilayer structure.

6.3 Discussion:

The XMCD measurements were performed, partly to support and provide more in-depth understanding of our spin pumping studies presented in Chapter 5. Therefore, we would like to re-address some of the issues that we have discussed in section 4 of Chapter 5. In nonlocal damping (spin-pumping) experiments, the thickness-dependent, spin sink induced damping enhancement $\Delta\alpha(t_{NM})$ is found to be linear with cutoff thickness t_c in direct-exchange coupled $Ni_{81}Fe_{19}\,(10nm)/\,[Pd,\,Pt](t)$, contrasting with the known exponential onset in indirect-exchange coupled $Ni_{81}Fe_{19}\,(10nm)/\,Cu(3nm)/\,[Pd,\,Pt](t)$. The linear depth dependence of damping, at lower thicknesses, for the Pt and Pd in direct contact samples is very similar to what was shown in section 3 and 4 of Chapter 5

Structure	$\lambda_J(nm)$	$A_{ex}(erg/cm^2)$
FM1/Cu/FM2	1.2	1250
Py/Pt(t)	1.9	177
Py/Pd(t)	4.8	457

Table 6.2: Interfacial exchange energy ΔA_{ex}, as calculated using the induced moment from XMCD measurement and the Stoner enhancement factor from ref [88].

(see Figure 5.7 in Chapter 5), for the ferromagnetic spin sink layers. Therefore for these direct contact samples, this linear depth dependence of damping, has been identified as a hallmark of spin-splitting in the spin sink layer near the interface in these paramagnets. For the spin current absorption in $FM1/Cu/FM2(t)$ structures (see section 2 in Chapter 5), we have suggested that the cutoff thickness λ_c for linear spin current absorption is on the order of $\lambda_J = hv_g/2\Delta_{ex}$, where v_g is the electronic group velocity at the Fermi level and Δ_{ex} is an exchange splitting energy. Electrons which enter the spin sink (Pt and Pd) at E_F do so at a distribution of angles with respect to the interface normal, traverse a distribution of path lengths, and precess by different angles (from minority to majority or vice verse) before being reflected back into the ferromagnet. For constant v_g, it is predicted that $\lambda_J \propto \Delta_{ex}^{-1}$, the exchange energy.

These paramagnetic (PM) layers Pt and Pd in direct exchange with $Ni_{81}Fe_{19}$ through the induced magnetic moment, we can estimate an interfacial exchange energy as: $\Delta A_{ex}(= \Delta_{ex} t_{PM})$. This interfacial exchange can be represented as $\Delta A_{ex} = M t_{PM}/2\mu_B N_0 F$, where$\mu_B$ is the Bohr magneton per atom, F is the Stoner enhancement factor, N_0 is the single-spin density of states, M is the magnetic moment averaged over the paramagnetic layer thickness t_{PM}. Note that, in ferromagnets the exchange splitting are assumed to be constant as a function of depth in the ferromagnet. This might probably be not true for the above mentioned paramagnetic cases, as most of the spin current absorption might be occurring close to the FM/PM interface. Therefore we assume the interfacial exchange ΔA_{ex} to be a reasonable representation of Δ_{ex} (bulk exchange) i.e. $\Delta A_{ex} \sim \Delta_{ex}$.

Taking parameters from the tables in [88], we calculate the interfacial exchange for a ferromagnetic case and the above mentioned bilayers of Py/Pt and Py/Pd. These calculated interfacial exchange energies are tabulated above. With the above mentioned approximation one can write $\lambda_J \propto \frac{1}{\Delta A_{ex}}$, which lead to $t_c \propto \frac{1}{\Delta A_{ex}}$. This relation shows very good agreement to our observation with Pt and Pd as we find (see section 4 of chapter 5): $\frac{t_c^{Pd}}{t_c^{Pt}} \sim \frac{\Delta A_{ex}^{Pt}}{\Delta A_{ex}^{Pd}} \sim \frac{5}{2}$. For a better understanding we plot t_c as a function of $\frac{1}{\Delta A_{ex}}$ for Pt, Pd and a typical ferromagnet as shown in Figure 6.3. We see that the obtained critical depths from spin pumping measurement are very much in agreement with calculated $\frac{1}{\Delta A_{ex}}$ using XMCD studies, as the three points falls on the same straight line which

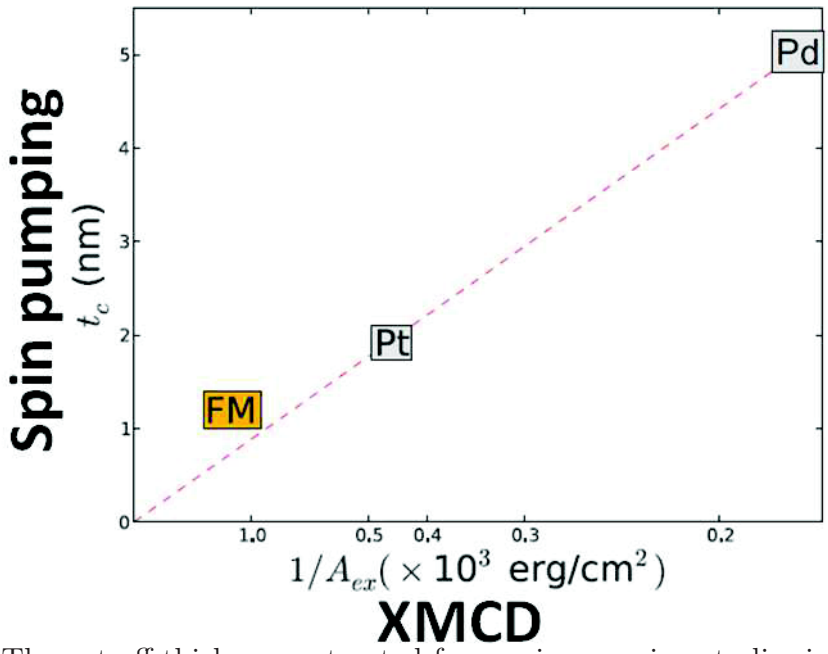

Figure 6.3: The cut off thickness extracted from spin pumping studies is correlated with the interfacial exchange energy calculated using XMCD study.

passes through zero. This tells us that for direct exchange contact samples (see Figure 5.7 in Chapter 5) the linear onset (like ferromagnet) for spin current absorption, could be caused by the induced moment in Pd, Pt (inducing some ferromagnetic character), in direct contact with $NiFe$.

Conclusion

Here we will summarize our major results, and pose open questions that came out from our study. First of all, we want to emphasize on the approach that we took compared to previous studies on spin pumping and damping enhancement in magnetic heterostructures. In particular we have adapted a common methodology for studying the nonlocal damping caused due to spin pumping. In a variety of magnetic and nonmagnetic materials, this is the first time the subtraction method is employed to extract nonlocal additional damping ($\Delta\alpha(t_{FM}) = \alpha_{SS}(t_{FM}) - \alpha_{no\,SS}(t_{FM})$) caused due to spin pumping effect. This method has enabled us to subtract out other contributions in damping in a magnetic heterostructure. For most of our studies (other than the direct contact samples) the ferromagnet under investigation (precessing layer) was always surrounded by Cu from both the sides, to avoid the effects of different interface, that makes the comparison much more easier and reliable.

In chapter 4, our main results include the verification of two predictions of spin pumping, which are (1) the additional damping $\triangle\alpha$ caused due to spin pumping is Gilbert type, which was verified by checking the linearity of $\Delta H_{pp}(\omega)$ as a function of ω, and (2) $\triangle\alpha$ is linearly dependent on the inverse of thickness of the precessing ferromagnetic layer, i.e. $\triangle\alpha \propto 1/t_{FM}$. Also for the first time we show that the damping for a ferromagnet is roughly independent of it's spin diffusion length. This argues against a proposed resistivity based mechanism for the observed nonlocal additional damping in magnetic heterostructures. From the spin pumping caused additional damping characterization, we have extracted interfacial spin mixing conductance parameters $\frac{g_{eff}^{\uparrow\downarrow}}{S}$, which play an important role in spin current transport. Using spin transfer torque (STT) method, these parameters are hard to characterize, but spin pumping offers a much easier means of characterization. As these two fundamental processes are reciprocal, the spin mixing conductance parameters are the same for STT and spin pumping. This makes, the characterization of these parameters, even more important. The main open question that remains in the study presented in chapter 4, is the origin of the damping enhancement of the ferromagnetic layer, when it's thickness decreases, in magnetic heterostructures

without spin sink.

In chapter 5, we have used spin pumping as a method of pure spin current generation and then injected it into several ferromagnetic, antiferromagnetic, and paramagnetic spin sink layers. The algebraic functional form of this type of decay was verified in all these cases. The spin dephasing length found for three structurally distinct ferromagnets ($NiFe$, $CoFeB$, Co) is $\lambda_C = 1.2 \pm 0.1\, nm$. The same length for the antiferromagnet $IrMn$ is found to be slightly higher $\lambda_C \sim 1.7\, nm$, interpreted based on weakened exchange coupling. The similarity of spin current absorption characteristics in FM and AFM, reveals a very similar dephasing mechanisms is present in antiferromagnet. This is a direct evidence of a possible STT effect in antiferromagnets.

The absorption of spin current in paramagnetic Pt, Pd, Ru layers are found to follow an exponential characteristic length dependance, when they are separated by a spacer. The obtained length scales for absorption in these paramagnetic Pt, Pd, Ru was found to be much shorter than their respective spin diffusion lengths. Intuitively, we have argued that the absorption lengths for pure spin current and charge current might be different. These studies brings an open question on the difference of pure spin current transport and charge current transport.

In chapter 6, XMCD measurements on FM/NM multilayers, were performed to partly support our studies in chapters 4 and 5 were discussed. These measurements show that when the paramagnetic Pt, Pd are in direct contact with the FM layer $NiFe$, magnetic moments are induced via direct exchange coupling. For Pd evidence of indirect exchange coupling via $3nm$ of Cu was found.

For direct contact samples, this linear depth dependence of damping, has been identified as a hallmark of spin-splitting in the spin sink layer near the interface in these paramagnets. The character of spin current absorption in the ultrathin paramagnets Pd and Pt is modified by direct exchange with ferromagnetic $Ni_{81}Fe_{19}$. The range of linear increase is observed to be inversely proportional to the exchange energy, inferred through induced Pd and Pt moments measured by XMCD.

APPENDIX I

Complex Susceptibility is given as $\chi = \chi^{'} + i\chi^{''}$. Let us assume that there is a phase mixing between these two parts. Therefore we have to introduce a phase factor $e^{i\delta}$. Where δ denotes the mixing angle between dispersive and absorptive components. So, new susceptibility will be $\chi e^{i\delta} = \left(\chi^{'} + i\chi^{''}\right)(\cos\delta + i\sin\delta) = (\chi^{'}\cos\delta - \chi^{''}\sin\delta) + i(\chi^{'}\sin\delta +$

$\chi^{''}\cos\delta$).

As discussed in chapter 3; The FMR spectrum that we observe is the imaginary part ($\chi^{'}\sin\delta+\chi^{''}Cos\delta$) which is responsible for absorbing the electromagnetic radiation (power) applied to it. Therefore we have

$$\chi^{'}\sin\delta\sim\frac{(H-H_{FMR})\sin\delta}{(H-H_{FMR})^2+(\triangle H)^2}$$

and

$$\chi^{''}\cos\delta\sim\frac{\triangle H\cos\delta}{(H-H_{FMR})^2+(\triangle H)^2}$$

So, the absorption spectra after taking the the phase mixing into account reads:

$$f\left(H\right)\sim\left(\frac{(H-H_{FMR})\sin\delta}{(H-H_{FMR})^2+(\triangle H)^2}+\frac{\triangle H\cos\delta}{(H-H_{FMR})^2+(\triangle H)^2}\right)$$

The function that we fit is the derivative of $f\left(H\right)$ with respect to H. And the linewidth that we measure is $\triangle H_{pp}$, which is the peak to peak linewidth and related to $\triangle H$ as: $\triangle H=\frac{\sqrt{3}\triangle H_{pp}}{2}$. Therefore the derivative spectra, that we observe, reads as:

$$\frac{df\left(H\right)}{dH}\sim\left[\frac{-\sqrt{3}\triangle H_{pp}\left(H-H_{FMR}\right)\cos\delta+\left\{\left(\frac{\sqrt{3}\triangle H_{pp}}{2}\right)^2-\left(H-H_{FMR}\right)^2\right\}\sin\delta}{\left[\left(H-H_{FMR}\right)^2+\left(\frac{\sqrt{3}\triangle H_{pp}}{2}\right)^2\right]^2}\right]$$

Bibliography

[1] S. Chikazumi and C. Graham, *Physics of Ferromagnetism*. Clarendon press, Oxford, 1997.

[2] W. Brown, *Micromagnetics*. Interscience Publishers, John Wiley and Sons, Inc., New York, 1963.

[3] L. Landau and L. E.M., "On the theory of the dispersion of magnetic permeability in ferromagnetic bodies," *Phys. Z. Sowjetunion*, vol. 8, p. 153, 1935.

[4] T. Gilbert, "A lagrangian formulation of the gyromagnetic equation of the magnetic field," *Physical Review*, vol. 100, p. 1243, 1955.

[5] N. Bloembergen and S. Wang, "Relaxation effects in para and ferromagnetic resonance," *Phys. Rev.*, vol. 93, pp. 72–83, Jan 1954.

[6] D. Polder, "On the quantum theory of ferromagnetic resonance," *Phys. Rev.*, vol. 73, pp. 1116–1116, May 1948.

[7] F. Schreiber, J. Pflaum, Z. Frait, T. Muhge, and J. Pelzl, "Gilbert damping and g-factor in Fe_xCo_{1-x} alloy films," *Solid State Communications*, vol. 93, no. 12, pp. 965 – 968, 1995.

[8] V. Kambersky, "On the landau-lifshitz relaxation in ferromagnetic metals," *Canadian Journal of Physics*, vol. 48, no. 24, pp. 2906–2911, 1970.

[9] R. J. Elliott, "Theory of the effect of spin-orbit coupling on magnetic resonance in some semiconductors," *Phys. Rev.*, vol. 96, pp. 266–279, Oct 1954.

[10] J. Kuneš and V. Kamberský, "First-principles investigation of the damping of fast magnetization precession in ferromagnetic $3d$ metals," *Phys. Rev. B*, vol. 65, p. 212411, Jun 2002.

[11] V. Korenman and R. E. Prange, "Anomalous damping of spin waves in magnetic metals," *Phys. Rev. B*, vol. 6, pp. 2769–2777, Oct 1972.

[12] S. M. Bhagat and P. Lubitz, "Temperature variation of ferromagnetic relaxation in the 3*d* transition metals," *Phys. Rev. B*, vol. 10, pp. 179–185, Jul 1974.

[13] B. Bland, J.A.C.and Heinrich, *Ultrathin Magnetic Structures III*. Springer, 2005.

[14] L. Berger, "Emission of spin waves by a magnetic multilayer traversed by a current," *Phys. Rev. B*, vol. 54, pp. 9353–9358, Oct 1996.

[15] B. Heinrich and J. Cochran, "Ultrathin metallic magnetic films: magnetic anisotropies and exchange interactions," *Advances in Physics*, vol. 42, no. 5, pp. 523–639, 1993.

[16] B. Heinrich, J. F. Cochran, T. Monchesky, and R. Urban, "Exchange coupling through spin density wave cr(001) using fe whisker substrates," *Journal of Applied Physics*, vol. 87, no. 9, pp. 5449–5451, 2000.

[17] T. Silva and W. Rippard, "Developments in nano-oscillators based upon spin-transfer point-contact devices," *Journal of Magnetism and Magnetic Materials*, vol. 320, no. 7, pp. 1260 – 1271, 2008.

[18] J. C. Slonczewski, "Current-driven excitation of magnetic multilayers," *Journal of Magnetism and Magnetic Materials*, vol. 159, no. 1-2, pp. L1 – L7, 1996.

[19] M. Tsoi, A. G. M. Jansen, J. Bass, W.-C. Chiang, M. Seck, V. Tsoi, and P. Wyder, "Excitation of a magnetic multilayer by an electric current," *Phys. Rev. Lett.*, vol. 80, pp. 4281–4284, May 1998.

[20] E. B. Myers, D. C. Ralph, J. A. Katine, R. N. Louie, and R. A. Buhrman, "Current-induced switching of domains in magnetic multilayer devices," *Science*, vol. 285, no. 5429, pp. 867–870, 1999.

[21] Y. Tserkovnyak, A. Brataas, and G. E. W. Bauer, "Enhanced Gilbert damping in thin ferromagnetic films," *Phys. Rev. Lett.*, vol. 88, no. 11, p. 117601, 2002.

[22] Y. Tserkovnyak, A. Brataas, G. E. W. Bauer, and B. I. Halperin, "Nonlocal magnetization dynamics in ferromagnetic heterostructures," *Rev. Mod. Phys.*, vol. 77, pp. 1375–1421, Dec 2005.

[23] H. Nakayama, K. Ando, K. Harii, T. Yoshino, R. Takahashi, Y. Kajiwara, K. Uchida, Y. Fujikawa, and E. Saitoh, "Geometry dependence on inverse spin hall effect induced by spin pumping in $ni_{81}fe_{19}$/pt films," *Phys. Rev. B*, vol. 85, p. 144408, Apr 2012.

[24] A. Brataas, G. E. Bauer, and P. J. Kelly, "Non-collinear magnetoelectronics," *Physics Reports*, vol. 427, no. 4, pp. 157 – 255, 2006.

[25] A. Brataas, Y. Tserkovnyak, G. E. W. Bauer, and P. J. Kelly, "Spin pumping and spin transfer," 2011.

[26] A. Brataas, Y. Nazarov, and G. Bauer, "Spin-transport in multi-terminal normal metal-ferromagnet systems with non-collinear magnetizations," *The European Physical Journal B - Condensed Matter and Complex Systems*, vol. 22, pp. 99–110, 2001. 10.1007/PL00011139.

[27] A. Brataas, Y. V. Nazarov, and G. E. W. Bauer, "Finite-element theory of transport in ferromagnet˘normal metal systems," *Phys. Rev. Lett.*, vol. 84, pp. 2481–2484, Mar 2000.

[28] S. I. Kiselev, J. C. Sankey, I. N. Krivorotov, N. C. Emley, R. J. Schoelkopf, R. A. Buhrman, and D. C. Ralph, "Microwave oscillations of a nanomagnet driven by a spin-polarized current," *Nature*, vol. 425, pp. 380–383, Sep 2003.

[29] J. C. Slonczewski, "Excitation of spin waves by an electric current," *Journal of Magnetism and Magnetic Materials*, vol. 195, no. 2, pp. 261 – 268, 1999.

[30] Y. Tserkovnyak, A. Brataas, and G. E. W. Bauer, "Spin pumping and magnetization dynamics in metallic multilayers," *Phys. Rev. B*, vol. 66, p. 224403, Dec 2002.

[31] M. Zwierzycki, Y. Tserkovnyak, P. J. Kelly, A. Brataas, and G. E. W. Bauer, "First-principles study of magnetization relaxation enhancement and spin transfer in thin magnetic films," *Phys. Rev. B*, vol. 71, p. 064420, Feb 2005.

[32] M. D. Stiles and A. Zangwill, "Anatomy of spin-transfer torque," *Phys. Rev. B*, vol. 66, p. 014407, Jun 2002.

[33] A. Ghosh, S. Auffret, U. Ebels, and W. Bailey, "Penetration depth of transverse spin current in ultrathin ferromagnets," *Phys. Rev. Lett.*, vol. 109, p. 032000, Aug 2012.

[34] T. Taniguchi, S. Yakata, H. Imamura, and Y. Ando, "Determination of penetration depth of transverse spin current in ferromagnetic metals by spin pumping," *Applied Physics Express*, vol. 1, no. 3, p. 031302, 2008.

[35] A. Janossy and P. Monod, "Spin waves for single electrons in paramagnetic metals," *Phys. Rev. Lett.*, vol. 37, pp. 612–615, Sep 1976.

[36] R. H. Silsbee, A. Janossy, and P. Monod, "Coupling between ferromagnetic and conduction-spin-resonance modes at a ferromagnetic¯normal-metal interface," *Phys. Rev. B*, vol. 19, pp. 4382–4399, May 1979.

[37] S. Mizukami, Y. Ando, and T. Miyazaki, "Magnetic relaxation of normal-metal nm/80nife/nm films," *Journal of Magnetism and Magnetic Materials*, vol. 239, pp. 42 – 44, 2002. International Symposium on Physics of Magnetic Materials/Internat ional Symposium on Advanced Magnetic Technologies.

[38] S. Mizukami, Y. Ando, and T. Miyazaki, "Effect of spin diffusion on gilbert damping for a very thin permalloy layer in cu/permalloy/cu/pt films," *Phys. Rev. B*, vol. 66, p. 104413, Sep 2002.

[39] B. Heinrich, Y. Tserkovnyak, G. Woltersdorf, A. Brataas, R. Urban, and G. E. W. Bauer, "Dynamic exchange coupling in magnetic bilayers," *Phys. Rev. Lett.*, vol. 90, p. 187601, May 2003.

[40] M. Bü ttiker, H. Thomas, and A. PrÃªtre, "Current partition in multiprobe conductors in the presence of slowly oscillating external potentials," *Zeitschrift fÃŒr Physik B Condensed Matter*, vol. 94, pp. 133–137, 1994. 10.1007/BF01307664.

[41] A. Brataas, Y. Tserkovnyak, P. G. Bauer, and P. P. Kelly, "Spin pumping and spin transfer," in *Spin Current* (S. Maekawa, S. Valenzuela, E. Saitoh, and T. Kimura, eds.), pp. 87–135, Oxford: Oxford University Press, 2012.

[42] J. Bass and W. P. Jr., "Spin-diffusion lengths in metals and alloys, and spin-flipping at metal/metal interfaces: an experimentalist's critical review," *J. Phys.: Condens. Matter*, vol. 19, no. 18, 2007.

[43] R. Urban, G. Woltersdorf, and B. Heinrich, "Gilbert damping in single and multilayer ultrathin films: Role of interfaces in nonlocal spin dynamics," *Phys. Rev. Lett.*, vol. 87, p. 217204, Nov 2001.

[44] P. W. Brouwer, "Scattering approach to parametric pumping," *Phys. Rev. B*, vol. 58, pp. R10135–R10138, Oct 1998.

[45] E. Šimánek and B. Heinrich, "Gilbert damping in magnetic multilayers," *Phys. Rev. B*, vol. 67, p. 144418, Apr 2003.

[46] S. Mizukami, Y. Ando, and T. Miyazaki, "The study on ferromagnetic resonance linewidth for nm/nife/nm(nm=cu, ta, pd and pt)films," *Japanese Journal of Applied Physics*, vol. 40, no. Part 1, No. 2A, pp. 580–585, 2001.

[47] S. Ingvarsson, L. Ritchie, X. Y. Liu, G. Xiao, J. C. Slonczewski, P. L. Trouilloud, and R. H. Koch, "Role of electron scattering in the magnetization relaxation of thin $ni_{81}fe_{19}$ films," *Phys. Rev. B*, vol. 66, p. 214416, Dec 2002.

[48] T. Gerrits, M. L. Schneider, and T. J. Silva, "Enhanced ferromagnetic damping in permalloy/cu bilayers," *Journal of Applied Physics*, vol. 99, no. 2, p. 023901, 2006.

[49] R. D. McMichael and M. D. Stiles, "Magnetic normal modes of nanoelements," *Journal of Applied Physics*, vol. 97, no. 10, p. 10J901, 2005.

[50] W. Chen, M. J. Rooks, N. Ruiz, J. Z. Sun, and A. D. Kent, "Spin transfer in bilayer magnetic nanopillars at high fields as a function of free-layer thickness," *Phys. Rev. B*, vol. 74, p. 144408, Oct 2006.

[51] K. C. Gupta, R. Gerg, I. Bahl, and P. Bhartia, "Microstrip lines and slotlines," vol. 2nd Edition, 1996.

[52] J. Stohr and S. H.C., *Magnetism From Fundamentals to Nanoscale Dynamics*. Springer-Verlag Berlin Heidelberg, 2006.

[53] B. T. Thole, P. Carra, F. Sette, and G. van der Laan, "X-ray circular dichroism as a probe of orbital magnetization," *Phys. Rev. Lett.*, vol. 68, pp. 1943–1946, Mar 1992.

[54] A. J. P. Meyer and G. Asch, "Experimental g[prime] and g values of fe, co, ni, and their alloys," *Journal of Applied Physics*, vol. 32, no. 3, pp. S330–S333, 1961.

[55] Y. S. Chen, C.-W. Cheng, G. Chern, W. F. Wu, and J. G. Lin, "Ferromagnetic resonance probed annealing effects on magnetic anisotropy of perpendicular cofeb/mgo bilayer," *Journal of Applied Physics*, vol. 111, no. 7, p. 07C101, 2012.

[56] J. O. Rantschler, P. J. Chen, A. S. Arrott, R. D. McMichael, J. W. F. Egelhoff, and B. B. Maranville, "Surface anisotropy of permalloy in nm/nife/nm multilayers," *Journal of Applied Physics*, vol. 97, no. 10, p. 10J113, 2005.

[57] C. R. Tellier and A. J. Tosser, "Size effects in thin films,"

[58] A. Ghosh, J. F. Sierra, S. Auffret, U. Ebels, and W. E. Bailey, "Dependence of nonlocal gilbert damping on the ferromagnetic layer type in ferromagnet/Cu/Pt heterostructures," *Applied Physics Letters*, vol. 98, no. 5, p. 052508, 2011.

[59] B. Dieny, J. P. Nozieres, V. S. Speriosu, B. A. Gurney, and D. R. Wilhoit, "Change in conductance is the fundamental measure of spin-valve magnetoresistance," *Applied Physics Letters*, vol. 61, no. 17, pp. 2111–2113, 1992.

[60] W. E. Bailey, S. X. Wang, and E. Y. Tsymbal, "Electronic scattering from co/cu interfaces: *In situ* measurement and comparison with theory," *Phys. Rev. B*, vol. 61, pp. 1330–1335, Jan 2000.

[61] A. Fert and L. Piraux, "Magnetic nanowires," *Journal of Magnetism and Magnetic Materials*, vol. 200, pp. 338 – 358, 1999.

[62] A. Reilly, W. Park, R. Slater, B. Ouaglal, R. Loloee, W. P. Jr., and J. Bass, "Perpendicular giant magnetoresistance of co91fe9/cu exchange-biased spin-valves: further evidence for a unified picture," *Journal of Magnetism and Magnetic Materials*, vol. 195, no. 2, pp. L269 – L274, 1999.

[63] C. Ahn, K.-H. Shin, and J. William P. Pratt, "Magnetotransport properties of cofeb and co/ru interfaces in the current-perpendicular-to-plane geometry," *Applied Physics Letters*, vol. 92, no. 10, p. 102509, 2008.

[64] S. Mizukami, Y. Ando, and T. Miyazaki, "Ferromagnetic resonance linewidth for nm/80nife/nm films (nm=cu, ta, pd and pt)," *Journal of Magnetism and Magnetic Materials*, vol. 226, no. 0, pp. 1640 – 1642, 2001. ¡ce:title¿Proceedings of the International Conference on Magnetism (ICM 2000)¡/ce:title¿.

[65] H. Lee, L. Wen, M. Pathak, P. Janssen, P. LeClair, C. Alexander, C. Mewes, and T. Mewes, "Spin pumping in $Co_{56}Fe_{24}B_{20}$ multilayer systems," *Journal of Physics D: Applied Physics*, vol. 41, no. 21, pp. 215001 (5 pp.) –, 2008.

[66] J.-M. Beaujour, J. Lee, A. Kent, K. Krycka, and C.-C. Kao, "Magnetization damping in ultrathin polycrystalline co films: evidence for nonlocal effects," *Physical Review B (Condensed Matter and Materials Physics)*, vol. 74, no. 21, pp. 214405 – 1, 2006.

[67] J.-M. L. Beaujour, W. Chen, A. D. Kent, and J. Z. Sun, "Ferromagnetic resonance study of polycrystalline cobalt ultrathin films," *Journal of Applied Physics*, vol. 99, no. 8, p. 08N503, 2006.

[68] J. Foros, G. Woltersdorf, B. Heinrich, and A. Brataas, "Scattering of spin current injected in pd(001)," *Journal of Applied Physics*, vol. 97, no. 10, p. 10A714, 2005.

[69] W. Weber, S. Riesen, and H. C. Siegmann, "Magnetization precession by hot spin injection," *Science*, vol. 291, no. 5506, pp. 1015–1018, 2001.

[70] J. Zhang, P. M. Levy, S. Zhang, and V. Antropov, "Identification of transverse spin currents in noncollinear magnetic structures," *Phys. Rev. Lett.*, vol. 93, p. 256602, Dec 2004.

[71] D. Ralph and M. Stiles, "Spin transfer torques," *Journal of Magnetism and Magnetic Materials*, vol. 320, no. 7, pp. 1190 – 1216, 2008.

[72] S. Wang, Y. Xu, and K. Xia, "First-principles study of spin-transfer torques in layered systems with noncollinear magnetization," *Phys. Rev. B*, vol. 77, p. 184430, May 2008.

[73] W. Weber, S. Riesen, C. H. Back, A. Shorikov, V. Anisimov, and H. C. Siegmann, "Spin motion of electrons during reflection from a ferromagnetic surface," *Phys. Rev. B*, vol. 66, p. 100405, Sep 2002.

[74] Q. Yang, P. Holody, S.-F. Lee, L. L. Henry, R. Loloee, P. A. Schroeder, W. P. Pratt, and J. Bass, "Spin flip diffusion length and giant magnetoresistance at low temperatures," *Phys. Rev. Lett.*, vol. 72, pp. 3274–3277, May 1994.

[75] L. Piraux, S. Dubois, A. Fert, and L. Belliard, "The temperature dependence of the perpendicular giant magnetoresistance in co/cu multilayered nanowires," *The European Physical Journal B - Condensed Matter and Complex Systems*, vol. 4, pp. 413–420, 1998.

[76] K. Carva and I. Turek, "Spin-mixing conductances of thin magnetic films from first principles," *Phys. Rev. B*, vol. 76, p. 104409, Sep 2007.

[77] R. Meservey and P. M. Tedrow, "Surface relaxation times of conduction-electron spins in superconductors and normal metals," *Phys. Rev. Lett.*, vol. 41, pp. 805–808, Sep 1978.

[78] J. Vogel, A. Fontaine, V. Cros, F. Petroff, J.-P. Kappler, G. Krill, A. Rogalev, and J. Goulon, "Structure and magnetism of pd in pd/fe multilayers studied by x-ray magnetic circular dichroism at the pd $l_{2,3}$sedges," *Phys. Rev. B*, vol. 55, pp. 3663–3669, Feb 1997.

[79] S. Yakata, Y. Ando, T. Miyazaki, and S. Mizukami, "Temperature dependences of spin-diffusion lengths of cu and ru layers," *Japanese Journal of Applied Physics*, vol. 45, no. 5A, pp. 3892–3895, 2006.

[80] J. W. Cable, E. O. Wollan, W. C. Koehler, and M. K. Wilkinson, "Neutron diffraction investigations of ferromagnetic palladium and iron group alloys," *Journal of Applied Physics*, vol. 33, no. 3, pp. 1340–1340, 1962.

[81] M. A. Ruderman and C. Kittel, "Indirect exchange coupling of nuclear magnetic moments by conduction electrons," *Phys. Rev.*, vol. 96, pp. 99–102, Oct 1954.

[82] S. S. P. Parkin, "Systematic variation of the strength and oscillation period of indirect magnetic exchange coupling through the 3 *d* , 4 *d* , and 5 *d* transition metals," *Phys. Rev. Lett.*, vol. 67, pp. 3598–3601, Dec 1991.

[83] M. Li, X. D. Ma, C. B. Peng, J. G. Zhao, L. M. Mei, Y. S. Gu, W. P. Chai, Z. H. Mai, B. G. Shen, Y. H. Liu, and D. S. Dai, "Magnetic-polarization effect of pd layers in fe/pd multilayers," *Phys. Rev. B*, vol. 50, pp. 10323–10326, Oct 1994.

[84] R. Nakatani, K. Hoshino, S. Noguchi, and Y. Sugita, "Magnetoresistance and preferred orientation in fe–mn/ni–fe/cu/ni–fe sandwiches with various buffer layer materials," *Japanese Journal of Applied Physics*, vol. 33, no. Part 1, No.1A, pp. 133–137, 1994.

[85] A. Rogalev, F. Wilhelm, N. Jaouen, J. Goulon, and J.-P. Kappler, *X-ray magnetic circular dichroism: historical perspective and recent highlights*, pp. 71 – 93. 2006.

[86] P. Carra, B. T. Thole, M. Altarelli, and X. Wang, "X-ray circular dichroism and local magnetic fields," *Phys. Rev. Lett.*, vol. 70, pp. 694–697, Feb 1993.

[87] M. G. Samant, J. Stöhr, S. S. P. Parkin, G. A. Held, B. D. Hermsmeier, F. Herman, M. Van Schilfgaarde, L.-C. Duda, D. C. Mancini, N. Wassdahl, and R. Nakajima, "Induced spin polarization in cu spacer layers in co/cu multilayers," *Phys. Rev. Lett.*, vol. 72, pp. 1112–1115, Feb 1994.

[88] *Landolt-Bornstein Tables*, ch. 1.3: 4d and 5d elements, alloys and compounds, p. 492. 1990.